



TECHNISCHE UNIVERSITÄT MÜNCHEN

Fakultät für Chemie

**Nonlinear Time-Resolved Spectroscopy of
Molecular Ensembles and Single Molecules:
Theory and Simulations**

DISSERTATION

Zur Erlangung des akademischen Grades
Doktor der Naturwissenschaften

vorgelegt von

Elisa Palacino González

Garching bei München, 2018



TECHNISCHE UNIVERSITÄT MÜNCHEN

Lehrstuhl für Theoretische Chemie

Nonlinear Time-Resolved Spectroscopy of Molecular Ensembles and Single Molecules: Theory and Simulations

Elisa Palacino González

Vollständiger Abdruck der von der Fakultät für Chemie der Technischen Universität
München zur Erlangung des akademischen Grades eines

Doktors der Naturwissenschaften

genehmigten Dissertation.

Vorsitzende: Prof. Dr. Tanja Gulder

Prüfer der Dissertation:

1. Prof. Dr. Wolfgang Domcke

2. Prof. Dr. Jürgen Hauer

Die Dissertation wurde am 21.11.2018 bei der Technische Universität München eingereicht
und durch die Fakultät für Chemie am 14.01.2019 angenommen.

This doctoral thesis is based on contributions to international peer-reviewed scientific journals. The work presented in this thesis has been published, has been submitted for publication, or is in a preprint form for forthcoming submission to an international scientific journal, by the time of submission of this thesis.

This work describes the development of novel theoretical methods for the calculation of nonlinear optical spectra, as well as the application of these methods for the analysis and interpretation of spectroscopic signals. The applications cover the spectroscopy of molecular ensembles as well as the spectroscopy of single molecules in the femtosecond time domain. The analysis is based on a non-perturbative formalism for the treatment of molecules with the external fields. Both the weak-field regime and the strong-field regime have been considered. A conspectus of two published papers and a manuscript in preparation is given. These three contributions are included in the Appendix.

E.P.G., Garching bei München, November 2018

Abstract

Modern techniques of nonlinear femtosecond spectroscopy are capable of unraveling the photoinduced dynamics in polyatomic chromophores in great detail. However, the information of interest is encoded in time- and frequency-resolved signal, the interpretation of which requires theoretical analysis and numerical simulations. In the present work, nonperturbative methods have been applied for the simulation of ensemble spectra and single-molecule signals. These simulations emulate the actual experiments: the response of the chromophore to the external fields of the laser pulses is numerically evaluated. Pulse-overlap effects and strong-field effects are automatically accounted for.

In the first part of this thesis, the concept of “ideal” and “real” transient-absorption pump-probe signals is introduced. The ideal signal provides insight into the mechanisms of detection of time- and frequency-resolved signals. It is demonstrated that the ideal signal is a two-faceted object, which exhibits the features of moving wave packets and stationary spectra. Its projection on short (good temporal resolution) or long (good frequency resolution) probe pulse gives the measurable spectra. For this analysis, I extended the method for the simulation of transient absorption signals [*Chem. Phys.* **312**, 135 (2005)] to account for excited-state absorption. The pump pulse can be of arbitrary strength, while the probe pulse is assumed to be weak. These results are illustrated for a model system which exhibits nonadiabatic dissipative dynamics.

In the second part of this thesis, the theoretical foundations of femtosecond double-pump single-molecule spectroscopy are developed. This novel spectroscopic technique is based on the detection of the fluorescence of individual chromophores which are excited by a pair of phase-locked pulses. I developed a general method for the simulation

of these signals which is based on the numerical solution of driven master equations. Fluctuations of the chromophore parameters induced by the environment are taken into account by a stochastic model. I performed a series of simulations, both in the regime of weak system-field coupling (when the signal scales linearly with the intensity of the pulses) as well as in the regime of strong system-field coupling (when the signal exhibits nonlinear scaling with the pulse intensity). In the weak-field regime, the signals are dominated by the coherence of the electronic density matrix of the chromophore, which is rapidly quenched by electronic dephasing. This restricts the information content of weak-field signals. In the strong-field regime, on the other hand, electronic populations contribute to the signals. The populations are not affected by electronic dephasing, which renders strong-field signals more robust with respect to environmental fluctuations.

Zusammenfassung

Mit den modernen Techniken der nichtlinearen Femtosekunden-Spektroskopie kann die photoinduzierte Dynamik von vielatomigen Molekülen im Detail untersucht werden. Die interessante Information ist jedoch in Zeit- und Frequenz-aufgelösten Signalen enthalten, deren Interpretation theoretische Analyse und numerische Simulationen erfordert. In der vorliegenden Arbeit wurden nichtstörungstheoretische Methoden benutzt, um sowohl Ensemble-Spektren als auch Einzelmolekül-Spektren zu simulieren. Die Simulationen imitieren dabei das Experiment: die Reaktion des Chromophors auf die externen Felder der Laser-Pulse wird numerisch berechnet. Die Effekte überlappender Pulse und starker Felder werden damit automatisch berücksichtigt. Im ersten Teil der Arbeit wird das Konzept „idealer“ und „realer“ Pump-Probe-Signale am Beispiel der transienten Absorption eingeführt. Das ideale Signal liefert Einsicht in die Mechanismen der Detektion von Zeit- und Frequenz-aufgelösten Spektren. Es wird gezeigt, dass das ideale Signal ein zwei-gesichtiges Objekt ist, welches Eigenschaften bewegter Wellenpakete und stationärer Spektren aufweist. Seine Projektion auf kurze (gute Zeitauflösung) oder lange (gute Frequenzauflösung) Probe-Pulse liefert die messbaren Spektren. Für diese Analyse erweiterte ich die Methode für die Simulation von transienten Absorptionssignalen [Chem Phys. 312, 135 (2005)] durch die Berücksichtigung der Absorption aus dem angeregten Zustand. Der Pump-Puls kann von beliebiger Stärke sein, während der Probe-Puls als schwach angenommen wird. Diese Resultate werden für ein Modellsystem, welches nichtadiabatische und dissipative Dynamik aufweist, illustriert. Im zweiten Teil der Arbeit werden die theoretischen Grundlagen der Femtosekunden-Doppel-Pump-Einzelmolekülspektroskopie entwickelt. Diese neuartige spektroskopische Methode basiert auf der Detektion der Fluoreszenz einzelner Moleküle nach Anregung durch ein phasenstabilisiertes Paar von Laserpulsen. Ich entwickelte eine allgemeine Methode für die Simulation dieser Signale, die auf der

numerischen Lösung getriebener Mastergleichungen beruht. Fluktuationen der Parameter der Chromophore, welche durch die Umgebung induziert werden, werden durch ein stochastisches Modell berücksichtigt. Ich führte eine Reihe von Simulationen durch, sowohl im Regime schwacher Kopplung von Chromophor und Feld (wenn das Signal linear mit der Intensität der Pulse skaliert) als auch im Regime starker Kopplung (wenn das Signal nichtlinear mit der Intensität der Pulse skaliert). Im Fall schwacher Felder werden die Signale durch die Kohärenz der elektronischen Dichtematrix dominiert, welche sehr schnell durch elektronische Dephasierung gelöscht wird. Dies schränkt den Informationsgehalt der Signale beträchtlich ein. Im Fall starker Felder tragen andererseits elektronische Populationen zu den Signalen bei, welche durch die elektronische Dephasierung nicht beeinflusst werden. Aus diesem Grund sind Signale, die durch starke Felder induziert werden, robuster gegenüber Fluktuationen der Umgebung.

PREFACE

This dissertation is submitted for the degree of Doctor of Philosophy at the Technical University of Munich.

As a former chemist by undergraduate background I could definitely be biased to introduce this thesis from a chemical perspective. However, the reality is that it truly rests in between chemistry, physics and computer science. Frankly, and being pragmatic, I should definitely say physics is the main area in which we could set it. However, after these years I understood that most of the chemistry of it resides behind the words of “Theoretische Chemie Lehrstuhl”. It can be difficult to imagine how a chemist would decide to pursue a doctorate in such a unfamiliar topic. Well, that is an interesting point, and in fact it is the reason why I decided to write about it in the first place.

After graduating in a five-year Diploma degree in Chemistry in Spain and decided to pursue a further career in science, I involved myself in a journey that would be the starting point of my scientific life. Later of contacting Prof. Domcke with my enthusiasm in doing a doctoral degree in his research group, he offered me different available PhD topics to choose from. They covered different approaches from pure applicational work in quantum chemistry to simulation of nonlinear optical spectra. At that point I should say the closest topic to my expertise definitely was the first one mentioned, however, my neuronal-based logics at that moment was highly influenced by the factor of curiosity (or maybe unsensibility) and exploring new things in a different area that the one I was used to. This made me choose at that time a PhD topic which could be untitled as: “theoretical developments in nonlinear optical spectroscopies”. This broad topic

has been my main activity since I joined the group and, after four years I find myself writing up this thesis. After these PhD years I have sharpened my knowledge in this field and developed myself in several scientific aspects. Moreover my stand up comedy skills have boosted since I started my PhD (which I think it is certainly not due to pure casualty).

I would like to thank my advisor through all these years, Professor Wolfgang Domcke, who gave me the opportunity to do my doctoral studies in his department. His experience and scientific knowledge were certainly a support for making this thesis possible. I would like as well to thank Dr. Maxim Gelin, my PhD supervisor, with whom I have had very fruitful scientific discussions and shared a lot of interesting ideas. Finally I am specially grateful for the support of my family, friends (including my dog) and David, who gave me strength specially in the most challenging times of these doctoral years and made me fully enjoy my stay in Munich.

To my parents

*"I love being a stand up comedian. It's probably the best job ever,
Uh... if I could have any job, I would be a cat.
But that's not something I'm supposed to talk about in public."
-Iliza Shlesinger- stand up comedian*

LIST OF ABBREVIATIONS

2PPE:	<i>Two-Pulse Photon-Echo</i>
4WM:	<i>Four-Wave Mixing</i>
CARS:	<i>Coherent Anti-Stokes Raman Scattering</i>
DDA:	<i>Diabatic Damping Approximation</i>
DW:	<i>Doorway-Window</i>
ET:	<i>Electron Transfer</i>
ESA:	<i>Excited-State Absorption</i>
EOM-PMA:	<i>Equation of Motion Phase-Matching Approach</i>
FSRS:	<i>Femtosecond Stimulated Raman Spectroscopy</i>
GR:	<i>Golden Rule</i>
GSB:	<i>Ground-State Bleach</i>
HEOM:	<i>Hierarchy Equation-of-Motion</i>
PP:	<i>Pump-Probe</i>
RDM:	<i>Reduced Density Matrix</i>
RWA:	<i>Rotating Wave Approximation</i>
SA:	<i>Secular Approximation</i>

SM: *Single-Molecule*

SE: *Stimulated emission*

TFG: *Time and Frequency Gate*

TA PP: *Transient-Absorption Pump-Probe*

CONTENTS

1	INTRODUCTION	1
2	BACKGROUND	9
2.1	The Density Operator	9
2.2	The Reduced Density Matrix	11
2.3	Time Evolution of the Density Operator	13
2.4	Time-Dependent Perturbation Theory. The Interaction Picture	15
2.5	Redfield Theory for Open Quantum Systems	17
3	THEORY OF NONLINEAR OPTICAL SPECTROSCOPY: RESPONSE FUNCTIONS	23
3.1	Basic Concepts in Time and Frequency Resolved Spectroscopy	23
3.2	The Perturbative Approach: Nonlinear Response Functions	25
3.3	Reduction of the Number of Coherent Pathways	26
3.3.1	The Rotating Wave Approximation	26
3.3.2	The Phase Matching Condition	30
3.4	Representative Non-Linear Optical Spectroscopies and the Corresponding Response Functions	32
3.4.1	Linear Absorption Spectroscopy	32
3.4.2	Pump-probe Spectroscopy	35
3.4.3	Two-Pulse Photon-Echo Spectroscopy	38
4	THE NON-PERTURBATIVE FORMALISM	41
4.1	The Equation of Motion Phase-Matching Approach for Three-Pulse Spectroscopy	42

4.2	Two-Pulse Based Methods: Ideal and Real Time- and Frequency-Resolved Spectra	44
4.3	The Doorway-Window Representation of Nonlinear Response Functions	46
5	DOUBLE-PUMP FEMTOSECOND FLUORESCENCE SPECTROSCOPY OF SINGLE MOLECULES	49
6	PUBLICATIONS AND MANUSCRIPTS	55
6.1	Analysis of transient-absorption pump-probe signals of nonadiabatic dissipative systems	56
6.2	Theoretical aspects of femtosecond double-pump single-molecule spectroscopy I. Weak-field regime	58
6.3	Theoretical aspects of femtosecond double-pump single-molecule spectroscopy II. Strong-field regime	60
7	CONCLUSIONS	63
8	APPENDIX	73

INTRODUCTION

Spectroscopy is based on the interaction of matter and electromagnetic fields. The main idea behind spectroscopy is to use the external perturbation by an electromagnetic field to probe the structure and dynamical processes of matter. There are many different radiative transitions that can occur. A classification of them can be based on different criteria, such as the order of the response of the system to the external fields, the type of resonances, the distinction between time- and frequency-domain techniques and the properties of the system under study, among others. The information content of various spectroscopic techniques is different and thus the choice of a technique depends on the kind of information one wants to extract. When an external electromagnetic field interacts with a molecular system, an induced polarization $P(t)$ is generated in the system as a consequence of response of the molecular ensemble to the external perturbation. This polarization, which represents the density of induced electric dipole moments per unit volume, constitutes the macroscopic observable of interest in most spectroscopic studies. Experimentally, the measured quantity is the electric field radiated by the induced polarization, which is expressed through the polarization as

$$E(t) \propto -iP(t). \quad (1.1)$$

Spectroscopic signals reveal how the induced polarization of a system varies with wavelength and time.

The most general classification of spectroscopic techniques can be based on the domain in which they are performed: frequency-resolved techniques or time-resolved techniques.¹ Historically, spectroscopy has been perceived as a frequency-resolved technique, involving external electromagnetic fields of long duration and narrow bandwidth interacting with the material system. In this context, UV/Visible, IR, Raman and X-ray spectroscopies have been extensively performed. The emergence of picosecond and femtosecond lasers has permitted the development of so-called ultrafast time-resolved spectroscopies,² in which short (and thus spectrally broad) pulses are employed to obtain information about the dynamics of physical, chemical or biological systems. The increasing shortening of the pulses down to the femtosecond (10^{-15} s) regime has permitted the monitoring of nuclear motion and elementary processes of chemical dynamics in real time.³ Ultrafast time-resolved spectroscopic techniques are widely employed nowadays for the probing of ultrafast electron and proton transfer reactions or solvation dynamics of diverse molecular systems.

Another classification of spectroscopic techniques can be based on the dependence of the induced polarization on the external electric field. The polarization can be expanded as

$$P = P^{(1)} + P^{(2)} + P^{(3)} + \dots \quad (1.2)$$

Here $P^{(1)}(t)$ is the linear polarization, which represents the linear optical response of the system. It describes absorption of weak fields. Beyond this weak-field limit, higher-order optical responses can be generated. The nonlinear polarization

$$P_{NL} = P^{(2)} + P^{(3)} + \dots \quad (1.3)$$

becomes relevant when the external electric field is intense or when several light-matter interactions occur with weak laser pulses.

The most commonly employed nonlinear techniques are referred to as “multi-wave mixing” spectroscopies. An n -wave mixing process involves the interaction of the system with n laser fields with wave vectors k_1, k_2, \dots, k_n and frequencies $\omega_1, \omega_2, \dots, \omega_n$. By this interaction, a coherent signal is generated and detected in the direction given by the wave-vector k_s and with frequency ω_s . k_s and ω_s are given by linear combinations of the applied wave vectors and frequencies. The different combinations that arise from the particular choice of signs defining k_s and ω_s define the possible processes that can be detected. Three-wave mixing processes ($n = 2$) are described by second-order polarizations $P^{(2)}(t)$ (for example, second harmonic generation, sum frequency generation or difference frequency generation). These processes vanish in random isotropic media with inversion symmetry. Therefore, the lowest-order optical nonlinearity is usually related to the third-order polarization $P^{(3)}(t)$. The spectroscopies related to $P^{(3)}(t)$ are called *four-wave mixing (4WM)* processes. They are the most widely used techniques in modern ultrafast spectroscopy. Examples are third harmonic generation, photon echo, transient grating, coherent anti-Stokes Raman scattering (CARS), among others. In these techniques, the signal is measured in a direction which differs from the incoming waves, in contrast to other 4WM techniques like pump-probe or hole-burning spectroscopy, in which the signal is generated in the direction of one of the incoming beams and the effect on this beam is measured (self action).

While linear spectroscopic techniques cannot resolve couplings or spectral correlations directly, nonlinear techniques can provide information on these properties.⁴ For example, effects such as homogeneous or inhomogeneous broadening cannot be uniquely deduced from linear spectra. The interpretation of certain dynamics and relaxation processes is out of reach for linear techniques. These processes are of particular relevance in condensed-phase spectroscopy, where lineshapes are broad and spectra are congested.

Nonlinear spectroscopies, on the other hand, provide a powerful tool for resolving these phenomena due to the simultaneous and independent control over the different frequencies involved or the time-ordering of the incoming fields, which allows the probing of correlations between different spectral features.

Table 1.1 summarizes some of the linear and nonlinear techniques, classified as coherent and spontaneous processes.


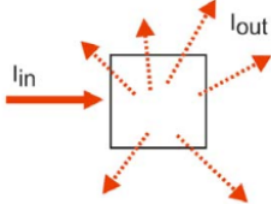
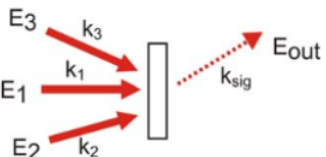
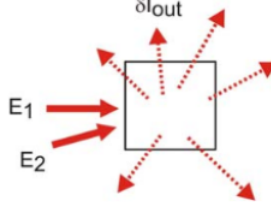
Detection:	<u>Coherent</u>	<u>Spontaneous</u>
	$I_{coherent} \propto \left \sum_i \mu_i \right ^2$ <p>Dipoles are driven coherently, and radiate with constructive interference in direction \bar{k}_{sig}</p>	$I_{spont.} \propto \sum_i \mu_i ^2$ <p>Dipoles radiate independently</p> $\bar{E}_{sig} \propto \sin \theta$
<u>Linear:</u>	<p>Absorption</p> 	<p>Fluorescence, phosphorescence, Raman, and light scattering</p> 
<u>Nonlinear:</u>	 <p>Pump-probe transient absorption, photon echoes, transient gratings, CARS, impulsive Raman scattering</p>	 <p>Fluorescence-detected nonlinear spectroscopy, i.e. stimulated emission pumping, time-dependent Stokes shift</p>

Table 1: Classification of some linear and nonlinear techniques according to their coherent or spontaneous nature. (Source: *Time-dependent Quantum Mechanics and Spectroscopy Lectures*, Andrei Tokmakoff, University of Chicago, 2014).

The traditional theoretical description of ultrafast nonlinear spectroscopy is based on the concept of *nonlinear optical response functions*.^{1,5} The response functions are defined within the perturbative formalism in which the interaction of material systems with

external fields is treated in perturbation theory. Within this formalism, an intuitive understanding of the dynamics of a molecular system undergoing excitation by external pulses can be developed. The perturbative formalism is considered in some detail in section 3.2.

This traditional way of studying light-matter interaction is restricted with respect to the size of the system under consideration. When the complexity of the molecular system increases, for example when nonadiabatic couplings or relaxation phenomena take place in a polyatomic molecule, the perturbative method becomes computationally expensive. To tackle such problems, nonperturbative descriptions based on the numerically exact solution of the equation of motion have been developed in recent years.^{6–10} These methods include the so-called equation-of-motion phase-matching approach (EOM-PMA)⁷ for the calculation the third-order polarization, the two-pulse EOM-PMA⁶ and the Doorway-Window (DW) concept,^{8–12} among others. The main difference between the perturbative and the nonperturbative formalisms consists in the way the electric polarization $P(t)$ is evaluated, perturbatively or nonperturbatively. One of the advantages of the non-perturbative formalism is that it can readily be combined with any numerical method describing the dynamics of the system. Nonperturbative methods also allow us to deal with strong system-field couplings.

Usually ultrafast spectroscopic experiments are performed in the regime of weak field-matter interaction, where the order of the induced polarization providing the signal is determined by the number of fields used. However, a growing number of ultrafast 4WM techniques have revealed much richer information on the photodynamics of different molecular systems by the use of more intense pulses.^{1,13–24,41} In this strong-field regime, simulations based on a perturbative treatment of the polarization are clearly inadequate (the perturbation series may even not converge). Instead, one has to use a nonperturbative formalism, in which all relevant laser fields are incorporated

into the Hamiltonian and the light-driven system dynamics is evaluated numerically exactly.^{37,38}

Molecular spectroscopy is usually performed on ensembles of molecules.³⁹ The spectroscopic information is extracted from the response of the ensemble to the external fields.^{40,41} Since the late 1990s, applications in molecular biology, photochemistry, polymer chemistry, quantum optics and other fields have been advanced considerably by the spectroscopic investigation of individual molecules.⁴²⁻⁴⁴ Historically, SM spectroscopic responses were first measured in the frequency domain. The first spectroscopic studies on single molecules date back to 1987,⁴⁶ when Moerner and Carter applied a frequency modulation technique⁴⁷ to detect the homogeneously broadened absorption spectra of pentacene molecules in solids.⁴² In 1990, Orrit and Bernar introduced a technique based on fluorescence detection to study the absorption process of SMs,⁴³ which served as a motivation for latter work in SM detection such as the study of molecules in jets.⁴⁸ The study of single-molecule (SM) responses provides valuable information about specific inter- and intra-molecular processes, which are absent in ensemble studies due to the bulk conditions.⁴⁵ SM responses are free of inhomogeneous broadening, while ensemble experiments can provide only averaged information, in which information about individual molecules is lost. Each chromophore is influenced by its local environment, so that absorption/emission spectra, transition dipole orientation, etc., varies from one chromophore to another. SM experiments indeed show this heterogeneity for chemically identical molecules²⁴. Another important aspect of SM spectroscopy concerns the properties of the laser excitation. Weak laser pulses would not produce a sufficient intensity of the signal. Therefore, strong pulses have to be used and only extremely photostable molecules can be interrogated in this way.

Very recently, ultrafast techniques have been combined with SM spectroscopy. Noteworthy in this respect is the technique developed in the van Hulst group.^{24,49} Using fluorescence detection, they obtained for the first time information about the dynamics

of individual molecules at the femtosecond timescale. In this technique (known as double-pump technique) two phased-locked femtosecond pump pulses interact with a highly photostable single chromophore in a polymer matrix. The fluorescence photons are collected with a confocal microscope as a function of a varying delay time (on the order of femtoseconds) between the two pulses. For individual dyes the detection of vibrational wavepackets has been demonstrated.⁵⁰⁻⁵⁴

In this thesis, specific aspects of femtosecond two-pulse spectroscopies are analyzed, using perturbative as well as nonperturbative theoretical descriptions. The first part deals with ensemble spectroscopy. A previously developed EOM-PMA method^{6,8,55} has been extended towards the inclusion of excited-state absorption (ESA). This extension has permitted the evaluation and comprehensive analysis of transient-absorption pump-probe (TA PP) signals. The main goal was to reveal in detail how the nonadiabatic wavepacket dynamics occurring at crossings of PE functions⁵⁶ can be revealed by the detection of pump-probe (PP) transients. The computational method is based on an exact numerical solution of the driven master equation governing the system dynamics, including coupling to a dissipative environment. A novel aspect of this work is a two-step calculation, involving first the evaluation of so-called *ideal* spectra which exhibit perfect time- and frequency-resolution. In a second step, the measurable *real* spectra are calculated. The ideal spectra contain the maximum level of information for a given spectroscopic signal. The real spectra are obtained through a double convolution of the ideal spectra with an appropriate time and frequency gate (TFG) function, which takes account of the probe mechanism.

In our simulations of TA PP signals, we selected a model system with an intrinsic dynamics which is well understood from previous studies.⁵⁷⁻⁵⁹ It consists of an electronic ground state, two coupled excited electronic states as well as a higher excited electronic state. A single reaction mode of a polyatomic molecule is included, which is weakly coupled to a dissipative bath. The effect of the bath is modeled perturbatively

(in the system-bath coupling) within multi-level Redfield theory.^{57,60} I have performed comprehensive simulations which reveal how the features of the system dynamics are imprinted on the ideal and real TA PP signals.

The second part of this thesis focuses on a theoretical analysis of femtosecond SM spectroscopy. This study was inspired by the recent experimental work of van Hulst and coworkers.⁴⁹ I developed a theoretical description of double-pump femtosecond SM signals with fluorescence detection, exploring the effects of electronic dephasing, heterogeneity in radiation-matter coupling and slow fluctuations of molecular parameters due to the environment. The theoretical model of the chromophore consists of two or three electronic states and a single underdamped high-frequency Franck-Condon active vibrational mode. As emphasized in a review from the van Hulst group,²⁴ both weak and strong coupling regimes are inherent in SM spectroscopy. In the first part of the work I therefore considered weak radiation-matter coupling.⁶¹ In the second part of the work, I extended the analysis to include strong-field effects.⁶² I analyzed the turnover from the weak-field regime to the strong-field regime. It has been found that the signals in both regimes exhibit qualitatively different behaviours.

BACKGROUND

2.1 The Density Operator

In ordinary quantum mechanics (Hilbert space) vector notation is used to represent the state of the system, while matrices are used to represent operators. When using the density operator,^{1,63} the state of the system also is defined by a matrix.

Starting with defining a quantum system described by the wavefunction $|\psi(t)\rangle$, the expectation value of any given operator A reads as

$$\langle A \rangle(t) = \langle \psi(t) | A | \psi(t) \rangle. \quad (2.1)$$

Expanding the wavefunction $|\psi(t)\rangle$ in an arbitrary basis set, $\{|n\rangle\}$ and taking the Hermitian conjugate of the expanded *ket* vector we have

$$|\psi(t)\rangle = \sum_n |n\rangle c_n(t), \quad (2.2)$$

$$\langle \psi(t) | = \sum_m c_m^*(t) \langle m |. \quad (2.3)$$

After the substitution of Eqs. 2.2 and 2.3 in Eq. 2.1, the expectation value of A is given by

$$\langle A \rangle(t) = \sum_{n,m} c_n(t) c_m^*(t) \langle m | A | n \rangle \equiv \sum_{n,m} c_n(t) c_m^*(t) A_{mn}. \quad (2.4)$$

The *density operator* (also known as the density matrix) is defined as

$$\rho(t) \equiv |\psi(t)\rangle\langle\psi(t)|. \quad (2.5)$$

An expansion of the density operator in the previously defined basis $\{|n\rangle\}$ gives

$$\rho(t) = \sum_{n,m} c_n(t) c_m^*(t) |n\rangle\langle m| \equiv \sum_{n,m} \rho_{nm}(t) |n\rangle\langle m|, \quad (2.6)$$

$\rho_{nm}(t) \equiv c_n(t) c_m^*(t)$ being the density operator matrix element. Eq. 2.4 can thus be rewritten as

$$\langle A \rangle(t) = \sum_{n,m} A_{mn} \rho_{nm}(t) \equiv \text{Tr}[A\rho(t)], \quad (2.7)$$

being defined by the *trace* or sum of the diagonal elements for a given operator.

Eq. 2.6 can equivalently be written as

$$\rho(t) = \begin{pmatrix} c_1 c_1^* & c_1 c_1^* & \dots \\ c_1 c_1^* & c_1 c_1^* & \\ \vdots & & \ddots c_N c_N^* \end{pmatrix}. \quad (2.8)$$

When the density matrix of a system is characterized by a single wavefunction, the system is known to be in a *pure* state. However, a general state of a quantum system may not be pure. The system may be in a statistical or mixed state. For an ensemble

of systems being with a given probability distribution in several quantum states, the density operator is defined by

$$\rho(t) \equiv \sum_k P_k |\psi_k(t)\rangle \langle \psi_k(t)|. \quad (2.9)$$

When the system is in a pure state, all probabilities P_k except for one vanish, and the system can be represented by a wavefunction. In a mixed state, the expectation value of any operator A is

$$\langle A \rangle(t) = \sum_k P_k \langle \psi_k(t) | A | \psi_k(t) \rangle = \text{Tr}[A\rho(t)]. \quad (2.10)$$

2.2 The Reduced Density Matrix

As discussed above, the density matrix notation allows us to work with statistical ensembles. Another important aspect is the possibility to describe only a part of the system in which one is interested in, providing a *reduced description*. Let us consider a system-bath Hamiltonian defined as

$$H = H_S(Q) + H_B(q) + H_{SB}(Q, q). \quad (2.11)$$

H_S , H_B and H_{SB} represent the system, a bath, and their interaction, while Q and q refer to the system and bath coordinates. Typically one is interested in monitoring the dynamics of a *system operator*, without being interested in the dynamics of the bath. This way, the complexity of the total density operator reduces dramatically. The expectation value of an operator $A(q_s)$ is given by

$$\langle A(q_s) \rangle(t) = \text{Tr}[\rho(t)A(q_s)]. \quad (2.12)$$

To evaluate the trace, the eigenstates of system and bath can be defined

$$H_s|\lambda\rangle = E_\lambda|\lambda\rangle, \quad (2.13)$$

$$H_B|\beta\rangle = E_\beta|\beta\rangle. \quad (2.14)$$

The direct product states $|\lambda\beta\rangle$ forms a complete basis set

$$\sum_{\lambda\beta} |\lambda\beta\rangle \langle \lambda\beta| = 1. \quad (2.15)$$

Although these states are not eigenstates of the total Hamiltonian in Eq. 2.11 due to H_{SB} , they can be used to evaluate the trace of a system operator according to

$$\text{Tr}\{\rho(t)A(Q)\} = \sum_{\substack{\lambda\mu \\ \beta\alpha}} \langle \lambda\beta|\rho(t)|\mu\alpha\rangle \langle \mu\alpha|A(Q)|\lambda\beta\rangle = \sum_{\substack{\lambda\mu \\ \beta\alpha}} \langle \lambda\beta|\rho(t)|\mu\beta\rangle \langle \mu|A|\lambda\rangle. \quad (2.16)$$

The *reduced system density operator* is defined as

$$\sigma_{\lambda\mu}(t) \equiv \sum_{\beta} \langle \lambda\beta|\rho(t)|\mu\beta\rangle = \text{Tr}_B \langle \lambda|\rho(t)|\mu\rangle. \quad (2.17)$$

According to the first part of the product defined in Eq 2.16, Tr_B denotes the partial trace over the bath degrees of freedom.⁶⁴ The expectation value of $A(Q)$ is thus

$$\langle A(Q) \rangle(t) = \sum_{a,b} \sigma_{ab}(t) A_{ba} \equiv \text{Tr}_S[\sigma(t)A] = \text{Tr}_S(\text{Tr}_B(\rho(t))A), \quad (2.18)$$

where Tr_S denotes the trace over the system degrees of freedom.

2.3 Time Evolution of the Density Operator

The time derivative of the density operator for a pure state is given as

$$\partial_t \rho(t) = \partial_t |\psi(t)\rangle \langle \psi(t)| = (\partial_t |\psi(t)\rangle) \cdot \langle \psi(t)| + |\psi(t)\rangle \cdot (\partial_t \langle \psi(t)|). \quad (2.19)$$

From *Schrödinger equation*, the dynamical behaviour of the density operator reads

$$\partial_t \rho(t) = -i/\hbar [H(t), \rho(t)], \quad (2.20)$$

where $H(t)$ represents a general Hamiltonian operator. Eq. 2.20 is the so-called *Liouville-Von Neumann equation*. When $\rho(t)$ is the density matrix of a pure state, the Schrödinger and the Liouville-von Neumann equations are equivalent. The solution of the Liouville-von Neumann equation contains the time evolution of the diagonal (populations) and off-diagonal (coherences) elements of the density matrix according to

$$\rho(t) = U(t, t_0) \rho(t_0) U^\dagger(t, t_0), \quad (2.21)$$

where U is a time-evolution operator which propagates the ket and the bra acting from the left and right sides, respectively.

For statistical mixtures representing closed systems, the dynamics is also governed by Eq. 2.20. In the case of open systems interacting with an environment, the Liouville

equation can include extra terms accounting for the decoherence of the off-diagonal elements and relaxation among the diagonal elements of the density matrix as

$$\partial_t \rho(t) = -i/\hbar [H(t), \rho(t)] - D\rho(t) + R\rho(t). \quad (2.22)$$

Here D is an operator which accounts for the dephasing of the coherence of the density matrix. That is, the system loses coherence and the off-diagonal elements of the density matrix eventually approach zero. R is another operator accounting for environmental effects on the system dynamics and is called the *relaxation operator*.

The numerical solution of Eq. 2.22 becomes more expensive when the number of system degrees of freedom increases, in comparison to the Schrödinger equation, due to the higher number of coefficients involved. One of the main advantages of the density operator is that it allows us to treat environmental effects that can affect the system dynamics. Environmental degrees of freedom are the intramolecular degrees of freedom not included in $\rho(t)$ as well as the inter-molecular degrees of freedom of the environment, e.g. a solvent. The simplest approach is to account for environmental effects in a phenomenological way, by introducing an empirical *dephasing operator*, D . In contrast to the density operator formalism, it is not possible to describe dephasing in the wavefunction picture. In general, the dissipative operator R accounting for environmental effects is time-dependent and gives rise to non-Markovian dynamics. The simplest description applies in the case of weak system-bath couplings, when the coupling can be treated perturbatively. In this case we can make use of the so-called *Redfield theory*,³³ which will be considered in subsection 2.5.

2.4 Time-Dependent Perturbation Theory. The Interaction Picture

In the context of spectroscopy we are interested in the interaction of molecular systems with external time-dependent electric fields. In this case, the total Hamiltonian $H(t)$ becomes time-dependent and generally given by

$$H(t) = H_0 + H'(t), \quad (2.23)$$

where $H'(t)$ represents a time-dependent external perturbation. When exploring the dynamics of systems interacting with an external perturbation, a very useful approach frequently used in spectroscopy is *perturbation theory*. This approach can be applied only when the time-dependent part in Eq. 2.23 is “small” compared to the system Hamiltonian, H_0 .

In order to get a perturbative solution of the Liouville equation (Eq. 2.20), it is necessary to express the system dynamics in the so-called *interaction picture*. To this purpose, we define the *time-evolution operator* with respect to the system Hamiltonian, H_0 , as

$$U_0(t, t_0) = e^{-\frac{i}{\hbar} H_0 (t - t_0)}. \quad (2.24)$$

We denote by the subindex I the interaction picture. The density matrix in the interaction picture is defined as

$$\rho_I(t) = U_0^\dagger(t, t_0) \rho(t) U_0(t, t_0). \quad (2.25)$$

$\rho_I(t)$ describes the time-evolution of the wavefunction caused exclusively by the time-dependent interaction Hamiltonian, $H'(t)$.

The Liouville von Neumann equation 2.20 in the interaction picture reads

$$\partial_t \rho_I(t) = -\frac{i}{\hbar} [H'_I(t), \rho_I(t)], \quad (2.26)$$

where $H'_I(t) = U_0^\dagger(t, t_0) H'(t) U_0(t, t_0)$. With the Liouville equation in the interaction picture, (Eq. 2.26), the dynamics of the system depends only on the “small” interaction. It is therefore possible to use the perturbative approach for the solution of Eq. 2.26.

In the interacting picture, the first- and second-order perturbative expansions yield Eq. 2.27 and Eq. 2.28:

$$\rho_I^{(1)}(t) = \rho(t_0) - \frac{i}{\hbar} \int_{t_0}^t d\tau H'_I(\tau) \rho(\tau), \quad (2.27)$$

$$\rho_I^{(2)}(t) = \rho_I(t_0) - \frac{i}{\hbar} \int_{t_0}^t d\tau H'_I(\tau) \rho(\tau) + \left(\frac{-i}{\hbar}\right)^2 \int_{t_0}^t d\tau_2 \int_{t_0}^{\tau_2} d\tau_1 H'_I(\tau_2) H'_I(\tau_1) \rho_I(\tau_1). \quad (2.28)$$

Expanding the density matrix to n^{th} order one obtains Eq. 2.29:

$$\begin{aligned} \rho_I^{(n)}(t) = & \rho_I(t_0) + \sum_{n=1}^{\infty} \left(\frac{-i}{\hbar}\right)^n \int_{t_0}^t d\tau_n \int_{t_0}^{\tau_{n-1}} d\tau_{n-1} \dots \\ & \dots \int d\tau_1 [H'_I(\tau_n), [H'_I(\tau_{n-1}), \dots [H'_I(\tau_1), \rho_I(t_0)] \dots]]. \end{aligned} \quad (2.29)$$

In the Schrödinger picture, this reads

$$\rho^{(n)}(t) = \rho^{(0)}(t) + \sum_{n=1}^{\infty} \left(\frac{-i}{\hbar}\right)^n \int_{t_0}^t d\tau_n \int_{t_0}^{\tau_{n-1}} d\tau_{n-1} \dots$$

$$\dots \int_{t_0}^{\tau_2} d\tau_1 U_0(t, t_0) \cdot [H'_I(\tau_n), [H'_I(\tau_{n-1}), \dots [H'_I(\tau_1), \rho(t_0)] \dots]] \cdot U_0^\dagger(t, t_0). \quad (2.30)$$

In Eq. 2.30, the interaction Hamiltonian is still in the interaction picture.

Considering an explicit interaction Hamiltonian in the dipole approximation described by

$$H'(t) = E(t) \cdot \mu, \quad (2.31)$$

Eq. 2.30 transforms into

$$\begin{aligned} \rho^{(n)}(t) = & \left(\frac{-i}{\hbar} \right)^n \int_{-\infty}^t d\tau_n \int_{-\infty}^{\tau_{n-1}} d\tau_{n-1} \dots \int_{-\infty}^{\tau_2} d\tau_1 E(\tau_n) E(\tau_{n-1}) \cdot \dots \cdot E(\tau_1) \\ & \dots U_0(t, t_0) \cdot [\mu(\tau_n), [\mu(\tau_{n-1}), \dots [\mu(\tau_1), \rho(-\infty)] \dots]] \cdot U_0^\dagger(t, t_0), \end{aligned} \quad (2.32)$$

where the dipole operator μ in the interaction picture, μ_I , is defined as

$$\mu_I(t) = \mu(t) = U_0^\dagger(t, t_0) \mu U_0(t, t_0). \quad (2.33)$$

Note that the dipole operator becomes time-dependent in the interaction picture since it evolves under the effect of the system Hamiltonian H_0 .

2.5 Redfield Theory for Open Quantum Systems

In this thesis, I restrict myself to the case of a system described by a single reaction mode coupled to the electronic states which is at the same time weakly coupled to a

dissipative environment, modeled within the linear response theory. This approach was first introduced by Jean *et al*⁶⁵ who adopted Redfield theory for relaxation.³³

The general model established for describing dissipative dynamic processes consists of several electronic energy levels coupled to a set of fluctuating coordinates. This general model can explain a broad number of processes occurring in nature, for example, electron transfer processes.

Within Redfield theory,³³ the system is weakly coupled to a dissipative environment, which allows a perturbative treatment of the system-bath coupling (Born approximation). This situation corresponds to the case when a single or a few reaction modes are part of the system, the rest of vibrational degrees of freedom being part of the bath. The perturbative treatment simplifies considerably the numerical treatment of the problem.

In the reduced density matrix (RDM) formalism, we denote the reduced density matrix by $\sigma(Q, t)$, where Q is the system reaction mode which is considered to be (weakly) coupled to the bath.

The following derivations were taken from references 33 and 66. The dynamics of the system embedded in a dissipative environment in the RDM formalism^{64,67} is governed by the following master equation

$$\partial_t \sigma = -i[H_0, \sigma] + \mathcal{R}(\sigma). \quad (2.34)$$

$\mathcal{R}(\sigma)$ is the so-called Redfield operator, which is defined by

$$\mathcal{R}(\sigma) = - \int_0^t d\tau \text{tr}_B \{ [H_{SB}, [H_{SB}(\tau), \sigma(t) \rho_B]] \}, \quad (2.35)$$

where H_{SB} is the system-bath interaction Hamiltonian in the interaction picture (introduced in section 2.4),

$$H_{SB}(\tau) = e^{-i(H_S+H_B)\tau} H_{SB} e^{i(H_S+H_B)\tau} \quad (2.36)$$

and ρ_B represents the equilibrium bath density matrix,

$$\rho_B = \frac{e^{-H_B/kT}}{\text{tr}_B\{e^{-H_B/kT}\}}. \quad (2.37)$$

Redfield theory is formulated in the system eigenstate representation defined by

$$H_0|\lambda\rangle = E_\lambda|\lambda\rangle. \quad (2.38)$$

In this representation, Redfield equation (Eq. 2.34) adopts the following form³³,

$$\partial_t \sigma_{\lambda\mu}(t) = -i\omega_{\lambda\mu} \sigma_{\lambda\mu}(t) + \sum_{\alpha\beta} R_{\lambda\mu\alpha\beta} \sigma_{\alpha\beta}(t), \quad (2.39)$$

where $\sigma_{\lambda\mu} = \langle \lambda | \sigma | \mu \rangle$ and $\omega_{\lambda\mu} = E_\lambda - E_\mu$. The first term on the right-hand side of Eq. 2.39 represents the system dynamics in the absence of the environment. The second term, which is given by:

$$\sum_{\alpha\beta} R_{\lambda\mu\alpha\beta} \sigma_{\alpha\beta}(t) = \langle \lambda | \mathcal{R}(\sigma) | \mu \rangle, \quad (2.40)$$

governs the relaxation dynamics of the system due to the presence of the bath. $R_{\lambda\mu\alpha\beta}$, the so-called Redfield tensor, is defined as follows:

$$R_{\lambda\mu\alpha\beta} = \Gamma_{\beta\mu\lambda\alpha}^+ + \Gamma_{\beta\mu\lambda\alpha}^- - \delta_{\mu\beta} \sum_{\kappa} \Gamma_{\lambda\kappa\kappa\alpha}^+ - \delta_{\lambda\alpha} \sum_{\kappa} \Gamma_{\beta\kappa\kappa\mu}^-. \quad (2.41)$$

Here,

$$\Gamma_{\beta\mu\lambda\alpha}^+ = \int_0^t d\tau \langle\langle \beta | H_{SB} | \mu \rangle \langle \lambda | \tilde{H}_{SB} | \alpha \rangle \rangle_B e^{-i\omega_{\lambda\alpha}\tau}, \quad (2.42)$$

$$\Gamma_{\beta\mu\lambda\alpha}^- = \int_0^t d\tau \langle\langle \beta | \tilde{H}_{SB} | \mu \rangle \langle \lambda | H_{SB} | \alpha \rangle \rangle_B e^{-i\omega_{\beta\mu}\tau}, \quad (2.43)$$

$\tilde{H}_{SB}(\tau) = e^{-iH_B\tau} H_{SB} e^{iH_B\tau}$, and $\langle\langle \dots \rangle\rangle$ denotes a trace taken over the bath degrees of freedom.

The Hamiltonian H_{SB} , is usually expressed as a sum of the type

$$H_{SB} = \sum_n Q_n F_n, \quad (2.44)$$

considering the different system and bath operators, Q_n and F_n , respectively. With Eq. 2.44, the Redfield operator adopts the form

$$\mathcal{R}(\sigma) = \sum_{nm} \int_0^t d\tau \{ [Q_n, Q_m(\tau) \sigma(t)] \langle F_n F_m(\tau) \rangle_B - [Q_m, \sigma(t) Q_n(\tau)] \langle F_n(\tau) F_m \rangle_B \},$$

where $Q_n(\tau) = e^{-iH_S\tau} Q_n e^{iH_S\tau}$ is determined by the system Hamiltonian and $F_n(\tau) = e^{-iH_B\tau} F_n e^{iH_B\tau}$, is determined by the bath Hamiltonian.

The tensor components (given by Eqs. 2.42 and 2.43) can now be expressed as

$$\Gamma_{\beta\mu\lambda\alpha}^+ = \sum_{nm} \langle \beta | Q_n | \mu \rangle \langle \lambda | Q_m | \alpha \rangle \int_0^t d\tau \langle F_n F_m(\tau) \rangle_B e^{-i\omega_{\lambda\alpha}\tau} \quad (2.45)$$

$$\Gamma_{\beta\mu\lambda\alpha}^- = \sum_{nm} \langle \beta | Q_n | \mu \rangle \langle \lambda | Q_m | \alpha \rangle \int_0^t d\tau \langle F_n(\tau) F_m \rangle_B e^{-i\omega_{\beta\mu}\tau} \quad (2.46)$$

In the case of a single system reaction mode Q and a linear system-bath interaction

$$H_{SB} = Q \sum_q g_q q_q \quad (2.47)$$

There exist a number of models which were developed to describe the bath.

^{36,68} The bath is usually described in the harmonic approximation, that is, as a collection of harmonic oscillators:

$$H_B = \sum_q \frac{\omega_q}{2} (p_q^2 + q_q^2), \quad (2.48)$$

p_q and q_q being the dimensionless coordinate and momentum operators. The system-bath coupling is described by the spectral function

$$J(\omega) = \frac{\pi}{2} \sum_q g_q^2 \delta(\omega - \omega_q). \quad (2.49)$$

The bath correlation functions are defined by:

$$\langle FF(\tau) \rangle_B = \int_0^\infty d\omega \frac{1}{\pi} J(\omega) (e^{-i\omega\tau} + 2n(\omega)\cos(\omega\tau)), \quad (2.50)$$

$$\langle F(\tau)F \rangle_B = \langle FF(\tau) \rangle_B^* = \int_0^\infty d\omega \frac{1}{\pi} J(\omega) (e^{i\omega\tau} + 2n(\omega)\cos(\omega\tau)), \quad (2.51)$$

where $F = \sum_q g_q q_q$ and $n(\omega) = 1/(e^{\omega/kT} - 1)$ is the Bose distribution function.

We consider the specific case of the *Ohmic spectral density*⁶⁹

$$J(\omega) = \eta\omega e^{-\omega/\omega_c}, \quad (2.52)$$

where η is a dimensionless parameter specifying the system-bath coupling strength and ω_c is a bath cut-off frequency.

In the present work, I apply an additional approximation to the general Redfield formalism, which is called the *Markovian approximation*. The system dynamics is Markovian if the bath correlation function decays to zero at a short time scale. Under this condition, it can be assumed that the Redfield tensor is time independent and can be evaluated as:

$$\Gamma_{\beta\mu\lambda\alpha}^+ = \langle\beta|Q|\mu\rangle\langle\lambda|Q|\alpha\rangle \int_0^\infty d\tau \int_0^\infty d\omega \frac{1}{\pi} J(\omega) (e^{-i\omega\tau} + 2n(\omega)\cos(\omega\tau)) e^{-i\omega\lambda\alpha\tau}, \quad (2.53)$$

$$\Gamma_{\beta\mu\lambda\alpha}^- = \langle\beta|Q|\mu\rangle\langle\lambda|Q|\alpha\rangle \int_0^\infty d\tau \int_0^\infty d\omega \frac{1}{\pi} J(\omega) (e^{i\omega\tau} + 2n(\omega)\cos(\omega\tau)) e^{-i\omega\lambda\alpha\tau}. \quad (2.54)$$

The Markovian approximation considerably simplifies the numerics. Redfield theory can also be expressed in the eigenstate representation of the reaction mode (so-called multilevel Redfield theory⁶⁵).

THEORY OF NONLINEAR OPTICAL SPECTROSCOPY: RESPONSE
FUNCTIONS

3.1 Basic Concepts in Time and Frequency Resolved Spectroscopy

In spectroscopy, the optical polarization P constitutes the main observable for the interpretation of time- or frequency-domain spectroscopic measurements. The dynamics of the electronic and nuclear degrees of freedom of the system and the environment-induced relaxation processes will affect the optical polarization. Thus, the calculation of the optical polarization is the primary goal of the theory of time and frequency resolved spectroscopy.

Different spectroscopic techniques can be classified according to the dependence of the induced polarization on the electric fields. The *linear* polarization is given by

$$P^{(1)} = \epsilon_0 \chi^{(1)} E, \quad (3.1)$$

where ϵ_0 represents the dielectric constant, $\chi^{(1)}$ is the linear susceptibility of the medium, and E is the field amplitude. If multiple laser fields interact with the system or if the intensity of the field is high enough the *nonlinear* polarization is required. It is defined via an expansion in powers of the electric field amplitude E as

$$P_{NL}^{(n)} = \epsilon_0 \left(\sum_n \chi^{(n)} E^{(n)} \right), \quad (3.2)$$

where $\chi^{(n)}$ represent the nonlinear susceptibilities. In isotropic media, even-order optical susceptibilities vanish due to the isotropy of the environment. In practice, the most common low-order nonlinear spectroscopic techniques are based on the 3rd-order nonlinear polarization.

The optical polarization can be expressed as the expectation value of the dipole operator μ :

$$P^{(n)}(t) = \text{Tr}(\mu \rho^{(n)}(t)) \equiv \langle \mu \rho^{(n)}(t) \rangle, \quad (3.3)$$

where $\rho^{(n)}(t)$ is n^{th} -order term in the perturbative expansion of the density matrix. Eq. 3.3 shows that the electronic off-diagonal elements of the density matrix are the source of the field-induced macroscopic polarization and the emitted light field. In other words, the creation of electronic coherence elements in the density matrix by the interaction with an external field gives rise to the polarization.

Making use of the perturbative expansion of the density matrix given by Eq. 2.30, the n^{th} -order polarization can be calculated by a n -fold convolution with the external fields:

$$P^{(n)}(t) = \left(\frac{-i}{\hbar} \right)^n \int_0^\infty dt_n \int_0^\infty dt_{n-1} \dots \int_0^\infty dt_1 E(t-t_n) E(t-t_n-t_{n-1}) E(t-t_n-\dots-t_1) \times$$

$$\langle \mu(t_n + t_{n-1} + \dots t_1) \cdot [\mu(t_{n-1} + \dots + t_1), \dots [\mu(0), \rho(-\infty)] \dots] \rangle, \quad (3.4)$$

where $\mu(t) = U_0^\dagger(t, t_0) \mu U_0(t, t_0)$ represents the dipole operator in the interaction picture.

As it can be seen from Eq. 3.4, the system described by the initial density matrix $\rho(-\infty)$ interacts $n - 1$ times with the external field, bringing the system to an electronic coherence state (if n is odd) or population state (if n is even). The last interaction, which originates from the detection of the signal, finally brings the system to a population state.

3.2 The Perturbative Approach: Nonlinear Response Functions

Perturbation theory is the standard approach used to describe the dynamics of a material system interacting with an external electromagnetic field. One of the main reasons of using perturbation theory in spectroscopy is the possibility of classification and bookkeeping of the different processes that can occur during the interaction of the molecular system with the external fields. This renders it convenient for the interpretation of spectroscopic signals of any material system.

The perturbative approach is restricted to weak (considerably weaker than the intramolecular couplings) field-matter couplings. Beyond this limit, nonperturbative approaches should be used (see chapter 4).

The nonlinear polarization $P^{(n)}(t)$ of Eq. 3.4 is a convolution of n electric fields with the n^{th} -order *nonlinear response function*

$$S^{(n)}(t_n, \dots, t_1) = \left(\frac{-i}{\hbar} \right)^n \langle \mu(t_n + t_{n-1} + \dots + t_1) \cdot [\mu(t_{n-1} + \dots + t_1), \dots [\mu(0), \rho(-\infty)] \dots] \rangle. \quad (3.5)$$

The n^{th} -order response function scales with the transition dipole moment as

$$S^{(n)}(t_n + t_{n-1} + \dots + t_1) \propto \mu_{nm}^{n+1}. \quad (3.6)$$

The commutators in Eq. 3.5 contain 2^n terms characterized by various number of interactions acting on the bra and ket vectors of the density matrix. There are always pairs of terms which are the complex conjugate to each other. It is sufficient to consider the 2^{n-1} independent terms.

3.3 Reduction of the Number of Coherent Pathways

As mentioned in the previous section, the commutators in Eq. 3.5 contain multiple terms originating from different interactions with the electric field. This leads to a relatively large number of possible coherent pathways. There exist several techniques or approximations to reduce the number of these terms. Among these, I discuss the *rotating wave approximation (RWA)* and the phase-matching conditions.

3.3.1 The Rotating Wave Approximation

The rotating wave approximation (RWA)⁷⁰ implies the neglect of high-oscillatory terms in the equations of motion describing the system dynamics after excitation. Let H_0 be the molecular Hamiltonian. For illustration, let us consider a two-level system

$$H_0 = \begin{pmatrix} \epsilon_1 & 0 \\ 0 & \epsilon_2 \end{pmatrix}, \quad (3.7)$$

represented by the density matrix

$$\rho = \begin{pmatrix} \rho_{11} & \rho_{12} \\ \rho_{21} & \rho_{22} \end{pmatrix}. \quad (3.8)$$

In the dipole approximation the total Hamiltonian describing interaction of the system with a time-dependent monochromatic external field takes the form

$$H(t) = \begin{pmatrix} \epsilon_1 & -\mu E(t) \\ -\mu E(t) & \epsilon_2 \end{pmatrix}, \quad (3.9)$$

where the electric field is given by

$$E(t) \equiv 2E_0 \cos(\omega t) = E_0(e^{i\omega t} + e^{-i\omega t}), \quad (3.10)$$

which is assumed to be in near resonance with the system energy splitting: $(\epsilon_1 - \epsilon_2)/\hbar \sim \omega$. Here, ω is the frequency of the field, E_0 is its amplitude, and μ is the transition dipole moment operator.

In the presence of an external field, the coherences of the density matrix oscillate with the frequency of the field, ω . The diagonal elements are time-dependent, but do not oscillate with the frequency ω and become stationary when the electric field is turned off. We invoke the RWA⁷¹ as follows. The dynamics of the system in the absence of the field obeys¹

$$\rho_{11}(t) = \rho_{11}(0), \quad (3.11)$$

$$\rho_{22}(t) = \rho_{22}(0), \quad (3.12)$$

for the diagonal and

$$\rho_{12}(t) = e^{i\frac{(\epsilon_1 - \epsilon_2)}{\hbar}t} \rho_{12}(0), \quad (3.13)$$

$$\rho_{21}(t) = e^{-i\frac{(\epsilon_1 - \epsilon_2)}{\hbar}t} \rho_{21}(0), \quad (3.14)$$

for the off-diagonal elements of the density matrix represented by Eq. 3.8.

We can define the evolution of the off-diagonal elements represented by Eqs. 3.13 and 3.14 in the so-called *rotating frame* (represented by tilde), which implies the transformation with additional frequency factors⁹

$$\tilde{\rho}_{12}(t) = e^{-i\omega t} \rho_{12}(t), \quad (3.15)$$

$$\tilde{\rho}_{21}(t) = e^{+i\omega t} \rho_{21}(t), \quad (3.16)$$

for the off-diagonal elements of the density matrix, while the diagonal terms remain unchanged

$$\tilde{\rho}_{11}(t) = \rho_{11}(t), \quad (3.17)$$

$$\tilde{\rho}_{22}(t) = \rho_{22}(t). \quad (3.18)$$

With this transformation, the off-diagonal elements vary slowly since for a near resonant field the additional frequency factors in Eqs. 3.15 and 3.16 almost cancel the natural evolution of the coherences. The Liouville equation under this framework reads⁹

$$\begin{pmatrix} \dot{\tilde{\rho}}_{12} \\ \dot{\tilde{\rho}}_{21} \\ \dot{\tilde{\rho}}_{11} \\ \dot{\tilde{\rho}}_{22} \end{pmatrix} = -i \begin{bmatrix} \Delta & 0 & -\tilde{\Omega}(t) & \tilde{\Omega}(t) \\ 0 & -\Delta & \tilde{\Omega}^*(t) & -\tilde{\Omega}(t) \\ -\tilde{\Omega}^*(t) & \tilde{\Omega}(t) & 0 & 0 \\ \tilde{\Omega}^*(t) & -\tilde{\Omega}(t) & 0 & 0 \end{bmatrix} \begin{pmatrix} \tilde{\rho}_{12} \\ \tilde{\rho}_{21} \\ \tilde{\rho}_{11} \\ \tilde{\rho}_{22} \end{pmatrix}, \quad (3.19)$$

where Δ is the frequency detuning given by

$$\Delta \equiv (\epsilon_1 - \epsilon_2)/\hbar + \omega, \quad (3.20)$$

and

$$\tilde{\Omega}(t) = \Omega \cdot (1 + e^{i2\omega t}) = \Omega \cdot (e^{-i\omega t} + e^{i\omega t})e^{i\omega t}. \quad (3.21)$$

Eq. 3.21 possesses a time-independent (zero-frequency) contribution and a contribution which oscillates as $e^{i2\omega t}$. When integrating the Liouville equation (Eq. 2.20), only the term which rotates in the same direction as the rotating frame will survive. Due to the highly-oscillatory integrand, the second integral is almost zero. In other words, we are neglecting the fast oscillating part of the field, keeping the slowly varying envelope. To illustrate the RWA for a simple case, let us consider the 1st order polarization,

$$P^{(1)}(t_1) = -\frac{i}{\hbar}\mu_{01}^2 e^{-i\omega t} \int_0^\infty dt_1 E(t-t_1) e^{-\Gamma t_1} - \frac{i}{\hbar}\mu_{01}^2 e^{+i\omega t} \int_0^\infty dt_1 E(t-t_1) e^{-\Gamma t_1} e^{-i2\omega t_1} \quad (3.22)$$

The RWA is valid in near resonant conditions, $\Delta \sim \omega$, and when the electric field envelope varies slowly in time (much slower than the optical period, $2\pi/\omega$). This approximation reduces the number of Liouville pathways by a factor of 2.

3.3.2 The Phase Matching Condition

Each of the spectroscopic techniques corresponds to a specific *phase matching condition*, that is a linear combination of the incoming wavevectors, which defines the direction of the emitted polarization⁷². This condition is selected experimentally by designing the geometry of the experimental setup. This reduces the possible coherent pathways for a given spectroscopic technique.

The explicit dependence of the external field on the wavevectors \vec{k} is as follows

$$E(t) = E_0(e^{-i\omega t + i\vec{k}\vec{r}} + e^{+i\omega t - i\vec{k}\vec{r}}) \quad (3.23)$$

In the case of n electric fields, the total n^{th} -order polarization will carry the wavevector

$$\vec{k}_{\text{signal}} = \sum_n \pm \vec{k}_n. \quad (3.24)$$

By choosing a specific linear combination in Eq. 3.24, we select a particular contribution to the signal.

Let us imagine two third-order experiments with pulses of identical frequency ($\omega_1 = \omega_2 = \omega_3 = \omega_{\text{signal}}$), which can be distinguished by the time-ordering of the pulses for

a given signal direction. Assuming a box geometry for the three incident fields, the radiated signal will be directed towards the upper right corner of the box, see Fig. 3.1 for the signal detected in the direction $\vec{k}_{signal} = +\vec{k}_a - \vec{k}_b + \vec{k}_c$, the so-called rephasing and non-rephasing contributions correspond to different time-orderings of the pulses

$$a = 1, b = 2, c = 3,$$

for the non-rephasing case and

$$a = 2, b = 1, c = 3,$$

for the rephasing case.

These definitions can be illustrated a simple way as shown in Figure 3.1:

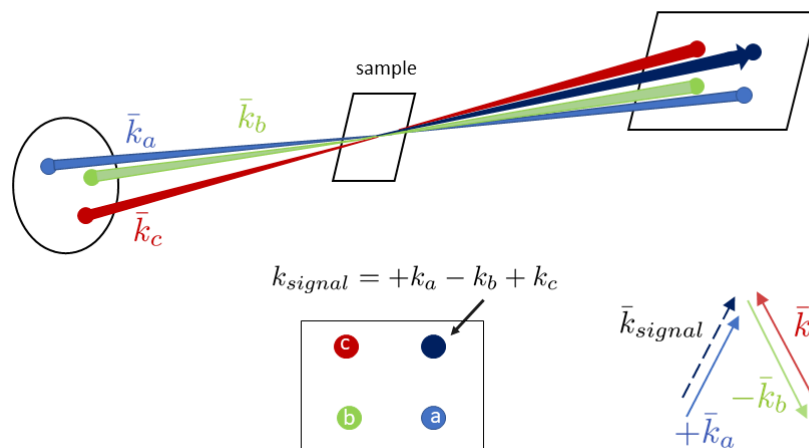


Figure 3.1: Definition of the signal wavevector for a box geometry for a specific phased-matched direction. The rephasing and non-rephasing situations correspond to different time ordering of the three incoming fields. (Adapted from: *Time-dependent Quantum Mechanics and Spectroscopy Lectures*, Andrei Tokmakoff, University of Chicago, 2014).

3.4 Representative Non-Linear Optical Spectroscopies and the Corresponding Response Functions

In ultrafast spectroscopy, the various techniques can be classified according to the order of the nonlinear response function representing the measured polarization. They differ in several aspects, like the detection mechanism as well as the number and properties of the fields involved.¹ Each of the techniques delivers specific information about the system dynamics.

In this section, representative spectroscopies will be discussed in the framework of nonlinear response functions. I start by introducing the simplest technique, linear absorption spectroscopy, and consecutively move towards some of the common higher-order techniques. The idea behind the approach taken here is to connect particular signals with their microscopic origin. To illustrate the processes involved in the different techniques I consider the previously introduced two-level model given by Eq. 3.8.

3.4.1 Linear Absorption Spectroscopy

The simplest case that can occur is characterized by a linear scaling of the polarization with the electric field. This is the *linear absorption* process, which is characterized by the 1st order response function¹

$$S^{(1)}(t_1) = \frac{-i}{\hbar} \langle \mu(t_1) [\mu(0), \rho(-\infty)] \rangle.$$

Adopting the RWA and within the impulsive limit ($E_0(t) \sim E_0 e^{i\omega t} \delta(t)$) the 1st order polarization is given by:

$$P^{(1)}(t_1) = -\frac{i}{\hbar} \mu_{01}^2 e^{-i\omega t} E_0 e^{-\Gamma t_1} \tag{3.25}$$

The resulting polarization emits an electric field:

$$EP^{(1)}(t) \propto -iP^{(1)}(t), \tag{3.26}$$

and its time dependence determines the so-called *free induction decay*.

In the RWA, the number of Liouville pathways reduces to two, which are complex conjugate to each other. Considering only the process with the last interaction on the ket, we have the following Liouville pathway:

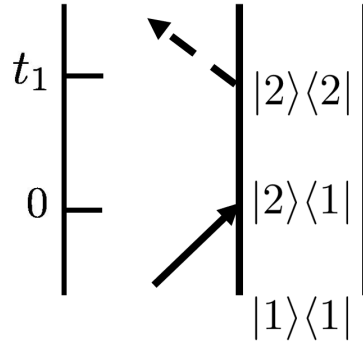


Figure 3.2: Liouville pathway for linear spectroscopy. The solid arrow represents the interaction with the external fields. An arrow pointing to the right represents an electric field with $e^{-i\omega t + ikr}$, while an arrow pointing to the left represents an electric field with $e^{+i\omega t - ikr}$. Arrows pointing outside the system represent de-excitations, while the opposite represent excitation processes. The signal is generated by the last interaction with the transition dipole moment outside the commutator, which has different nature than the previous interactions. Therefore, a different arrow (dashed) is used to represent the emitted signal.

The system initially is in the electronic ground state. After excitation by the laser pulse at time 0, a coherent state is generated with propability proportional to the transition dipole moment

$$\rho_{12}(0) \propto \mu_{12}. \quad (3.27)$$

This coherent state evolves in time according to

$$\rho_{12}(t) \propto \mu_{12} e^{-\frac{i}{\hbar}(\epsilon_2 - \epsilon_1)t_1} e^{-\Gamma t_1}, \quad (3.28)$$

where Γ is the dephasing rate of the transition. At time t_1 the system emits a light field described by Eq. 3.26. Due to this interaction with the transition dipole operator the system returns to a population, either in the electronic ground state or in the excited electronic state.

When detecting the linear emitted field, an inherent measurement of the incoming field is done along with the signal, since the incoming field is transmitted in the same direction as the emitted field, as seen in Equation 3.25. Since the first order polarization is always *heterodyne* detected (by using the input laser pulse as a local oscillator) and the second order terms of the polarization are small compared to the first order, we can use Eq. 3.28 to calculate the absorption spectrum. After taking Fourier transform with respect to the time variable we obtain

$$A(\omega) = \frac{2\Gamma}{(\omega - \omega_0)^2 + \Gamma^2}. \quad (3.29)$$

A general expression for the linear absorption spectrum reads

$$A(\omega) \propto 2R \int_0^\infty dt \cdot e^{i\omega t} \langle \mu(t) \mu(0) \rho(-\infty) \rangle. \quad (3.30)$$

3.4.2 Pump-probe Spectroscopy

One of the most common time-resolved third-order techniques is the pump-probe transient-absorption (PP TA) spectroscopy.¹ This technique can be used to record many types of time-dependent processes which manifest themselves in the population dynamics, such as relaxation processes, chemical dynamics, wavepacket dynamics and quantum beats. In such experiments, the molecular system is initially prepared by a first *pump* laser pulse into a nonequilibrium state. The dynamics of the new state is probed by an interaction with a second *probe* laser pulse. The probe pulse is delayed in time with respect to the pump pulse.

The transient transmittance PP signal is defined through the difference polarization⁵

$$\tilde{P}_{PP}(t) = P_{PP}(t) - P^{\text{off}}(t),$$

where $P^{\text{off}}(t)$ is the polarization induced solely by the probe pulse.

In general, when the pulses are in resonance with the electronic excitation in the system, the PP signal contains two contributions. Both of them reflect the system dynamics and report different information: the resonance Raman contribution (reflecting electronic ground-state dynamics) also called GSB, and the SE contribution (reflecting electronic excited state dynamics).⁷³ If transitions to higher-lying electronic excited states cannot be neglected, the PP signal also contains the ESA contribution.

The measured 3rd order polarization is detected in the direction of the probe pulse. To fulfill this condition, the pump pulse must interact twice with the system with wave vectors $+k_{pump}$ and $-k_{pump}$. This defines the *phase-matching condition* of TA PP spectroscopy

$$k_{PP} = +\vec{k}_{pu} - \vec{k}_{pu} + \vec{k}_{probe} = +\vec{k}_{probe}.$$

In PP spectroscopy, the time delay between the pump and the probe fields determines the sequence of the interactions. Hence, the system interacts first with the pump pulse (two interactions) and then with the probe pulse (last interaction). Therefore, the contributions originating from other sequences of interactions will not be present in the signal. If the pump and the probe pulses overlap in time, additional contributions must be considered, constituting the so-called coherence spike or coherent artefact.¹ Overlapping pulses should be avoided since the pulse overlap complicates the interpretation of the signal. Due to the phase-matching condition and in the RWA, the Liouville pathways for the possible coherent processes that take place in a TA PP measurement reduce to six. Figure 3.3 shows these diagrams in detail.¹

After the two interactions with the pump pulse at times t_1 and t_2 , the system ends up in a population state (excited electronic state for the SE and ESA contributions, or ground electronic state for the GSB contribution). This state shows dynamical evolution with respect to the probe time-delay. The third interaction is produced by the probe pulse at t_3 , which brings the system into a coherent state, with probability μ_{12} .

The PP signal is given by the 3rd order polarization. As shown in the diagrams in Figure 3.3, there are three different kinds of nonlinear response functions for the stimulated emission, ground state bleach and excited-state absorption contributions:

$$S_{SE}^{(3)}(t_3, t_2, t_1) \propto \frac{i}{\hbar^3} \mu_{21}^4 e^{-i\frac{(\epsilon_2 - \epsilon_1)}{\hbar} t_3} e^{-\Gamma t_3}, \quad (3.31)$$

$$S_{Bl}^{(3)}(t_3, t_2, t_1) = S_{SE}^{(3)}(t_1, t_2, t_3), \quad (3.32)$$

$$S_{ESA}^{(3)}(t_3, t_2, t_1) \propto -\frac{i}{\hbar^2} \mu_{10}^2 \mu_{32}^{(2)} e^{-i\frac{(\epsilon_3 - \epsilon_2)}{\hbar} t_3} e^{-\Gamma t_3}. \quad (3.33)$$

The 3rd order response function $S^{(3)}$ is the sum of the above three contributions. Considering Dirac delta pulses, $S^{(3)}$ is equal to the 3rd-order polarization.

There are two different techniques to measure the PP signal. When the emitted field is directly measured as it emerges from the sample, the *time-integrated* signal is measured. If the emitted field is passed through a spectrometer dispersing the light the *dispersed* signal is measured. The integrated and dispersed PP signals are defined as

$$S_{PP}^{int}(\tau, \omega_{pr}) = \text{Im} \int_{t_0}^{\infty} E_P(t - \tau) e^{-i\omega t} P_{PP}(t), \quad (3.34)$$

and

$$S_{PP}^{disp}(\tau, \omega_{pr}, \omega) = \text{Im} E_P(\omega - \omega_P) P_{PP}(\omega) \quad (3.35)$$

respectively, where

$$P_{PP}(\omega) = \int_{-\infty}^{\infty} dt e^{i\omega t} P_{PP}(t), \quad (3.36)$$

$$E_P(\omega) = \int_{-\infty}^{\infty} dt e^{i\omega t} E_P(t - \tau). \quad (3.37)$$

Two-pulse femtosecond stimulated Raman spectroscopy (FSRS) can be viewed as a special case of PP spectroscopy,⁷⁴⁻⁷⁶ with a long (picosecond) pump pulse and a short (femtosecond) probe pulse.

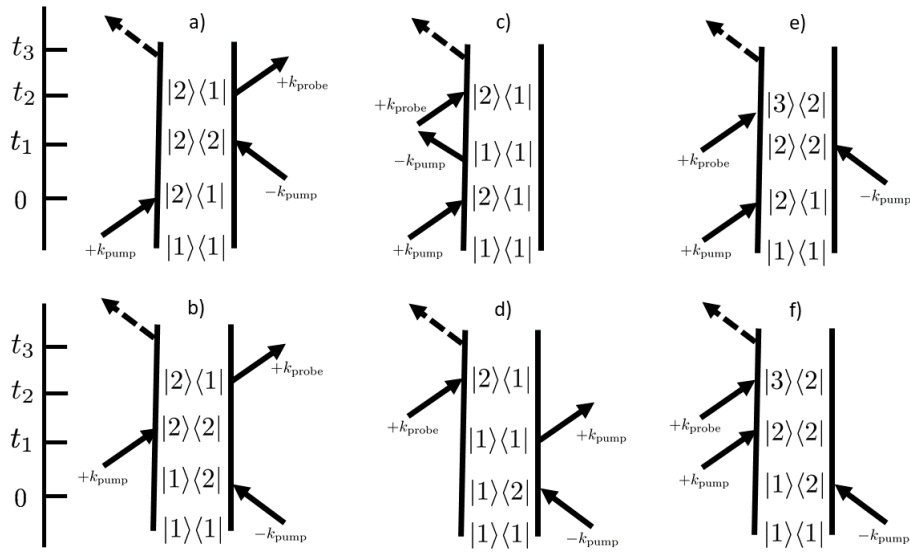


Figure 3.3: Pump probe Liouville pathways.¹ Figures a) and b) correspond to stimulated emission, c) and d) correspond to the ground-state bleach and d) and f) correspond to excited-state absorption contributions. There are two different kinds of arrows in these diagrams. The solid arrows represent an interaction with the external fields. An arrow pointing to the right represents an electric field with $e^{-i\omega t + ikr}$, while an arrow pointing to the left represents an electric field with $e^{+i\omega t - ikr}$. Arrows pointing outside the system represent de-excitations while the opposite represents excitation processes. The signal is generated by the last interaction with the transition dipole moment outside the commutator. A dashed arrow is used to represent the emitted signal.

3.4.3 Two-Pulse Photon-Echo Spectroscopy

Another common third-order spectroscopy is the so-called *two-pulse photon-echo* (2PPE) spectroscopy. This technique is commonly used to distinguish static and dynamic broadening of spectral features, as well as to determine time scales of energy gap fluctuations. This is usually done making use of the rephasing definition of the signal.

In this technique, two pulses interact with the sample with wavevectors k_1 and k_2 . The third-order polarization is detected in the phase-matching direction given by

$$\vec{k}_{2PPE} = +2\vec{k}_2 - \vec{k}_1. \quad (3.38)$$

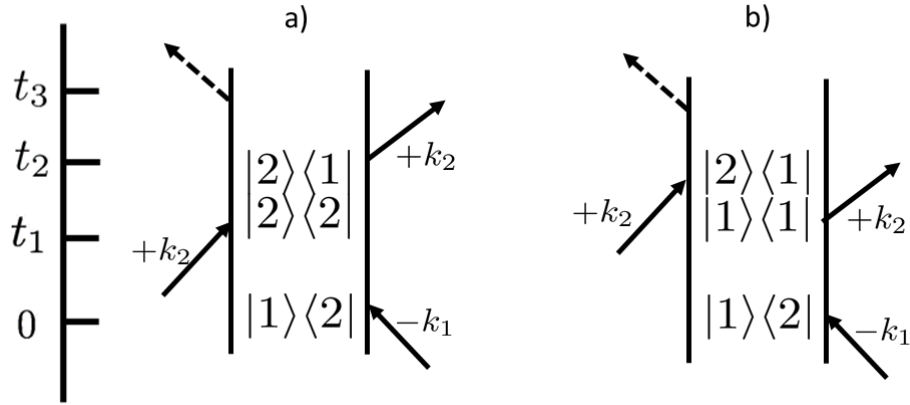


Figure 3.4: Two-pulse photon echo Liouville pathways¹. Two-pulse photon echo Liouville pathways. See caption of Fig 3.3 for the explanation of the symbol.

This implies that the system interacts twice with the second pulse. In contrast with the PP experiment, the signal is detected in a direction which differs from the direction of the incoming fields. This last aspect implies a *homodyne* detection of the signal, that is $|P^{(3)}|^2$, in contrast to the *heterodyne* detection defined by $E_0P^{(3)}$.

Within the RWA, the Feynman diagrams contributing to the signal are depicted in Figure 3.4.

For both diagrams a) and b), the system is prepared in a coherence state after the single interaction with pulse 1. The evolution of such a coherence state along t_1 is given by Eq. 3.28, with a phase determined by $e^{i\omega t_1}$. The first interaction with the second pulse converts the system to a population state. The second interaction with this pulse creates again a coherence state, which oscillates now with an opposite sign of the phase, $e^{-i\omega t_3}$. This phenomenon is called *rephasing*, motivated by the presence of the inhomogeneous broadening in the media. This rephasing, which occurs at a specific separation time between both pulses, gives name to the *echo* technique.¹

Assuming pulses in the impulsive limit, we can neglect the time separation t_2 between the last two interactions occurring within the same pulse. The third-order response function is given then by¹

$$S_{2PPE}^{(3)}(t_3, t_2, t_1) \propto \frac{i}{\hbar^3} \mu_{21}^4 e^{+i\frac{(\epsilon_2 - \epsilon_1)}{\hbar} t_1} e^{-i\frac{(\epsilon_2 - \epsilon_1)}{\hbar} t_3} e^{-\Gamma t_3} = \frac{i}{\hbar^2} \mu_{21}^4 e^{-i\frac{(\epsilon_2 - \epsilon_1)}{\hbar} (t_3 - t_1)} e^{-\Gamma(t_3 + t_1)}. \quad (3.39)$$

The corresponding third-order polarization in the impulsive limit reads

$$P^{(3)}(t; T, \tau) = S^{(3)}(t, 0, \tau), \quad (3.40)$$

where t is the current time, τ is the coherence time and T is the population time. The latter is considered to be negligible.

Experimentally, the signal is measured by a detector which integrates it with respect to the last time period t :

$$\int_0^\infty dt |P^{(3)}(t; T, \tau)|^2 \propto \frac{\mu_{21}^8}{\hbar^6} e^{-2\Gamma\tau} \cdot \int_0^\infty dt |e^{-i\frac{(\epsilon_2 - \epsilon_1)}{\hbar} t} e^{-\Gamma t}|^2 = \frac{\mu_{21}^8}{\hbar^6} e^{-2\Gamma\tau} \text{const.} \quad (3.41)$$

Homogeneous broadening is accounted for by the dephasing parameter Γ . Inhomogeneous broadening can be taken into account by taking a convolution of Eq. 3.41 with a Gaussian distribution for the energy gap. The inhomogeneously broadened signal is given by¹

$$P^{(3)}(t; T, \tau) \propto \frac{i}{\hbar^3} \mu_{21}^4 e^{-i\frac{\epsilon_{21}^{(0)}}{\hbar} (\tau - t)} e^{-\Gamma(\tau + t)} e^{-\sigma \frac{(\tau - t)^2}{2}}, \quad (3.42)$$

where $\epsilon_{21}^{(0)}$ is the central transition frequency and σ is the width of the inhomogeneous distribution.

THE NON-PERTURBATIVE FORMALISM

The perturbative formalism is the conventional tool for the calculation of spectroscopic signals. The calculation of response functions is easy for simple material systems, such as few-level systems or shifted harmonic oscillators for which the response function $S(t_3, t_2, t_1)$ can be analytically calculated. When dealing with systems of higher complexity, however, the evaluation of the response functions becomes computationally challenging,^{68,77} resulting in long computation times. Hence alternative nonperturbative methods based on a numerically exact treatment of the field-matter interaction have been suggested in the past decades.^{6,8-10,78} In contrast to the perturbative approach, these methods do not require the evaluation of multi-time nonlinear response functions. They are based on computing of the overall polarization. However, an *a posteriori* decomposition of the polarization for specific phase-matching conditions must be carried out. The signals simulated by both perturbative and nonperturbative methods are identical in regimes where both techniques are applicable.

Several nonperturbative methods for the calculation of nonlinear polarizations have been proposed. These include the Equation of Motion Phase-Matching Approach (EOM-PMA)⁷ for the calculation of the 3rd-order polarization in three-pulse four-wave-mixing spectroscopy, the two-pulse EOM-PMA⁶ and the nonperturbative Doorway-

Window Approach.⁸⁻¹² These methods can be computationally more efficient than the perturbative methods. This is important when dealing with systems of high complexity, e.g. systems with strong vibrational and electronic couplings or systems involving dissipative dynamics. Moreover, these methods allow us to explore driven system dynamics beyond the weak-field limit, which in some cases can enhance the information content of the signals. The non-perturbative formalism is a powerful tool for studying molecular excited-state dynamics induced by strong laser fields.

4.1 The Equation of Motion Phase-Matching Approach for Three-Pulse Spectroscopy

The EOM-PMA is a hybrid approach which is valid up to the third order in the system-field interaction.³⁸ This method can be adapted for the evaluation of the polarization for any third-order technique. To explain the EOM-PMA, I consider the three-pulse photon-echo (PE) signal. In this technique, the system interacts with three laser pulses with arrival times t_1, t_2 and t_3 and the phase-matching condition is $k_{PE} = -k_1 + k_2 + k_3$.¹

The evaluation of the PE polarization by the EOM-PMA method is based on the propagation of three auxiliary density matrices $(\sigma_1, \sigma_2, \sigma_3)$ obeying the equations of motion⁷

$$\partial_t \sigma_1(t) = -i[H_0 - V_1(t) - V_2^\dagger(t) - V_3^\dagger(t), \sigma_1(t)] - \mathcal{R}\sigma_1(t) \quad (4.1)$$

$$\partial_t \sigma_2(t) = -i[H_0 - V_1(t) - V_2^\dagger(t), \sigma_2(t)] - \mathcal{R}\sigma_2(t) \quad (4.2)$$

$$\partial_t \sigma_3(t) = -i[H_0 - V_1(t) - V_3^\dagger(t)] - \mathcal{R}\sigma_3(t), \quad (4.3)$$

Here $V_n(t) = \lambda_n E_n(t - t_n) \exp\{i\omega_n t\} X$, $V_n^\dagger(t) \equiv V_n(t)$, $E_n(t - t_n)$ is the dimensionless envelope, X is the transition operator, and λ_n is the scalar product of the transition dipole vector $\vec{\mu}$ with the vector of the external field. Within the RWA, the third-order polarization in the PE direction is evaluated as⁷

$$P_{PE}(t) = e^{ik_{PE} \cdot r} \langle X(\sigma_1(t) - \sigma_2(t) - \sigma_3(t)) \rangle + c.c. \quad (4.4)$$

The polarization, in the RWA, can therefore be evaluated by just performing three density matrices propagations.

After the evaluation of the three-pulse induced polarization, the signal for any 4WM technique can be calculated. For example, the heterodyne detected 2D PE signal is given by a double Fourier transform with respect to two time delays, τ and T ,

$$S_{PE}(\omega_\tau, T, \omega_t) \sim \int d\tau \int dt e^{-i\omega_\tau \tau} e^{i\omega_t t} P_{PE}(\tau, T, t), \quad (4.5)$$

where $\tau = t_2 - t_1$ and $T = t_3 - t_2$.

It should be noticed that the density matrices σ_1, σ_2 and σ_3 in Eq. 4.4 are auxiliary density matrices. In particular, they are not Hermitian. Eq. 4.4 is valid in the leading order of perturbation theory and coincides with the formula obtained by the response function formalism.

4.2 Two-Pulse Based Methods: Ideal and Real Time- and Frequency-Resolved Spectra

The signals for several two-pulse spectroscopic techniques, such as TA PP, SE, or two-pulse PE, can also be computed with nonperturbative methods.⁶ The calculation of the spectra can be performed in a two-step procedure, involving the computation of (1) “ideal” time- and frequency- resolved spectra^{1,6,8,79–81} and (2) subsequent evaluation of “real” spectra by convolution of the ideal spectra with a proper *time- and frequency-gate* function (TFG). This analysis assumes a sufficiently weak CW probe pulse. The pump pulse, on the other hand, can be of arbitrary strength and duration, which can be useful for applications of optimal control theory. Although simultaneous perfect time- and frequency-resolution cannot be obtained in real experiments, ideal spectra are free of this constraint and therefore can provide much more information than real spectra. The TFG functions emulate the effect of the actual probe pulse of finite duration, which reduces the resolution of the spectra.

For the calculation of the ideal spectra within the EOM-PMA, N_ω propagations of several master equations (two for SE and three for PP and PE) at different emission frequencies must be performed. This produces an ideal spectra on the grid $N_t \times N_\omega$ (N_t and N_ω represent the number of grid points for the time and frequency axes, respectively). In contrast to the standard EOM-PMA, this method yields N_t points in the time grid with a single propagation of the density matrix. Therefore the calculation of the ideal time- and frequency-resolved spectra implies N_ω separate propagations. This method is efficient for overlapping (and possibly long) pump and probe pulses⁶.

As an example, I discuss how to calculate the time-and frequency-resolved SE spectrum. Let us consider the system introduced in section 3.3, interacting with a pump pulse giving rise to the interaction matrix element

$$V_L(t) = \lambda_L E_L(t) \exp\{i\omega_L t\} X + H.c.. \quad (4.6)$$

Here λ_L , $E_L(t)$ and ω_L represent the pump pulse strength, dimensionless envelope and carrier frequency, respectively. The calculation of the ideal SE spectrum involves the propagation of the two master equations⁶

$$\partial_t \bar{\rho}(t) = -i[\bar{H} - V_L, \bar{\rho}(t)] - (R + \Gamma)\bar{\rho}(t), \quad (4.7)$$

$$\partial_t \bar{\sigma}_S(t) = -i[\bar{H} - V_L, \bar{\sigma}(t)] - (R + \Gamma)\bar{\sigma}(t) + i\bar{V}_S(t)\bar{\sigma}(t), \quad (4.8)$$

where $\bar{V}_S(t) = \lambda_S \exp\{i\omega_S t\} X$, and λ_S is the probe pulse strength. It should be noted that \bar{V}_S in Eq. 4.8 acts only on the left side of the density matrix $\bar{\sigma}$, therefore no *H.c.* must be considered.

The SE signal corresponds to the steady-state rate of the change of emitted photons with the frequency ω_s at a certain time t . The ideal time- and frequency-resolved SE signal⁸ reads

$$S_{SE}(t, \bar{\omega}_S) = \text{Im} A_{SE}(t, \bar{\omega}_S), \quad (4.9)$$

$$A_{SE}(t, \bar{\omega}_S) = \text{tr}\{\bar{V}_S^\dagger(t)[\bar{\sigma}(t) - \bar{\rho}(t)]\} + O(\lambda_S^3) \quad (4.10)$$

The actual TFG SE spectrum, evaluated for probe pulse of finite duration, is calculated by a two-fold numerical convolution of the ideal spectrum

$$S_{SE}^{\text{TFG}}(t, \bar{\omega}_S) \sim \text{Im} \int_{-\infty}^{\infty} d\bar{\omega} \int_{-\infty}^{\infty} dt' \phi_{SE}(t - t', \bar{\omega}_S - \bar{\omega}') \times A_{SE}(t' - \bar{\omega}'). \quad (4.11)$$

Here,

$$\phi_{SE}(\tau, \Omega) = E_t(-\tau)\phi(\tau, \Omega; \gamma) \quad (4.12)$$

is the TFG function, E_t is the probe pulse envelope and

$$\phi(\tau, \Omega; \gamma) = \int_{-\infty}^{-\tau} d\xi E_t(\xi) \exp\{(\gamma + i\Omega)(\tau + \xi)\}, \quad (4.13)$$

where γ is a parameter which controls the frequency resolution. In the calculation of real spectra by Eq. 4.11 both real and imaginary parts of the ideal spectrum are necessary.

4.3 The Doorway-Window Representation of Nonlinear Response Functions

The Doorway-Window (DW) picture of spectroscopic signals⁸⁻¹² was introduced in 1989 by Mukamel and coworkers⁸². It provides the basis for an alternative method for the numerical calculation of the response of a system to external non-overlapping fields. The application of this formalism has several advantages over the perturbative formalism. For example, it is not restricted to weak system-field interactions and can be employed to study strong-field effects.

The concept of the DW representation can be described as follow. The system of interest (before the interaction with the first pulse) is represented by the density matrix $\rho_0(-\infty)$. At time t_1 , the so-called “*Doorway*” pulse with carrier the frequency ω_1 interacts with the system, and creates a Doorway state $\rho_D(\omega_1)$. Once the pulse is over, the system evolves during time T according to its intrinsic field-free (possibly nonadiabatic and

dissipative) dynamics. At time t_2 , a second “*Window*” pulse with carrier frequency ω_2 interacts with the system, projecting the evolving Doorway state $\rho_D(\omega_1, T)$ into a Window state $\rho_W(\omega_2)$. Any two-pulse signal can thus be evaluated by taking the trace of this projection $\text{Tr}\langle\rho_D(\omega_1, T)\rho_W(\omega_2)\rangle$.

In this thesis, the DW representation is employed for the analysis and evaluation of double-pump signals in the strong field regime. A detailed description of the application of the method is described in chapter 5.

DOUBLE-PUMP FEMTOSECOND FLUORESCENCE SPECTROSCOPY OF SINGLE MOLECULES

The first double-pump SM experiments have been reported in references 24 and 49. In this technique, two phased-locked pulses with relative phase ϕ and time-delay τ interact with a highly-photostable single chromophore in a matrix and the emitted fluorescence photons are collected as a function of τ .

In general, the intensity of the double-pump fluorescence SM signal can be expanded as:

$$I_F(\tau, \phi) = \sum_{k=2,4,6,\dots} I_k(\tau, \phi), \quad (5.1)$$

where k denotes the number of interactions of the chromophore with the laser pulses. For sufficiently weak pulses (equivalent to the perturbative limit) the signal scales linearly with the field intensity and the signal is given by $I_2(\tau, \phi)$. For strong system-field coupling, higher-order terms in the expansion 5.1 gain relevance. Any term in the expansion given by Eq. 5.1 can be dissected into two parts:

$$I_k(\tau, \phi) = I_k + \tilde{I}_k(\tau, \phi). \quad (5.2)$$

Here the first term arises from the interaction of the system with the same pump pulse, and gives rise to a τ - and ϕ -independent background. The second term represents an odd number of interactions of the system with each of the two pulses.

If the pump pulses are well-separated in time, the double-pump signal can be evaluated as⁶²

$$I_k(\tau, \phi) = A(\tau) + (B(\tau)e^{i\phi} + B^*(\tau)e^{-i\phi})e^{-\gamma_2\tau} + (C(\tau)e^{2i\phi} + C^*(\tau)e^{-2i\phi})e^{-\gamma_3\tau}. \quad (5.3)$$

Here γ_2 and γ_3 are the single and double-coherence dephasing rates, $A(\tau)$ represents the contribution which results from the evolution of the chromophore in the electronic population, $B(\tau)$ is the single-coherence contribution, and $C(\tau)$ is the double-coherence contribution. In the weak coupling case, A is τ -independent, contributing to the constant background of the double-pump signal. In the strong coupling case, A is τ -dependent. Explicit analytical expressions for $A(\tau)$, $B(\tau)$ and $C(\tau)$ can be obtained using the strong-pulse doorway-window picture (see section 4.3). $A(\tau)$ and $B(\tau)$ are evaluated by solving the master equation

$$\partial_t \rho(t) = \frac{-i}{\hbar} [H_0 + H_F(t), \rho(t)], \quad (5.4)$$

where H_0 and H_F represent the system and system-field interaction Hamiltonians. The SM signal is given by^{61,62}

$$I_F(\tau, \phi) = \text{Tr}\{\rho_{22}(t \rightarrow \infty)\}, \quad (5.5)$$

where Tr denotes the trace with respect to the vibrational degrees of freedom, and $\rho_{22}(t \rightarrow \infty)$ is the total population of the excited state after the pulses have interacted

with the system. For an electronic two-state system, $A(\tau)$ and $B(\tau)$ can be obtained by the evaluation of Eq. 5.5 for three values of $\phi = 0, \pi/2, \pi$:

$$I_F(\tau, 0) = A(\tau) + B(\tau) + B^*(\tau), \quad (5.6)$$

$$I_F(\tau, \pi) = A(\tau) - (B(\tau) + B^*(\tau)), \quad (5.7)$$

$$I_F(\tau, \pi/2) = A(\tau) + i(B(\tau) - B^*(\tau)). \quad (5.8)$$

Inversion of these equations gives

$$A(\tau) = \frac{I_F(\tau, 0) + I_F(\tau, \pi)}{2}, \quad (5.9)$$

$$\text{Re}B(\tau) = \frac{I_F(\tau, 0) - I_F(\tau, \pi)}{4}, \quad (5.10)$$

$$B(\tau) = \frac{I_F(\tau, 0) + I_F(\tau, \pi)}{4} - \frac{I_F(\tau, \pi/2)}{2}. \quad (5.11)$$

The derivation of Eq. 5.3 for an electronic three-state system is analogous,

Evaluating Eq. 5.5 for $\phi = 0, \pi/4, \pi/2, -\pi/2$, and π , we obtain after elementary algebra:

$$A(\tau) = \frac{I_F(\tau, 0) + I_F(\tau, \pi) + I_F(\tau, \pi/2) + I_F(\tau, -\pi/2)}{4}, \quad (5.12)$$

$$\text{Im}B(\tau) = \frac{I_F(\tau, -\pi/2) - I_F(\tau, \pi/2)}{4}, \quad (5.13)$$

$$\text{Re}C(\tau) = \frac{I_F(\tau, 0) + I_F(\tau, \pi) - I_F(\tau, \pi/2) - I_F(\tau, -\pi/2)}{8}, \quad (5.14)$$

$$\text{Im}C(\tau) = \frac{1}{2} (A(\tau) - I_F(\tau, \pi/4)) + \frac{1}{\sqrt{2}} (\text{Re}B(\tau) - \text{Im}B(\tau)). \quad (5.15)$$

The validity of Eq. 5.3 is based on the following two conditions. The pump pulses must be (i) temporally well separated ($\tau \gg \tau_p$, the pulse-overlap effects can be neglected) and (ii) relatively short ($\tau_p < \gamma_2^{-1}, \gamma_3^{-1}$), so that optical dephasing during the pulses can be neglected. When both conditions are satisfied, the SM signals calculated analytically via Eq. 5.3 match perfectly those obtained via a numerically exact solution of the master equation. If (ii) is slightly violated ($\tau_p \sim \gamma_2^{-1}, \gamma_3^{-1}$), the SM signals calculated by the two methods differ quantitatively, but not qualitatively.

The environment plays a crucial role in shaping spectroscopic signals from single chromophores embedded in a polymer matrix. The effect of the environment at room temperature gives rise to modulations of the molecular parameters. For each time delay of the pulses, the chromophore experiences a different local environment. To model the effects of the environment on the chromophore Hamiltonian parameters (such as excited electronic state energies, vibrational frequencies, potential energy shifts and chromophore-field coupling parameters), I considered a simple stochastic law:

$$A_\tau = \bar{A} + \delta_A(r_\tau - 1/2). \quad (5.16)$$

Here A_τ a stochastic realization of any of the mentioned parameters at a specific time-delay τ , \bar{A} represents its mean value, δ_A controls the amplitude of modulations and r_τ is a random number uniformly distributed in the interval $[0,1]$.

It is potentially possible to uncover information on the environmental modulation of the parameters by analyzing a large number of signals for a single chromophore. For a set of N transient signals measured, $I_F(\tau, \phi, n)$ ($n = 1, 2, \dots, N$), the ensemble signal is given by

$$\bar{I}_k(\tau, \phi) = N^{-1} \sum_n I_F(\tau, \phi, n). \quad (5.17)$$

The variance is given by

$$\Delta I_R(\tau, \phi) = N^{-1} \sum_n I_F(\tau, \phi, n)^2 - \bar{I}_F(\tau, \phi)^2. \quad (5.18)$$

Higher-order moments are defined accordingly. These moments carry information on the stochastic properties of the environmental modulations.

PUBLICATIONS AND MANUSCRIPTS

This chapter contains the most relevant publications produced in this doctoral work. Each of the publications is introduced by a brief conspectus. The papers are attached in the Appendix section.

PAPER 1. Analysis of transient-absorption pump-probe signals of nonadiabatic dissipative systems. E. Palacino-González, M.F. Gelin and W. Domcke. *Manuscript in preparation.*

PAPER 2. Theoretical aspects of femtosecond double-pump single-molecule spectroscopy I. Weak-field regime. E. Palacino-González, M. F. Gelin and W. Domcke. *Phys. Chem. Chem. Phys.* **19**, 32296-32306 (2017).

PAPER 3. Theoretical aspects of femtosecond double-pump single-molecule spectroscopy II. Strong-field regime. E. Palacino-González, M. F. Gelin and W. Domcke. *Phys. Chem. Chem. Phys.* **19**, 32307-32319 (2017).

6.1 Analysis of transient-absorption pump-probe signals of nonadiabatic dissipative systems

Crossings of molecular potential-energy surfaces play a key mechanistic role in energy- and charge-transfer processes.⁸³ Electron transfer constitutes the basic step in a majority of biological processes occurring in nature, such as in the cell metabolism and energy balance in protein complexes. The comprehensive visualization of the ultrafast electronic, vibrational and photochemical dynamics at curve crossings is therefore an important goal of femtosecond time-resolved spectroscopy in chemistry. An explicit mapping of the nonadiabatic wavepacket dynamics calls for the application of complementary time and frequency resolved spectroscopic techniques. In this work, I introduce the concept of ideal and real signals and simulate them for the case of transient-absorption pump-probe (TA PP) spectroscopy. I considered a model of a spectroscopically accessible one-dimensional curve crossing formed by the lowest two excited singlet states in the vicinity of the Franck-Condon region of a polyatomic molecule. The considered reaction mode is coupled to a harmonic bath, which introduces vibrational energy relaxation. The electronic inter-state coupling is assumed to be strong, so that the nonadiabatic electronic population dynamics deviates from the Fermi Golden rule (GR) behaviour, showing electronic and vibrational beatings. The simulations are based on an exact numerical solution of the driven time-dependent master equation. An extension of the two-pulse EOM-PMA method⁶ is considered to account for excited-state absorption (ESA). The effects of laser pulse shape and pulse overlap are implicit in the method. A systematic decomposition of the TA PP signals into its building contributions (*stimulated emission (SE)*, *ground-state bleaching (GSB)* and *excited-state absorption (ESA)*) is performed and the three processes are analyzed in detail. It is shown that a fairly complete and orderly picture of the coupled electronic/nuclear dynamics at avoided crossings in a dissipative environment can be obtained by this manner.

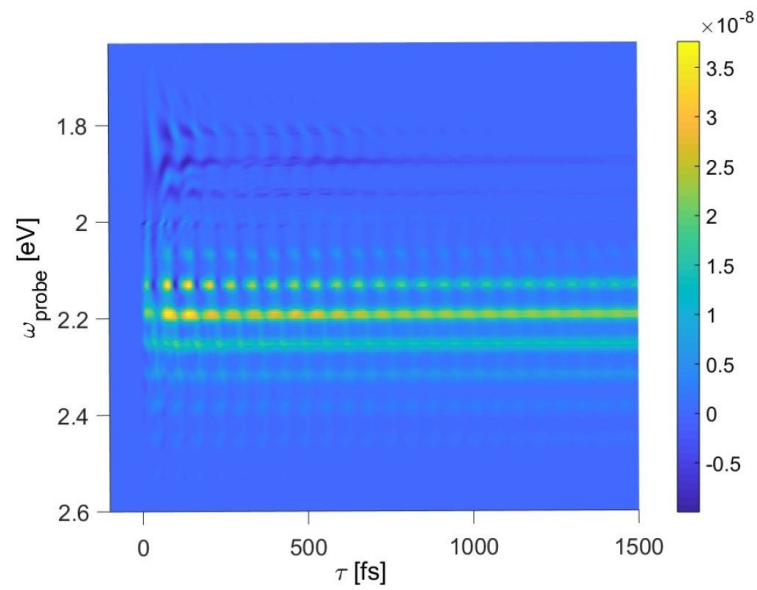


Figure 6.1: Ideal time- and frequency-resolved TA PP signal

Individual candidate contribution: I contributed in extending the method used for the simulation of two-pulse spectroscopy, implemented it in a MATLAB code and analyzed the results. I contributed to writing the paper.

6.2 Theoretical aspects of femtosecond double-pump single-molecule spectroscopy. I. Weak-field regime

I developed a theoretical description of double-pump femtosecond single-molecule signals with fluorescence detection. This work was motivated by recent experiments of the van Hulst group.^{24,49} and considers the description and interpretation of the measured signals in the weak-field regime.⁶¹ A simple model mimicking a chromophore interacting with an environment was used.

The time-resolution of the SM fluorescence signals is provided by the time-delay between two phased-locked femtosecond pulses. The simulation of the signals is performed by solving numerically exactly the driven master equation describing the evolution of the system density-matrix. In the weak-field limit, the signal can be evaluated in the leading (second) order in the system-field interaction:

$$I_F(\tau, \phi) = \bar{I}_2 + \bar{I}_2(\tau, \phi), \quad (6.1)$$

where the subscript “2” indicates the number of interactions of the system with the two pulses, and τ and ϕ denote the time delay and relative phase of the pulses. The first term in Eq. 6.1 represents a constant (time-independent) contribution to the signal, which originates from the interaction with a single pulse. The second term arises from the amplitude in which each pulse interacts once with the system. The different contributions to the signal are shown schematically in Fig. 6.2.

$$I_F(\tau, \phi) = \lambda^2 \left(\begin{array}{c} |1\rangle\langle 1| \\ |0\rangle\langle 0| \end{array} \begin{array}{c} \nearrow \#1 \\ \searrow \#1 \end{array} + \begin{array}{c} |1\rangle\langle 1| \\ |0\rangle\langle 0| \end{array} \begin{array}{c} \nwarrow \#2 \\ \nearrow \#2 \end{array} + \begin{array}{c} |1\rangle\langle 1| \\ |0\rangle\langle 1| \\ |0\rangle\langle 0| \end{array} \begin{array}{c} \nwarrow \#2 \\ \nearrow \#1 \end{array} \right) \tau, \phi$$

Figure 6.2: Schematic view of the different coherent pathways contributing to the double-pump fluorescence signal in the weak-field regime. λ denotes the system-field coupling strength.

In a first approximation I studied how these contributions are reflected in the signal without considering coupling to an environment, which allowed us to establish a reference picture. Then I focused on how slow modulations induced by the environment affect the SM responses.

The signals exhibit vibrational beatings arising from the electronic coherences of the density matrix of the chromophore. These beatings are therefore quenched by electronic dephasing. The signals are sensitive to the relative phase of the pulses. In particular, if the phase is 0 and π , the signals oscillate in anti-phase. I showed that information on the environment-induced fluctuations can be obtained, provided a sufficiently large set of SM signals is available.

Individual candidate contribution: I contributed in developing the methodology for the simulation of the single-molecule signals and implemented it in a MATLAB code. I performed the simulations, analyzed the results and produced the figures. I contributed to writing the paper.

6.3 Theoretical aspects of femtosecond double-pump single-molecule spectroscopy. II. Strong-field regime

As a continuation to the work of Paper 2. I investigated double-pump fluorescence signals in the strong coupling case.⁶¹ I consider a chromophore with three electronic states including a single Franck-Condon active harmonic vibrational mode*. The rest of the vibrational modes of the system are included in an environment, which is described by a dephasing operator introduced phenomenologically. In the strong-field regime, the intensity of the double-pump SM signal can be expanded as

$$I_F(\tau, \phi) = \sum_{k=2,4,6,\dots} I_k(\tau, \phi), \quad (6.2)$$

where k corresponds to the number of interaction with both pulses. Due to the higher order contributions ($k = 4, 6, \dots$), phase-independent population states are produced after an even number of interactions of the system with the first pulse. The SM signal is a combination of coherence and population contributions and contains information on the vibrational wavepacket dynamics in the electronic populations of the chromophore density matrix. The origin of the population dynamics of the SM signals in the strong-field case is illustrated in Fig. 6.3.

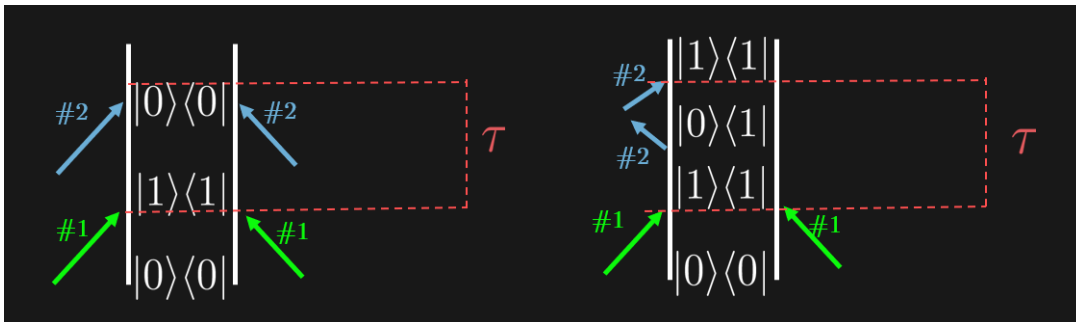


Figure 6.3: Schematic view of the population contribution to the double-pump signal in 4th order. λ denotes the system-field coupling strength.

* Generalization towards chromophores with several Franck-Condon active modes is straightforward.

I determined the critical value of the system-field coupling parameter which represents the turnover from the weak-coupling to the strong-coupling regime. The information content of the signals is higher in the strong-coupling regime, since electronic dephasing does not completely quench the signatures of vibrational dynamics, even though the signal becomes phase-independent. Strong-field signals for relative phases of 0 and π are not mirror images of each other, as in the weak-field case. For pulse delay times longer than the dephasing time, the signals with phases 0 and π coincide and reveal vibrational beatings. The 2D maps (see Fig. 6.4) showing τ and ϕ dependence exhibit a slight tilt of the phase-time profile, which is not as pronounced as in the weak-field case:

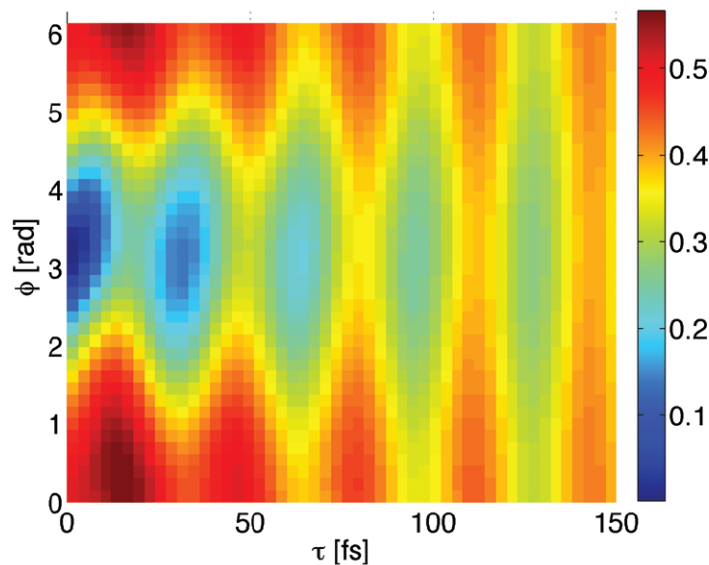


Figure 6.4: A representative 2D map of $I_F(\tau, \phi)$.

I investigated the effect of modulations of the system parameters by the environment and found the critical values of the fluctuations for which the signals lose completely their structure.

It can be concluded that SM signals in the strong-field case are more robust with respect to fluctuations. It has been shown that the effect of higher-lying excited states on the double-pump signals is significant, in particular in the phase dependence of the signals. The analysis demonstrates that the adjustment of the system-field coupling can be

viewed as a tool for the analysis of femtosecond double-pump SM signals and the enhancement of the information in SM spectroscopy.

Individual candidate contribution: I contributed in developing the methodology for the simulation of the single-molecule signals and implemented it in a MATLAB code. I performed the simulations, analyzed the results and produced the figures. I contributed to writing the paper.

CONCLUSIONS

The aim of this dissertation was the development of theoretical methods for the simulation and analysis of nonlinear optical spectra of molecular systems on the femtosecond timescale. The formalism adopted for the computation of the spectra is based on a nonperturbative treatment of the external fields. This approach allows us to study the spectroscopy of more complex systems, such as molecular chromophores in dissipative environments. It is also possible to tune the intensity of the laser pulses to maximize the information content of the spectroscopic signals.

The first part of the thesis focuses on transient-absorption pump-probe (TA PP) spectroscopy. The goal is a comprehensive understanding of the relationship of the nonadiabatic dynamics of a molecular model system in a dissipative environment and the TA PP spectra. For this purpose, I extended the so-called two-pulse equation-of-motion phase-matching approach developed earlier by Gelin *et al.* [*Chem. Phys.* **312**, 135-143 (2005)] towards the inclusion of higher-lying excited electronic states giving rise to excited-state absorption. This method is based on the exact numerical solution of light-driven auxiliary quantum master equations. It accounts for pulse-overlap effects and is applicable for pump pulses of arbitrary strength. A central concept is the so-called ideal TA PP signal. The ideal signal exhibits simultaneously perfect time and frequency

resolution, but is *per se* not experimentally measurable. The measurable real signals are obtained by the convolution of the ideal signals with a time and frequency gate function, which is determined by the shape of the probe pulse. The concept of the ideal signal provides insight into the mechanisms of the detection of ultrafast molecular dynamics with TA PP spectroscopy. Moreover, it is an efficient computational tool for the numerical calculation of TA PP signals.

As an application of these theoretical developments, I considered a model exhibiting an energy crossing of excited states. The model comprises four electronic states, the electronic ground state, two coupled excited electronic states, and a higher excited electronic state. The nuclear motion is represented by a single Condon active vibrational mode. To account for vibrational energy relaxation, the vibrational mode of the model system is coupled to a harmonic bath. Electronic dephasing is included phenomenologically by a decay constant for all electronic coherences. I systematically investigated which features of the photoinduced system dynamics are imprinted in the ideal and real TA PP signals. This analysis demonstrates that TA PP spectroscopy can deliver a fairly complete picture of the nonadiabatic electronic/nuclear dynamics of such systems. The ideal signal is a two-faceted object which combines the features of moving wave packets and stationary spectra. Short (good temporal resolution) or long (good frequency resolution) probe pulses reveal the corresponding facet. It is well known from the response function formalism^{1,5} that the TA PP signal can be decomposed into the ground-state bleach, stimulated emission and excited-state absorption contributions. I developed an extension of the EOM-PMA formalism which allows the computation of the three separate contributions⁸⁴. A systematic analysis of the three contributions was performed for the nonadiabatic dissipative model system.

The second part of this thesis deals with femtosecond time-resolved spectroscopy of single-molecules. Motivated by recent pioneering experiments of van Hulst and coworkers,^{24,49} I developed a theoretical description of double-pump single-molecule

(SM) spectroscopy with fluorescence detection. In this spectroscopic method, two phase-locked pump pulses are applied and the fluorescence signal is recorded as a function of the time delay of the two pump pulses. In contrast to ensemble spectra, SM spectra are free of inhomogeneous broadening. On the other hand, the SM spectra are affected by slow fluctuations of the polymer environment in which the chromophores are embedded. Femtosecond SM spectra contain information on the ultrafast dynamics of the chromophore as well as on the coupling of the chromophore with the polymer environment.

I have developed two variants of theoretical descriptions of femtosecond double-pump SM spectroscopy. The first formulation is based on perturbation theory in the matter-field interaction and is restricted to the weak-field regime and expressions for the spectroscopic signals can be derived analytically. In the second formulation, the matter-field interaction is included nonperturbatively and the density matrix of the chromophore is obtained by the numerical solution of driven master equations.

In the first article,⁶¹ I simulated femtosecond SM signals in the weak-field regime for a model representing a chromophore with a single Condon-active mode. In this regime, the SM spectra are dominated by the coherences of the electronic density matrix of the chromophore, which are rapidly quenched by electronic dephasing, which limits the information content of weak-field SM spectra. In the second article,⁶² I studied SM signals in the strong-field regime, which is characterized by a nonlinear scaling of the signal with the intensity of the pump pulse and the onset of Rabi cycling. In this regime, populations of the electronic density matrix of the chromophore contribute to the SM spectra. The electronic populations are insensitive to electronic dephasing and therefore persist much longer than the electronic coherences. Therefore, femtosecond SM signals in the strong-field regime provide more information on the chromophore dynamics. The simulation of the effect of slow environmental fluctuations on the SM spectra in

the weak-field and strong-field regimes revealed that strong-field SM signals are more robust with respect to environmental effects than weak-field signals.

BIBLIOGRAPHY

- [1] S. Mukamel, *Principles of Nonlinear Optical Spectroscopies*. Oxford University Press (1999).
- [2] A.H. Zewail, *J. Phys. Chem.* **100**, 12701-12724 (1996).
- [3] M. Cho, *Chem. Rev.* **108**, 1331-1418 (2008).
- [4] T. Brixner, J. Stenger, H.M. Vaswani, M. Cho, R.E. Blankenship and G.R. Fleming, *Nature* **434**, 625-628 (2005).
- [5] W. Domcke and G. Stock, *Adv. Chem. Phys.* **100**, 1 (1997).
- [6] M.F. Gelin, D. Egorova and W. Domcke, *Chem. Phys.* **312**, 135-143 (2005).
- [7] M.F. Gelin, D. Egorova and W. Domcke, *Acc. Chem. Res.* **42** (2009).
- [8] M.F. Gelin, D. Egorova and W. Domcke, *Chem. Phys.* **301**, 129 (2004).
- [9] M.F. Gelin, D. Egorova and W. Domcke, *J. Phys. Chem. B* **115**, 5648 (2011).
- [10] M.F. Gelin, D. Egorova, A. V. Pislakov and W. Domcke, *Chem. Phys. Lett.* **391**, 234 (2004).
- [11] Y. J. Yan, L.E. Fried and S. Mukamel, *J. Phys. Chem.*, **93**, 8149-8162 (1989).
- [12] M.F. Gelin and D. Kosov, *Chem. Phys.* **347** (2008).
- [13] W.P. de Boeij, M. S. Pshenichnikov and D. A. Wiersma, *Chem. Phys.* **233**, 287 (1998).
- [14] T. Renger, V. May, and O. Kühn, *Phys. Rep.* **343**, 137 (2001).
- [15] O.A. Sytina, V.I. Novoderezhkin, R. van Grondelle, and M.L. Groot, *J. Phys. Chem. A* **115**, 11944 (2011).

- [16] M.W. Graham, Y.Z. Ma, and G.R. Fleming, *Nano Lett.* **8**, 3936 (2008).
- [17] J.C. Wright, *Annu. Rev. Phys. Chem.* **62**, 209 (2011).
- [18] D.B. Turner and K.A. Nelson, *Nature* **466**, 1089 (2010).
- [19] A.P. Conde, R. Montero, A. Longarte, and F. Castano, *Phys. Chem. Chem. Phys.* **12**, 15501 (2010).
- [20] C. Somma, G. Folpini, K. Reimann, M. Woerner, and T. Elsaesser, *J. Chem. Phys.* **144**, 184202 (2016).
- [21] R.K. Murawski, Y.V. Rostovtsev, Z.E. Sariyanni, V.A. Sautenkov, and M.O. Scully, *Phys. Rev. A* **77**, 023403 (2008)
- [22] P. Nuernberger, T. Vieille, C. Ventalon, and M. Joffre, *J. Phys. Chem. B* **115**, 5554 (2011).
- [23] H. F. Shen, Y. Zhang, T.-M. Yan, Z. Y. Wang, and Y. H. Jiang, *Chem. Phys.* **476**, 17 (2016).
- [24] D. Brinks, R. Hildner, E. M.H.P. van Dijk, F.D. Stefani, J.B. Nieder, J. Hernando, and N.F. van Hulst, *Chem. Soc. Rev.* **43**, 2476 (2014).
- [25] M.F. Gelin, Y. Tanimura and W. Domcke, *J. Chem. Phys.* **139**, 214302 (2013).
- [26] R.D. Coalson, *J. Chem. Phys.* **86**, 995 (1987).
- [27] L. Seidner, G. Stock and W. Domcke, *J. Chem. Phys.* **103**, 3998 (1995).
- [28] C.H. Mark and D. Chandler, *Phys. Rev. A* **44**, 2352 (1991),
- [29] N. Makri and D.E. Makarov, *J. Chem. Phys.* **102**, 4600 (1995).
- [30] N. Makri, *J. Phys. Chem. A* **102**, 4414 (1998).
- [31] Y. Tanimura and R. Kubo, *J. Phys. Soc. Jpn.* **58** 101 (1989).

- [32] Y. Tanimura, *J. Phys. Soc. Jpn.* **75**, 082001 (2006).
- [33] A.G. Redfield, *Adv. Magn. Reson.* **1** (1965).
- [34] W.H. Louisell, in: R.J. Glauber (Ed.), *Proceedings of the International School of Physics - Enrico Fermi*, vol. XLII, New York, Academic Press, p. 680 (1969).
- [35] V. May, O. Kuhn and M. Schreiber, *J. Phys. Chem.* **97**, 12591 (1993).
- [36] U. Weiss, *Quantum Dissipative Systems*. World Scientific, Singapore, 2nd ed. (1999)
- [37] L. Seidner, G. Stock and W. Domcke, *J. Chem. Phys.* **103**, 3998 (1995).
- [38] V. Barone, *Computational Strategies for Spectroscopy. From Small Molecules to Nano Systems*. Wiley, (2012).
- [39] R. Dutta and B. Bagchi, *J. Chem. Phys.* **145**, 164907 (2016).
- [40] R. Kubo, *Adv. Chem. Phys.* **15**, 101 (1969).
- [41] W. Arbelo-González, R. Crespo-Otero, and M. Barbatti, *J. Chem. Theor. Comput.* **12**, 5037-5049, (2016).
- [42] W.E. Moerner and L. Kaldor, *Phys. Rev. Lett.* **62**, 2535-2538 (1989).
- [43] M. Orritt and J. Bernard, *Phys. Rev. Lett.* **65**, 2716-2719 (1990).
- [44] W. E. Moerner and M. Orrit, *Science* **283**, 1670 (1999).
- [45] E. Barkai, Y. Jung and R. Silbey, *Annu. Rev. Phys. Chem.* **55**, 1, (2004).
- [46] W.E. Moerner and T.P. Carter, *Phys. Rev. Lett.* **59**, 2705-2708 (1987).
- [47] G.C. Bjorklund, *Opt. Lett.* **5**, 15-17 (1980).
- [48] W.J. Tango, J.K. Link and R.N. Zare, *J. Chem. Phys.* **49**, 4264-4268 (1968).
- [49] R. Hildner, D. Brinks, F.D. Stefani and N.F. van Hulst, *Phys. Chem. Chem. Phys.* **13**, 1888-1894 (2011).

- [50] A.V. Pislakov, M.F. Gelin and W. Domcke, *J. Phys. Chem. A* **107**, 2657-2666 (2003).
- [51] S.A. Kovalenko, A.L. Dobryakov and V. Farztdinov, *Phys. Rev. Lett.* **96**, 068301 (2006).
- [52] O. Hüter, M. Sala, H. Neumann, S. Zhang, H. Studzinski, D. Egorova and F. Temps, *J. Chem. Phys.* **145**, 014302 (2016).
- [53] S. Rafiq, J.C. Dean and G.D. Scholes *J. Phys. Chem. A* **119**, 11837 (2015).
- [54] S. Rafiq and G.D. Scholes, *Chem. Phys. Lett.* **683**, 500–506 (2017).
- [55] D. Egorova, M.F. Gelin and W. Domcke, *J. Chem. Phys.* **122**, 134504 (2005).
- [56] B. Wolfseder and W. Domcke, *Chem. Phys. Lett.* **259**, 113 (1996).
- [57] D. Egorova, M. Thoss, W. Domcke, and Haobin Wang, *J. Chem. Phys.* **119**, 2761 (2003).
- [58] D. Egorova and W. Domcke, *J. Photochem. Photobiol. A: Chemistry* **166**, 19–31 (2004).
- [59] A.V. Pislakov, M.F. Gelin, and W. Domcke, *J. Phys. Chem. A* **107**, 2657-2666 (2003).
- [60] V. May, O. Kühn, *Charge and Energy Transfer Dynamics in Molecular Systems*. Wiley-VCH, Berlin (2004).
- [61] E. Palacino-González, M.F. Gelin and W. Domcke, *Phys. Chem. Chem. Phys.* **19**, 32296-32306 (2017).
- [62] E. Palacino-González, M.F. Gelin and W. Domcke, *Phys. Chem. Chem. Phys.* **19**, 32307-32319 (2017).
- [63] U. Fano, *Rev. Mod. Phys.* **29**, 74 (1957).
- [64] K. Blum, *Density Matrix Theory and Applications*, Plenum, New York (1981).
- [65] J.M. Jean, R.A. Friesner, and G.R. Fleming, *J. Chem. Phys.* **96**, 5827 (1992).

- [66] D. Egorova, *Modelling of ultrafast electron-transfer processes: multi-level Redfield theory and beyond*. Doctoral dissertation (2002).
- [67] R. Zwanzig, *J. Chem. Phys.* **33**, 1338 (1960).
- [68] W.T. Pollard, A.Y. Felts, and R.A. Friesner, *Adv. Chem. Phys.* **XCIII**, 77 (1996).
- [69] A.J. Leggett, S. Chakravarty, A.T. Dorsey, M.P.A. Fisher, A. Garg and W. Zwerger, *Rev. Mod. Phys.* **59**, 1 (1987).
- [70] W.H. Louisell, *Quantum Statistical Properties of Radiation*. Wiley, New York (1973).
- [71] L. Allen and J.H. Eberly, *Optical Resonance and Two-Level Atoms*. Wiley, New York (1975).
- [72] P. Hamm and M. Zanni, *Concepts and Methods of 2D Infrared Spectroscopy*. Cambridge University Press., (2011).
- [73] W.T. Pollard, S.-Y. Lee and R.A. Mathies, *J. Chem. Phys.* **92**, 4012 (1990).
- [74] J. Rao, M.F. Gelin and W. Domcke *J. Phys. Chem. A* **146**, 084105 (2017).
- [75] M.F. Gelin, W. Domcke and J. Rao, *J. Chem. Phys.* **144**, 184307 (2016).
- [76] J. Rao, M.F. Gelin and W. Domcke *J. Phys. Chem. A* **120**, 3286-329 (2016).
- [77] Y. Tanimura and A. Ishizaki, *Acc.Chem. Res.* **42** (2009).
- [78] H. Wang and M. Thoss, *Chem, Phys.* **347**, 139 (2008).
- [79] S. Mukamel, C. Ciordas-Ciurdariu and V. Khidekel, *Adv. Chem. Phys.* **101**, 345 (1997).
- [80] S. Mukamel, *J. Chem. Phys.* **107**, 4165 (1997).
- [81] M.F. Gelin, A.V. Pislakov and W. Domcke, *Phys. Rev A* **65**, 063507 (2002).
- [82] Y.J. Yan and S. Mukamel, *Phys. Rev. A* **41**, 6485 (1990).

- [83] T. Kumpulainen, B. Lang, A. Rosspeintner and E. Vauthey, *Chem. Rev.* **117**, 10826–10939 (2017).
- [84] E. Palacino-González, M.F. Gelin and W. Domcke, *Manuscript in preparation*.

APPENDIX

Complete list of publications

4. **Analysis of transient-absorption pump-probe signals of nonadiabatic dissipative systems.** E.Palacino-González, M.F. Gelin and W. Domcke. *Manuscript in preparation.*
3. **Nonperturbative response functions: A tool for the interpretation of four-wave-mixing signals beyond third order.** L. Chen, E.Palacino-González, M.F. Gelin and W. Domcke, *J. Chem. Phys.* **147**, 234104 (2017).
2. **Theoretical aspects of femtosecond double-pump single-molecule spectroscopy II. Strong-field regime.** E. Palacino-González, M. F. Gelin and W. Domcke, *Phys. Chem. Chem. Phys.* **19**, 32307-32319 (2017).
1. **Theoretical aspects of femtosecond double-pump single-molecule spectroscopy I. Weak-field regime.** E. Palacino-González, M. F. Gelin and W. Domcke, *Phys. Chem. Chem. Phys.* **19**, 32296-32306 (2017).

Paper 1

*

* **Analysis of transient-absorption pump-probe signals of nonadiabatic dissipative systems.** E.Palacino-González, M.F. Gelin and W. Domcke. *Manuscript in preparation.*

Analysis of transient-absorption pump-probe signals of nonadiabatic dissipative systems

Elisa Palacino-González, Maxim F. Gelin and Wolfgang Domcke¹

Department of Chemistry, Technische Universität München, D-85747, Garching, Germany

(Dated: November 15, 2018)

We introduce and analyze the concept of the "ideal" time and frequency resolved transient-absorption pump-probe (PP) signal. The ideal signal provides the most direct link between the "real" (measurable) PP signal and the material system dynamics. To this end, a method for the simulation of PP signals [Gelin et al., *Chem. Phys.* **312**, 135 (2005)] has been extended to take excited-state absorption into account. The simulation of PP signals involves two steps. (i) The ideal signal, which exhibits perfect time and frequency resolution, is calculated. For this purpose, the actual probe pulse is replaced by an auxiliary continuous-wave pulse. (ii) The real signal is obtained by the convolution of the ideal signal with the appropriate time- and frequency-gate function, which depends on the envelope of the actual probe pulse. This method has been used to simulate integrated and dispersed PP signals for a model system exhibiting nonadiabatic and dissipative dynamics. We demonstrated how the ideal signal, an object exhibiting the features of moving wave packets as well as stationary spectra, is related to real signals detected with short (good temporal resolution) or long (good frequency resolution) probe pulses.

I. INTRODUCTION

Broadly speaking, any time-resolved spectroscopic experiment delivers the response of a material system probed by several laser pulses. The response is detected as a spectroscopic signal, which depends explicitly on the carrier frequencies, delay times, phases, and temporal envelopes of the pulses and contains implicitly useful information about the system dynamics. In transient-absorption pump-probe (for brevity, PP hereafter) experiments, for example, one detects integral (superscript int) signals $I_{PP}^{int}(t, \omega_2)$ or dispersed (superscript dis) signals $I_{PP}^{dis}(t, \omega_2, \omega)$ ¹. Here t is the time delay between the pump and probe pulses, ω_2 is the carrier frequency of the probe pulse, and ω is the frequency corresponding to the Fourier transform of the signal obtained with a spectrometer. In the case of femtosecond third-order spectroscopy, the link between spectroscopic observables, e.g. $I_{PP}^{int}(t, \omega_2)$ and $I_{PP}^{dis}(t, \omega_2, \omega)$, and the material system is given by the third-order response functions^{1,2}. These response functions describe the system dynamics in the electronic ground state and in the relevant excited electronic states during three sequential time intervals, and their behavior is difficult to understand intuitively even in the case of exactly solvable model of damped displaced harmonic oscillator, not to speak about the response functions for more complicated material systems. One can thus raise the question whether it is possible to find a closer link between the measurable signal and the intrinsic system dynamics.

One of such links is provided by the doorway-window approach, which has been introduced and developed for PP signals^{1,3,4} and later extended to photon-echo 2D spectroscopy⁵ and strong-field spectroscopy^{6,7}. This approach offers an intuitively appealing picture of the PP experiment: the pump pulse prepares the material system (that is, creates the doorway state), which then

evolves according to the intrinsic (field free) dynamics and is finally detected by the probe pulse which creates the window state. However, this transparent doorway-window picture is only applicable for non-overlapping laser pulses. Hence it cannot take into account, for example, Raman-like sequences of the pulses (pump-probe-pump) contributing to the PP signal.

An alternative link between signals and material dynamics is given by the concept of the ideal time and frequency resolved spectrum, which has been introduced for the description and interpretation of fluorescence up-converted signals⁸⁻¹⁴. The application of this concept is as follows: (i) One first calculates the ideal spectrum which would be detected if perfect time and frequency resolution were possible. (ii) The real (measured) signal obtained with an up-conversion pulse of finite duration is subsequently evaluated by the convolution of the ideal spectrum with the appropriate time and frequency gate (TFG) function. The ideal spectrum is independent of the properties of the up-conversion pulse. Furthermore, if the excitation pulse is short enough to be approximated by the Dirac delta function, the ideal time- and frequency-resolved fluorescence spectrum is solely determined by the material system dynamics and is independent of the properties of the laser pulses.

The aim of the present work is to introduce and analyze the ideal time- and frequency-resolved spectrum $I_{PP}(t, \omega)$ for femtosecond PP spectroscopy, both as a useful and appealing concept and as an efficient tool to evaluate real (measurable) signals $I_{PP}^{int}(t, \omega_2)$ and $I_{PP}^{dis}(t, \omega_2, \omega)$. We calculate the ideal signal $I_{PP}(t, \omega)$ by employing the two-pulse variant of the equation-of-motion phase-matching approach (EOM-PMA)¹⁴⁻¹⁶. In this approach, the actual probe pulse is replaced by a fictitious continuous wave (CW) pulse, and the ideal signal is obtained by the numerical solution of three auxiliary master equations. In the present work, we

extend the existing EOM-PMA formalism by including higher-lying electronic states which give rise to excited-state absorption (ESA). Motivated by recent transient-absorption PP experiments monitoring ultrafast electron transfer^{17–26}, we consider a model system possessing two non-adiabatically coupled excited electronic states (mimicking donor and acceptor states for electron transfer) which are strongly coupled to a high-frequency reaction mode which, in turn, is bilinearly coupled to a harmonic bath. We analyze the ideal spectrum and demonstrate how the ideal spectrum $I_{PP}(t, \omega)$ is converted into real PP signals $I_{PP}^{int}(t, \omega_2)$ and $I_{PP}^{dis}(t, \omega_2, \omega)$ detected with transform-limited pulses of finite duration.

II. HAMILTONIAN AND EQUATIONS OF MOTION

We consider a chromophore with four electronic states, which are the electronic ground state $|e_0\rangle$, two nonadiabatically coupled excited states $|e_1\rangle$ and $|e_2\rangle$, and a higher excited electronic state $|e_3\rangle$ which accounts for ESA. In the diabatic representation, the Hamiltonian of the chromophore assumes the form

$$H_S = H_g + H_e + H_3 \quad (1)$$

(hereafter, the subscripts g , e , and 3 refer to the electron ground state, two coupled excited states $|e_1\rangle$ and $|e_2\rangle$, and the higher state $|e_3\rangle$, respectively). Explicitly,

$$H_g = |e_0\rangle h_0 \langle e_0|, \quad (2)$$

$$H_e = |e_1\rangle (h_1 + \epsilon_1) \langle e_1| + |e_2\rangle (h_2 + \epsilon_2) \langle e_2| + v (|e_1\rangle \langle e_2| + |e_2\rangle \langle e_1|), \quad (3)$$

$$H_3 = |e_3\rangle (h_3 + \epsilon_3) \langle e_3|. \quad (4)$$

Here ϵ_1 , ϵ_2 and ϵ_3 are the electronic excitation energies (to the energy minima of the excited states) and v denotes the electronic coupling of the states $|e_1\rangle$ and $|e_2\rangle$. The vibrational Hamiltonians are written in the harmonic approximation,

$$h_k = \frac{\omega_{vib}}{2} \{P^2 + (Q - \Delta_k)^2\}, \quad (5)$$

$k = 0, 1, 2, 3$. Here Q and P are the dimensionless coordinate and momentum of the selected vibrational harmonic mode (reaction mode) with frequency ω_{vib} (which, for simplicity, is assumed to be the same in all electronic states). The Δ_k are the horizontal shifts of the potential energy functions with respect to the electronic ground state ($\Delta_0 = 0$).

To account for vibrational relaxation and dephasing in the chromophore due to weakly-coupled intramolecular modes as well as possibly a solvent environment, we

adopt the system-bath approach and partition the total Hamiltonian into the system Hamiltonian, the bath Hamiltonian, and their coupling,

$$H = H_S + H_B + H_{SB}. \quad (6)$$

We assume that the system mode Q is bilinearly coupled to a harmonic heat bath which is responsible for vibrational relaxation and dephasing:

$$H_{SB} = Q \sum_a c_a q_a, \quad (7)$$

$$H_B = \frac{1}{2} \sum_a \omega_a \{p_a^2 + q_a^2\}. \quad (8)$$

Here p_a , q_a and ω_a are the dimensionless momentum, coordinate, and frequency of a th oscillator of the bath. The system-bath coupling constants c_a are taken, for simplicity, the same for all electronic states involved. The influence of the bath on the system dynamics is determined by the spectral density

$$g(\omega) = \sum_a c_a^2 \delta(\omega - \omega_a). \quad (9)$$

Consider a PP experiment, in which the system interacts with pump ($\alpha = 1$) and probe ($\alpha = 2$) laser pulses. The corresponding interaction Hamiltonian in the rotating wave approximation (RWA) is written as

$$H_F(t) = H_1(t) + H_2(t), \quad (10)$$

where

$$H_\alpha(t) = -\eta_\alpha E_\alpha(t - \tau_\alpha) e^{-i(\mathbf{k}_\alpha \mathbf{r} - \omega_\alpha(t - \tau_\alpha))} X + \text{H.c.} \quad (11)$$

η_α is the system-field coupling parameter \mathbf{k}_α , ω_α , τ_α and $E_\alpha(t)$ denote the wave-vector, the carrier frequency, the arrival time, and the dimensionless envelope of the α th pulse. The transition dipole moment operator is defined as

$$X = \eta_\alpha^{02} |e_0\rangle \langle e_2| + \eta_\alpha^{23} |e_2\rangle \langle e_3|. \quad (12)$$

We thus assume that the state $|e_2\rangle$ is optically bright from the electronic ground state $|e_0\rangle$ while the state $|e_1\rangle$ is optically dark. The higher excited state $|e_3\rangle$ is optically coupled to $|e_2\rangle$, but not to $|e_1\rangle$. Darkness of the lowest excited electronic state $|e_1\rangle$ from $|e_0\rangle$ is a common feature in many molecular chromophores, while the assumption of absence of ESA from the state $|e_1\rangle$ is arbitrary and is adopted here for the sake of simplicity. In the following we set, for convenience, $\eta_\alpha^{02} = 1$ and $\eta_\alpha^{23}/\eta_\alpha^{02} = \lambda$.

In the present work, the influence of the vibrational bath is accounted for at the level of multilevel Redfield theory, which is justified when the system-bath interaction is weak and bath memory is short on the system dynamics timescale^{27–29}. The driven system dynamics

is described by the reduced density matrix $\rho(t)$ which obeys the master equation

$$\frac{\partial}{\partial t}\rho(t) = -\frac{i}{\hbar}[H_0 + H_F(t), \rho(t)] + (\mathcal{R} + \mathcal{D})\rho(t). \quad (13)$$

Here \mathcal{R} is the Redfield relaxation operator which accounts for vibrational (vibronic) relaxation and dephasing caused by the system-bath coupling of Eq. (7) (see Refs. ²⁷⁻²⁹ for detailed derivations). The operator

$$\mathcal{D}\rho(t) = -\zeta \sum_{s \neq s'} |s\rangle\langle s'| | \langle s|\rho(t)|s'\rangle \quad (14)$$

describes pure electronic dephasing, where s and s' run over all four electronic states. ζ is a phenomenological dephasing rate which, for simplicity, is taken the same for all electronic states.

Before the arrival of the first laser pulse, the system is assumed to be at thermal equilibrium in the electronic ground state,

$$\rho(-\infty) = \rho_B |e_0\rangle\langle e_0|, \quad (15)$$

where

$$\rho_B = Z_B^{-1} e^{-H_g/(k_B T)} \quad (16)$$

is a vibrational Boltzmann distribution (k_B is the Boltzmann constant, Z_B is the partition function, and T is the temperature).

III. EVALUATION OF PP SIGNALS WITH THE TWO-PULSE EOM-PMA METHOD

For the evaluation of PP signals, we employ the so-called two-pulse EOM-PMA method, which has been derived in Refs. ¹⁴⁻¹⁶ under assumption that ESA can be neglected in the spectral region of interest. In the present work, this method is extended to be able to account for ESA. The detailed derivations of the method for a general system Hamiltonian (A1) and a general transition dipole moment operator (A2) can be found in the Appendix. Here we summarize and adapt the results for the system Hamiltonian (1) and the transition dipole moment operator (12).

A. Evaluation of the ideal signal

To evaluate the ideal PP signal with the two-pulse EOM-PMA method, we have to solve three master equations for the auxiliary density matrices $\rho_1(t)$, $\rho_2(t)$, $\rho_3(t)$:

$$\frac{\partial}{\partial t}\rho_1(t) = -\frac{i}{\hbar}[H_S + \mathcal{H}_1(t) + \mathcal{H}_2(t), \rho_1(t)] + (\mathcal{R} + \mathcal{D})\rho_1(t), \quad (17)$$

$$\frac{\partial}{\partial t}\rho_2(t) = -\frac{i}{\hbar}[H_S + \mathcal{H}_1(t), \rho_2(t)] + (\mathcal{R} + \mathcal{D})\rho_2(t), \quad (18)$$

$$\frac{\partial}{\partial t}\rho_3(t) = -\frac{i}{\hbar}[H_S + \mathcal{H}_2(t), \rho_3(t)] + (\mathcal{R} + \mathcal{D})\rho_3(t). \quad (19)$$

Here

$$\mathcal{H}_1(t) = -\eta_1 E_1(t) e^{i\omega_1 t} X + \text{H.c.} \quad (20)$$

describes interaction of the system with the pump pulse and

$$\mathcal{H}_2(t) = -\eta_2 e^{i\omega t} X \quad (21)$$

describes interaction of the system with a fictitious CW probe pulse. Note that $\mathcal{H}_2(t)$ is non-Hermitian: the H.c. term does is absent in Eq. (21). The auxiliary density matrices in Eqs. (17)-(19) differ in the system-field interactions included: $\rho_1(t)$ is driven by the pump pulse and by the fictitious CW pulse, $\rho_2(t)$ is driven solely by the pump pulse, while $\rho_3(t)$ is driven solely by the CW pulse. Having solved Eqs. (17)-(19), one can calculate the function

$$C_{PP}(t, \omega) = -i \text{Tr} \{ X^\dagger (\rho_1(t) - \rho_2(t) - \rho_3(t)) \} \quad (22)$$

which determines the ideal PP signal

$$I_{PP}(t, \omega) = \text{Re} C_{PP}(t, \omega)$$

(there is a slight change of notation in comparison with Ref.¹⁶).

As is well known, the PP signal can be split into three contributions, ground-state bleach (GSB), stimulated emission (SE), and ESA^{1,2}. In the perturbative response-function formalism, these contributions are obtained separately^{1,2}. To achieve this decomposition within the two-pulse EOM-PMA, two extra steps are necessary.

(i) We introduce the auxiliary left (superscript L) master equation

$$\begin{aligned} \frac{\partial}{\partial t}\rho_1^L(t) = & -\frac{i}{\hbar}[H_S + \mathcal{H}_1(t), \rho_1^L(t)] - \\ & -\frac{i}{\hbar}\mathcal{H}_2(t)\rho_1^L(t) + (\mathcal{R} + \mathcal{D})\rho_1^L(t). \end{aligned} \quad (23)$$

The difference between Eqs. (23) and (17) is as follows: The system-field Hamiltonian $\mathcal{H}_2(t)$ enters Eqs. (17) in the usual manner, through a commutator, while it enters Eq. (23) as an operator acting on the density matrix from the left.

(ii) We define the quantity $\tilde{C}_{PP}(t, \omega)$, which is evaluated via Eq. (22), whereby in the density matrices in Eqs. (17)-(19) are evaluated with $\lambda = 0$ (ESA is neglected).

With these definitions, we have (see Appendix)

$$C_{PP}(t, \omega) = C_{GSB}(t, \omega) + C_{SE}(t, \omega) + C_{ESA}(t, \omega) \quad (24)$$

where

$$C_{SE}(t, \omega) = -i \text{Tr} \{ X^\dagger (\rho_{11}^L(t) - \rho_{10}(t)) \}, \quad (25)$$

$$C_{GSB}(t, \omega) = \tilde{C}_{PP}(t, \omega) - C_{SE}(t, \omega), \quad (26)$$

$$C_{ESA}(t, \omega) = C_{PP}(t, \omega) - \tilde{C}_{PP}(t, \omega). \quad (27)$$

B. Evaluation of the real signal

As is shown in the Appendix, the real integrated and dispersed PP spectra can be calculated by the convolution of the ideal signals with appropriate TFG functions:

$$I_{PP}^{int}(t, \omega_2) = \text{Re} \int_{-\infty}^{\infty} dt' d\omega' \Phi_{PP}^{int}(t - t', \omega_2 - \omega') \times C_{PP}(t', \omega'), \quad (28)$$

$$I_{PP}^{dis}(t, \omega_2, \omega) = \text{Re} \int_{-\infty}^{\infty} dt' d\omega' \Phi_{PP}^{dis}(t - t', \omega_2 - \omega', \omega) \times C_{PP}(t', \omega'). \quad (29)$$

Here the ideal PP signal $C_{PP}(t, \omega)$ is defined by Eq. (24). One can also obtain the GSB, SE, and ESA contributions to the real spectra by replacing $C_{PP}(t, \omega)$ in Eq. (24) by $C_{GSB}(t, \omega)$, $C_{SE}(t, \omega)$ and $C_{ESA}(t, \omega)$, respectively.

The TFG functions depend on the parameters of the probe pulse according to Eqs. (A51) and (A56). Modeling the envelope of the probe pulse as an exponential⁸⁻¹⁴,

$$E_2(t) = \exp(-\Gamma|t|) \quad (30)$$

($1/\Gamma$ being the pulse duration), the TFG functions can be evaluated analytically^{14,16}:

$$\Phi_{PP}^{int}(\tau, \Omega) = \exp(-\Gamma|\tau|) \Phi(\tau, \Omega; \gamma), \quad (31)$$

$$\Phi_{PP}^{dis}(\tau, \Omega, \omega) = \frac{\Gamma}{\Gamma^2 + (\omega - \omega_2)^2} e^{i(\omega - \omega_2)\tau} \Phi(\tau, \Omega; \gamma) \quad (32)$$

where

$$\begin{aligned} \Phi(\tau, \Omega; \gamma) &= \theta(\tau) \frac{\exp\{-\Gamma\tau\}}{\Gamma + \gamma + i\Omega} + \theta(-\tau) \times \\ &\times \left[\frac{\exp\{(\gamma + i\Omega)\tau\}}{\Gamma + \gamma + i\Omega} + \frac{\exp\{(\gamma + i\Omega)\tau\} - \exp\{\Gamma\tau\}}{\Gamma - \gamma - i\Omega} \right] \end{aligned} \quad (33)$$

and $\gamma > 0$ is a technical parameter (see below). In a hypothetical case of simultaneous ideal time and frequency resolution, $\Phi_{PP}^{int}(\tau, \Omega) = \delta(\tau)\delta(\Omega)$, the ideal PP signal coincides with the real integrated PP signal.

C. Ideal vs real signals

Ideal time- and frequency resolved spectra have been discussed in the literature, but mostly in the context of fluorescence up-conversion signals^{8-14,16}. The SE contribution to the PP signal, $\text{Re}C_{SE}(t, \omega)$, coincides (up to a ω -dependent prefactor) with the time- and frequency-resolved fluorescence signal, which is defined as a rate of emission of photons of frequency ω at a time t ¹. The precise simultaneous detection of ω and t violates the Heisenberg uncertainty relation. The actually measured time- and frequency-resolved fluorescence signal is obtained by the convolution of $C_{SE}(t, \omega)$ with the TFG function $\Phi_{PP}^{int}(\tau, \Omega)$ ^{8-14,16}. In this case, the parameter γ in Eq. (33) controls the spectral resolution ($\gamma = 0$ corresponds to ideal frequency resolution), while the duration of the probe pulse controls the time resolution ($E_2(t) \rightarrow \delta(t)$ corresponds to ideal temporal resolution). Eq. (31) reveals that $\Phi_{PP}^{int}(\tau, \Omega)$ cannot be approximated as $\delta(\tau)\delta(\Omega)$, revealing that perfect time and frequency resolution cannot be achieved simultaneously.

The ideal PP spectrum $\text{Re}C_{PP}(t, \omega)$ also has a clear physical meaning: it is the rate of change of energy absorbed by the system from a CW field of a frequency ω and time t . As in the case of fluorescence, simultaneous acquisition of $C_{PP}(t, \omega)$ with high time and frequency resolution is impossible, since the system can interact with the CW pulse (21) at any time moment within the interval $[0, t]$. The real PP signals, detected with a probe pulse of finite duration, are obtained via Eqs. (31) and (32). In contrast to fluorescence up-conversion^{14,16}, $\gamma > 0$ in Eq. (33) is a technical parameter which insures causality (probe follows pump) and convergence (for dispersed signals).

There are certain restrictions on the time and frequency resolution of PP signals. If the probe pulse is short on the timescale of the system dynamics, the time (t) and frequency (ω) resolution of $I_{PP}^{dis}(t, \omega_2, \omega)$ is not restricted by the Heisenberg uncertainty relation, because ω is the frequency corresponding to the Fourier transform with respect to free induction decay time, while t is the time delay between the pump and probe pulse^{1,30}. As for $I_{PP}^{int}(t, \omega_2)$, its resolution with respect to ω_2 is limited by the probe-pulse duration, since the latter defines the detection time of the integrated signal^{1,30}. We also refer to a recent elucidating discussion of the possibility of simultaneous time- and frequency-resolution in femtosecond stimulated Raman scattering (FSRS) spectroscopy^{31,32} (without actinic pulse, FSRS is a variant of PP spectroscopy performed with a picosecond pump-pulse and a femtosecond probe pulse).

D. Computational aspects

Superficially, the main working equation (22) for the calculation of PP signals for a system with ESA coincides with the corresponding formula derived in Ref.¹⁶. How-

ever, the ingredients of this formula, the system Hamiltonian H_S , the dipole moment operator X , and the dissipation operator $\mathcal{R} + \mathcal{D}$ are now defined in an extended Hilbert space comprising the electronic ground state $|e_0\rangle$, two lower-lying excited electronic states $|e_1\rangle$ and $|e_2\rangle$, and the higher-lying excited electronic state $|e_3\rangle$.

The two-pulse EOM-PMA is an efficient method for the evaluation of time- and frequency-resolved PP signals for overlapping pump and probe pulses of arbitrary duration. The pump pulse is allowed to be of any strength, while the probe pulse is assumed to be weak. The calculation of the spectra consists of two steps. (i) One performs N_ω propagations of three density matrices at different emission frequencies according to Eqs. (17)-(19) and calculates the ideal spectrum $C_{PP}(t, \omega)$ on the grid $N_t \times N_\omega$ (N_t and N_ω are the number of grid points in the time and frequency domain, respectively). (ii) The spectrum for the actual probe pulse is calculated by a two-fold numerical convolution of the ideal spectrum with the appropriate TFG functions (31) and (32).

With the two-pulse EOM-PMA method, the signals are calculated without resort to several commonly used simplifications, like the doorway-window approximation^{1,3,4,6,7} or the neglect of dissipation effects during the pulses^{1,33}. The two-pulse EOM-PMA leads to a $\sim N_\omega$ scaling for the computation of time- and frequency-resolved spectra, in contrast to the $\sim N_t \times N_\omega$ scaling for the *a posteriori* decomposition of the total polarization in the nonperturbative approach³⁴ or in the method of Tanimura and Mukamel^{35,36}. The method of Hahn and Stock³⁷ also exhibits a $\sim N_\omega$ scaling, but it is efficient only for temporarily well separated pulses (that is, within the domain of validity of the doorway-window approach).

IV. ILLUSTRATIVE CALCULATIONS

A. Model system and numerical details

The parameters of the model are specified as follows. The vibrational frequency $\omega_{vib} = 0.064$ eV, which yields the vibrational period $\tau_\Omega = 2\pi/\omega_{vib} = 65$ fs. The dimensionless horizontal displacement of the lower excited-state potential energy functions from the minimum of the electronic ground state ($\Delta_g = 0$) are taken as $\Delta_2 = -2$ and $\Delta_1 = -0.83$, the difference of vertical adiabatic electronic energies is set to $\epsilon_2 - \epsilon_1 = 0.126$ eV, and the electronic coupling is $v = 0.01$ eV^{38,39}. As for the higher electronic state, we choose $\Delta_3 = -1$ and $\epsilon_3 = 2\epsilon_2$. This choice is arbitrary, but it ensures a fairly well spectrally separated ESA contribution to the total PP signal (see below). The corresponding potential energy functions are sketched in Fig. 1. It can be seen that the energies of the states $|e_1\rangle$ and $|e_2\rangle$ as a function of Q exhibit a crossing at $Q = -3$.

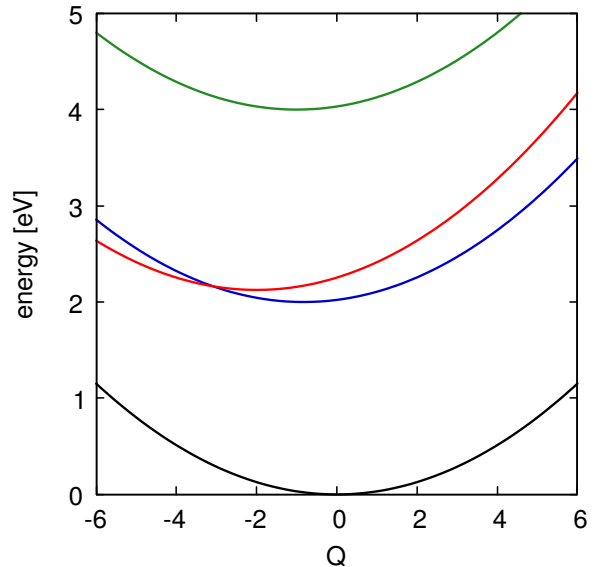


Figure 1. Potential-energy functions of the model system: $|e_0\rangle$ (black), $|e_1\rangle$ (blue), $|e_2\rangle$ (red), $|e_3\rangle$ (green).

In the vicinity of the crossing, the coupling v becomes relevant. While the diabatic energy curves cross, as shown in Fig. 1, the adiabatic energy curves avoid crossing. The near degeneracy of the potential energy functions around $Q = -3$ leads to nonadiabatic effects, since v is smaller than the vibrational frequency ω_{vib} .

The pump pulse is weak ($\eta_1 = 0.001$ eV), its envelope is Gaussian,

$$E_1(t) = \exp\left\{-\left(t/\tau_p\right)^2\right\}, \quad (34)$$

and its duration, $\tau_p = 10$ fs, is short on the timescale of the system dynamics. The carrier frequency of the pump pulse is fixed at $\omega_1 = \epsilon_2 + 2\omega_{vib}$, which corresponds to the vertical excitation energy of the bright state $|e_2\rangle$. We set $\epsilon_2 = 2$ eV. Within the RWA, the value of ϵ_2 just determines the origin of the frequency axis.

The vibrational relaxation operator \mathcal{R} in the master equation (13) is described by multi-level Redfield theory²⁷⁻²⁹ with an Ohmic spectral density, $J(\omega) = \eta\omega \exp\{-\omega/\omega_{vib}\}$. The dimensionless parameter η , which controls vibrational relaxation, is set to 0.1, to ensure underdamped coherent system dynamics. The dependence of \mathcal{R} on the external fields⁴⁰ can be neglected for weak pulses employed in the present work (see discussion in Ref.⁴¹). The electronic dephasing is relatively weak, $\zeta^{-1} = 200$ fs. The temperature is set to zero (at $T = 300$ K, $\omega_{vib}/(k_B T) \approx 2.5$). The driven master equations (17)-(19) and (23) are converted into matrix form by an expansion in terms of the eigenstates of the system Hamiltonian H_S and solved via the fourth-order Runge-Kutta integrator. The ideal signals $C_{PP}(t, \omega)$ and their constituents $C_{GSB}(t, \omega)$, $C_{SE}(t, \omega)$, and $C_{ESA}(t, \omega)$ are

evaluated via Eqs. (24)-(27). The real signals are then calculated via Eqs. (31) and (32) with $\gamma = 0.005$ eV.

B. Discussion of the ideal signals

The three contributions to the ideal PP signal, $C_{GSB}(t, \omega)$ (a), $C_{SE}(t, \omega)$ (b), $C_{ESA}(t, \omega)$ (c), as well as the total ideal signal, $C_{PP}(t, \omega)$ (d) are shown in Fig. 2 as a function of t and ω . We first discuss general features of these signals, and then discuss each of the contributions separately.

As a function of t , the signals rise rapidly ($\sim E_1^2(t)$)⁴² around the arrival time of the pump pulse at $t = 0$. Up to $t \sim \tau_\Omega$ they exhibit the wave-packet motion. The reason is that the CW probe pulse does not have enough time to perform a Fourier analysis of the system dynamics on this time scale. For $t > \tau_\Omega$, the wave-packet signatures disappear, and the signals exhibit series of peaks which reveal predominately the vibrational frequency ω_{vib} (along the ω -axis) and vibrational period τ_Ω (along the t -axis). According to the sign convention adopted in the present work, the GSB and SE contributions to real PP signals are positive, while the ESA contribution is negative. As one can see from Fig. 2, the ideal GSB (a) and SE (b) contributions are predominantly, but not completely, positive and the ideal ESA (c) contribution is only predominantly, but not completely, negative. The reason is that Raman-like sequences of interactions, like pump-probe-pump, contribute to the ideal signal. For the real signal, these contributions are negligibly small for well separated pump and probe pulses. In this case, only sequential interactions, such as pump-pump-probe, contribute to the real signal.

The GSB contribution (Fig. 2(a)) monitors the system dynamics in the electronic ground state. In the impulsive limit (excitation with a Dirac-delta pulse) the wave packet in the ground state is stationary¹. Our pump pulse is not impulsive and therefore several vibrational levels in the electronic ground state are significantly excited, which leads to pronounced stripes around $\omega = 2.13$, 2.19, and 2.25 eV. The time evolution of $C_{GSB}(t, \omega)$ is solely governed by H_g and reveals a purely harmonic wave-packet motion.

The SE contribution (Fig. 2(b)) is identical to the ideal time- and frequency-resolved fluorescence signal which has been studied in detail in Ref.¹⁴. Among numerous vibrational peaks, $C_{SE}(t, \omega)$ exhibits a hump around ~ 500 fs. This hump is an electronic coherence, which is the manifestation of a partial wave-packet revival induced by the non-adiabatic coupling. Along the ω -axis, $C_{SE}(t, \omega)$ narrows with t and eventually almost vanishes at $t = 1500$ fs, due to an irreversible $|e_2\rangle \rightarrow |e_1\rangle$ population transfer, which arises due to the $|e_2\rangle \rightarrow |e_1\rangle$ vibronic coupling and is facilitated by the vibronic energy relaxation due to the coupling of the system to the heat bath. The number of significantly populated vibronic levels in

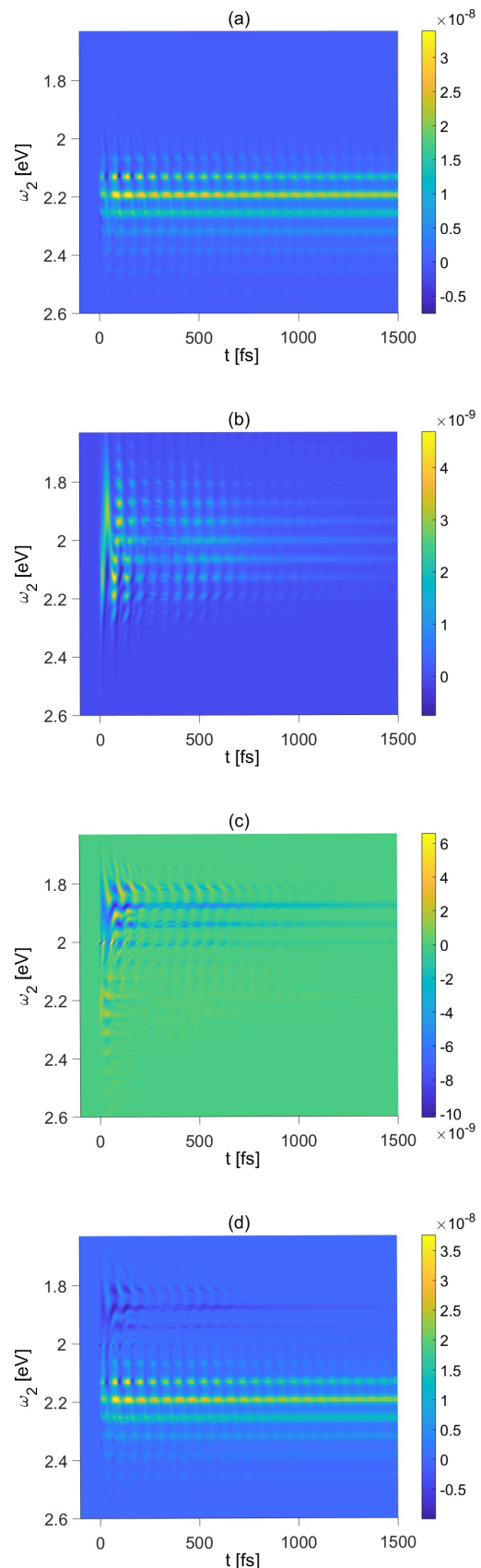


Figure 2. Two-dimensional view of GSB (a), SE (b), ESA (c) contributions to the ideal time- and frequency-resolved PP signal (d).

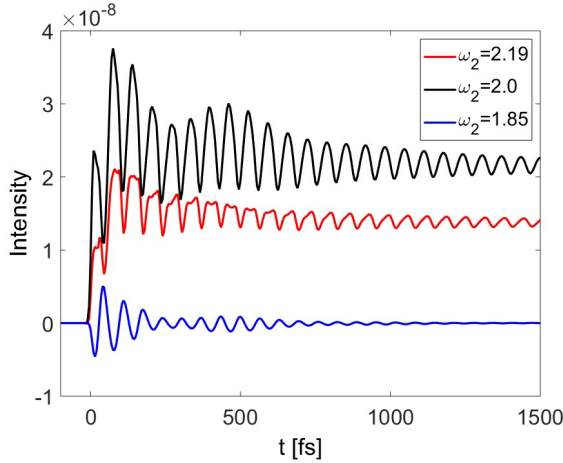


Figure 3. Cuts of the ideal PP signal at three frequencies indicated in the legend.

$|e_2\rangle$ is higher than in the ground state: the wave packet created in $|e_2\rangle$ by the pump pulse follows the gradient towards the equilibrium position of this state, owing to a significant shift Δ_2 of the potential energy function $|e_2\rangle$ relative to $|e_0\rangle$. Hence the SE contribution along the ω -axis is initially wider than the GSB contribution.

The ESA contribution is depicted in Fig. 2(c). The SE and ESA contributions reflect different projections of the wave-packet motion in the coupled $|e_2\rangle$ - $|e_1\rangle$ states. SE projects the wave packet on $|e_0\rangle$, while the ESA projects it in on $|e_3\rangle$. The widths of $C_{ESA}(t, \omega)$ and $C_{SE}(t, \omega)$ along the ω -axis are approximately the same at short t . This reflects the fact that the two contributions originate from the same $|e_2\rangle$ - $|e_1\rangle$ wave packet. At longer t , $C_{ESA}(t, \omega)$ shrinks significantly in comparison with $C_{SE}(t, \omega)$, which mirrors the difference in the reporter states used for the detection of these contributions. In particular, $C_{ESA}(t, \omega)$ exhibits a pronounced minimum around ~ 500 fs (recall that the ESA contribution is predominantly negative) which reveals the electronic coherence.

Fig. 2(d) shows the total ideal PP signal. Note that the GSB, SE, and ESA contributions are concentrated around $\omega = 2.19$, 2.00 , and 1.85 eV, respectively, for the present model. The maximum intensity of the GSB contribution is roughly 7 times higher than the maximum intensity of the SE contribution and 3 times higher than the maximum intensity of the ESA contribution (cf Figs. 2(a)-(c)). As a result, $C_{PP}(t, \omega)$ is dominated at higher ω by $C_{GSB}(t, \omega)$ with admixture of $C_{SE}(t, \omega)$, while it is dominated at lower ω by $C_{ESA}(t, \omega)$. The overall intensity of $C_{PP}(t, \omega)$ decreases with time, since the SE and ESA contributions eventually vanish. PP signals at conical intersections exhibit a similar behavior^{30,47}.

For a more detailed view of the ideal PP signal, Fig. 3 shows cuts of $C_{PP}(t, \omega)$ at $\omega = 2.19$, 2 , and 1.85 eV,

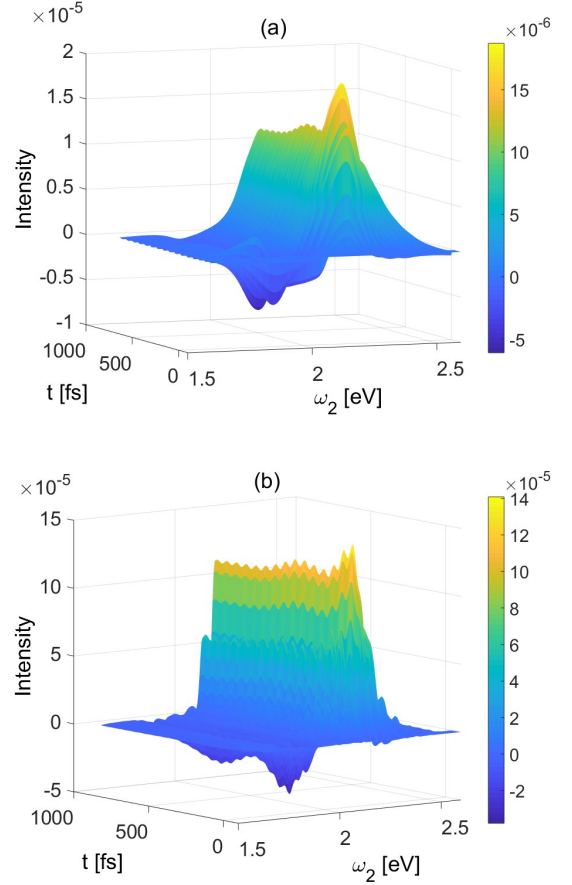


Figure 4. Three-dimensional view of the real integrated time- and frequency-resolved PP signal for short (a, $\Gamma^{-1} = 10$ fs) and relatively long (b, $\Gamma^{-1} = 50$ fs) probe pulse.

corresponding to the maximal intensities of the GSB, SE, and ESA contributions, respectively. For $\omega = 2.19$ eV (red line), $C_{PP}(t, \omega)$ exhibits vibrational oscillations with a period of $\tau_{\Omega} = 65$ fs and reveals vibrational wave-packet motion in the electronic ground state. On the other hand, $C_{PP}(t, \omega)$ at $\omega = 2$ eV (black line, GSB+SE) and at $\omega = 1.85$ eV (blue line, ESA) show, additionally, the electronic revival around 500 fs.

C. Discussion of real signals

Fig. 4 shows integrated PP signals $I_{PP}^{int}(t, \omega_2)$ (Eq. (28)) in the case of a short (a) and a relatively long (b) probe pulse. These signals do not exhibit any signatures of the Raman processes which are present in the ideal signals, since these contributions are averaged out upon the convolution of $C_{PP}(t, \omega)$ with the TFG functions (31) and disappear for non-overlapping pulses. As has been mentioned above, the frequency resolution of the integrated signals as well the width of $I_{PP}^{int}(t, \omega_2)$ in the fre-

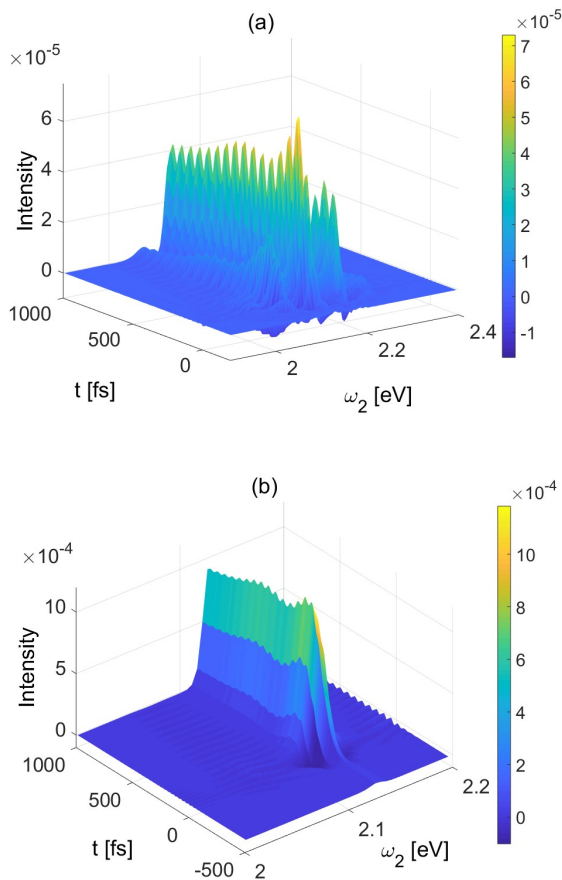


Figure 5. Three-dimensional view of the real dispersed time- and frequency-resolved PP signal for short (a, $\Gamma^{-1} = 10$ fs) and relatively long (b, $\Gamma^{-1} = 50$ fs) probe pulse. Note that (b) is rotated with respect to (a)

quency domain are determined by the pulse duration. Hence the vibrational peaks in $I_{PP}^{int}(t, \omega_2)$ in Fig. 4(a) are not resolved, while the signal in Fig. 4(b) shows clear vibrational features both in the (GSB+SE) and ESA regions. In the time domain, the picture is roughly the opposite, as expected. The signal in Fig. 4(a) reveals vibrational wave-packet motion, while the signal in Fig. 4(b) does not exhibit pronounced temporal dynamics. Yet, since the duration of the probe pulse (50 fs) is close to the vibrational period ($\tau_{\Omega} = 65$ fs), a low-amplitude vibrational beatings superimposed on the “ridges” revealing specific vibrational frequencies are clearly seen in the signal in panel (b). If the duration of the probe pulse is further increased, vibrational beatings disappear and the signal becomes almost static (not shown). The weak electronic recurrence around 500 fs is visible in the signals in both panels.

The intensity of the signals in Fig. 4(a) and (b) decreases with time, since the SE and ESA contributions eventually disappear. However, the total signal does

not tend to zero for $t \rightarrow \infty$, since the GSB contribution does not vanish. By employing the doorway-window picture^{1,3,4,6,7}, it can be shown that the GSB contribution at $t \rightarrow \infty$ yields the window operator averaged with the equilibrium Boltzmann distribution of Eq. (16). If the probe pulse is short on the system dynamics timescale, this quantity is closely related to the linear response function and steady-state linear absorption spectrum.

Fig. 5 shows dispersed signals $I_{PP}^{dis}(t, \omega_2, \omega)$ as a function of t and ω . Panel (a) corresponds to a short probe pulse, while panel (b) corresponds to a relatively long probe pulse. The frequency resolution of both signals is not directly related to the duration of the probe pulse. More precisely, the bandwidth $E_2(\omega - \omega_2)$ of the probe pulse determines, on the one hand, the number of vibrational (vibronic) levels which can be simultaneously probed and, on the other hand, determines the width of $I_{PP}^{dis}(t, \omega_2, \omega)$ in the ω -domain (see Eq. (A52)). For this reason, the width of the signal in panel (a) of Fig. 5 is significantly broader than the width of the signal in panel (b), while both signals are much narrower than the integrated signals in Fig. 4. The ESA is not visible in Fig. 5, since the domain of the ESA contribution, $\omega \sim 1.85$ eV, is not covered by the probe pulse.

Let us now consider the signals in panels (a) and (b) of Fig. 5 separately. If the probe pulse is short (panel (a)), $I_{PP}^{dis}(t, \omega_2, \omega)$ exhibits clear vibrational peaks in the ω -domain as well as vibrational oscillations and an electronic revival in the t -domain. This illustrates that the resolutions in t and ω are not mutually Fourier limited. If the probe pulse is relatively long (panel (b)), $I_{PP}^{dis}(t, \omega_2, \omega)$ does not show any clear peak structure, because the bandwidth of the probe pulse, $\Gamma^{-1} = 0.013$ eV, is too narrow to accommodate a pair of vibrational peaks separated by $\omega_{vib} = 0.064$ eV. In the t -domain, on the other hand, the signal does exhibit low-amplitude oscillations revealing vibrational and electronic features.

Summarizing, both integrated and dispersed PP signals, notably the signals induced by short pump and probe pulses, deliver a fairly complete picture of the coupled electronic/nuclear dynamics of the considered nonadiabatic dissipative system.

V. CONCLUSIONS

We have introduced and analyzed the concept of the ideal time- and frequency-resolved PP signal, $I_{PP}(t, \omega)$. This signal, which can hypothetically be measured as the rate of change of energy absorbed by the system from a CW probe pulse of frequency ω at time t , can be considered as the most direct link between spectroscopic observables and the dynamics of material systems. $I_{PP}(t, \omega)$ is a two-faceted object exhibiting the features of moving wave packets and stationary vibronic spectra. Its projection on short (good temporal resolution) or long (good frequency resolution) probe pulses reveals the cor-

responding facet in the real (measurable) integrated and dispersed PP signals $I_{PP}^{int}(t, \omega_2)$ and $I_{PP}^{dis}(t, \omega_2, \omega)$.

To convert the concept of the ideal PP signal into an efficient numerical tool, we have extended the two-pulse EOM-PMA method of Ref.¹⁶ by the inclusion of ESA. Within this method, the actual probe pulse is replaced by a fictitious CW pulse, and the ideal signal $I_{PP}(t, \omega)$ is obtained by the numerical evaluation of three auxiliary master equations. The real integrated and dispersed PP signals $I_{PP}^{int}(t, \omega_2)$ and $I_{PP}^{dis}(t, \omega_2, \omega)$ are subsequently evaluated by a numerical convolution of $I_{PP}(t, \omega)$ with the appropriate TFG functions. Distinct from other nonperturbative methods^{43,44}, the two-pulse EOM-PMA permits the separate evaluation of the ideal and real GSB, SE, and ESA contributions to the PP signal. The pump pulse can be of arbitrary strength, while the probe pulse is assumed to be weak.

We simulated the ideal and real SE, GSB, and ESA contributions and total PP signals for a model system possessing a Franck-Condon active reaction mode and exhibiting strong electronic inter-state coupling among the excited electronic states. Although the GSB is the dominant contribution (and reveals ground-state wave-packet dynamics), the signatures of the moving wave packets in the coupled excited electronic states are pronounced in the spectral region corresponding to the maximum of SE. The ESA is manifested by negative contributions to the total PP signals. Its time dependence also reveals the wave-packet motion in the coupled electronic states through vibrational oscillations and electronic population recurrence. The ESA contribution is frequently regarded as a nuisance which contaminates PP signals. However, when the ESA is spectrally well separated, the higher excited state serves as a "reporter state", revealing an additional projection of the wave-packet dynamics in the nonadiabatically coupled lower excited electronic states. This may be especially important if one of the coupled states is optically dark from the ground state^{45,46}.

In general, the information delivered by PP signals in the time domain seems to be more instructive than the information delivered in the frequency domain for the considered model system. As a function of time, the signals exhibit oscillatory responses which reveal vibrational wave packets and nonadiabatic electronic dynamics. As a function frequency, (integrated or dispersed) PP spectra exhibit vibrational peaks which are broadened by electronic dephasing.

In the present analysis, we considered a nonadiabatically coupled system with a single Condon-active vibrational mode. While single vibrations sometimes dominate fluorescence of electron transfer systems⁴⁸, several active vibrational modes were clearly detected in recent PP signals for a number of systems^{23,24,45}. Although the explicit treatment of several system modes within multistate Redfield formalism is computationally feasible^{27,49,50}, a more general and more accurate treatment could be achieved by combining the EOM-PMA with the hierarchy equation of motion (HEOM)

method⁵¹, including the laser fields into the system Hamiltonian⁵² and incorporating all optically active vibrational modes into the heat bath via a structured spectral density⁵³. It seems also promising to combine the EOM-PMA with on-the-fly ab initio nonadiabatic quantum or classical molecular dynamics simulations^{54,55}. Work in these directions is in progress.

Appendix A: Two-pulse EOM-PMA with ESA

The derivations in this Appendix generalize those of Ref.¹⁶ toward the inclusion of ESA. In the main article, the chromophore is modeled as a system with four electronic states. Here, we consider the more general situation of a chromophore with an electronic ground state g , a manifold of N_e (possibly coupled) lower-lying excited electronic states denoted collectively by e , and a manifold of N_u higher excited electronic states denoted collectively by u . We neglect possible non-adiabatic couplings between the manifolds g and e , as well as e and u . If necessary, triplet states and singlet-triplet couplings can also be included into H_e . With these simplifications, the system Hamiltonian can be written as a block 3×3 matrix operator in the electronic space

$$H_S = \begin{pmatrix} H_g & 0 & 0 \\ 0 & H_e & 0 \\ 0 & 0 & H_u \end{pmatrix}. \quad (\text{A1})$$

Here H_g is the vibrational Hamiltonian of the electronic ground-state, while the $N_e \times N_e$ matrix operator H_e and the $N_u \times N_u$ matrix operator H_u are the electron-vibrational (vibronic) Hamiltonians in the manifolds e and u including internal vibronic couplings. The system interacts with two laser pulses, and the corresponding system-field Hamiltonian in the RWA is given by Eqs. (10) and (11) in which the transition dipole moment operators are defined as

$$X = \begin{pmatrix} 0 & \mu_{ge} & 0 \\ 0 & 0 & \mu_{eu} \\ 0 & 0 & 0 \end{pmatrix}, \quad X^\dagger = \begin{pmatrix} 0 & 0 & 0 \\ \mu_{eg} & 0 & 0 \\ 0 & \mu_{ue} & 0 \end{pmatrix} \quad (\text{A2})$$

where the $\mu_{eg} = \mu_{ge}^\dagger$ is a $N_e \times 1$ matrix and $\mu_{ue} = \mu_{eu}^\dagger$ is a $N_u \times N_e$ matrix.

The driven system dynamics is described by the electronic density matrix $\rho(t)$ which obeys the master equation (13), in which the system Hamiltonian and the transition dipole moment operators are defined by Eqs. (A1) and (A2), respectively

1. Phase-matched nonlinear polarization

To simplify the subsequent derivations, we found it convenient to subdivide them in a sequence of steps.

a. Evolution under the action of pulse #1

Consider the evolution of the system in the presence of pulse #1 alone,

$$\frac{\partial}{\partial t}\rho(t) = -\frac{i}{\hbar}[H_S + H_1(t), \rho(t)] + (\mathcal{R} + \mathcal{D})\rho(t), \quad (\text{A3})$$

with the initial condition $\rho(t = t') = \rho(t')$. We can rewrite then Eq. (A3) in the operator form,

$$\rho(t) = \mathcal{G}(t, t')\rho(t'). \quad (\text{A4})$$

b. Explicit \mathbf{k}_1 -dependence

Consider the unitary transformed density matrix

$$\sigma(t) = O\rho(t)O^\dagger \quad (\text{A5})$$

where

$$O = \begin{pmatrix} 1 & 0 & 0 \\ 0 & e^{-i\mathbf{k}_1\mathbf{r}} & 0 \\ 0 & 0 & e^{-i2\mathbf{k}_1\mathbf{r}} \end{pmatrix}. \quad (\text{A6})$$

Obviously, $\sigma(t)$ obeys the master equation

$$\frac{\partial}{\partial t}\sigma(t) = -\frac{i}{\hbar}[H_S + \bar{H}_1(t), \sigma(t)] + (\mathcal{R} + \mathcal{D})\sigma(t) \quad (\text{A7})$$

with the initial condition

$$\sigma(t') = O\rho(t')O^\dagger \quad (\text{A8})$$

and with the renormalized system-field Hamiltonian

$$\bar{H}_1(t) = -\eta_1 E_1(t - \tau_1) e^{i\omega_1(t - \tau_1)} X + \text{H.c.} \quad (\text{A9})$$

To obtain Eq. (A7), we used the identities

$$OXO^\dagger = e^{i\mathbf{k}_1\mathbf{r}}X, \quad OX^\dagger O^\dagger = e^{-i\mathbf{k}_1\mathbf{r}}X^\dagger \quad (\text{A10})$$

and assumed that $O(\mathcal{R} + \mathcal{D})O^\dagger = \mathcal{R} + \mathcal{D}$, which is valid if operators $\mathcal{R} + \mathcal{D}$ do no induce any transitions between the manifolds g and e , e and u .

Rewriting Eq. (A7) in operator form as

$$\sigma(t) = \bar{\mathcal{G}}(t, t')\sigma(t') \quad (\text{A11})$$

we obtain

$$\sigma(t) = \bar{\mathcal{G}}(t, t') \{O\rho(t')O^\dagger\}. \quad (\text{A12})$$

The notation $\bar{\mathcal{G}}(t, t') \{...\}$ means that $\bar{\mathcal{G}}$ acts on the entire expression in the curly brackets. Returning back to the original density matrix $\rho(t)$ according to the transformation (A5), we obtain

$$\rho(t) = O^\dagger \bar{\mathcal{G}}(t, t') \{O\rho(t')O^\dagger\} O. \quad (\text{A13})$$

This expression gives, through the operators O , the explicit \mathbf{k}_1 -dependence of the density matrix.

c. Perturbation expansion in pulse #2

Let us now solve Eq. (13) perturbatively in pulse #2. Assuming that there are no external fields at $t = -\infty$, we obtain in the first order

$$\rho(t) = \mathcal{G}(t, -\infty)\rho(-\infty) + i\frac{\eta_2}{\hbar} \int_{-\infty}^t dt' E_2(t' - \tau_2) \times \mathcal{G}(t, t')A(t') + \mathcal{O}(\eta_2^2) \quad (\text{A14})$$

where

$$A(t') = \left(e^{-i(\mathbf{k}_2\mathbf{r} - \omega_2(t' - \tau_2))} X + e^{i(\mathbf{k}_2\mathbf{r} - \omega_2(t' - \tau_2))} X^\dagger \right) \times \mathcal{G}(t', -\infty)\rho(-\infty) - \mathcal{G}(t', -\infty)\rho(-\infty) \times \left(e^{-i(\mathbf{k}_2\mathbf{r} - \omega_2(t' - \tau_2))} X + e^{i(\mathbf{k}_2\mathbf{r} - \omega_2(t' - \tau_2))} X^\dagger \right). \quad (\text{A15})$$

Using the definition (A13), we can rewrite Eq. (A14) as

$$\rho(t) = O^\dagger \bar{\rho}(t) O + i\frac{\eta_2}{\hbar} \int_{-\infty}^t dt' E_2(t' - \tau_2) \times O^\dagger \bar{\mathcal{G}}(t, t') \bar{A}(t') O + \mathcal{O}(\eta_2^2), \quad (\text{A16})$$

where

$$\bar{\rho}(t') \equiv \bar{\mathcal{G}}(t', -\infty)\rho(-\infty) \quad (\text{A17})$$

and

$$\bar{A}(t') = \left(e^{-i(\mathbf{k}_2\mathbf{r} - \mathbf{k}_1\mathbf{r} - \omega_2(t' - \tau_2))} X + e^{i(\mathbf{k}_2\mathbf{r} - \mathbf{k}_1\mathbf{r} - \omega_2(t' - \tau_2))} X^\dagger \right) \bar{\rho}(t') - \bar{\rho}(t') \left(e^{-i(\mathbf{k}_2\mathbf{r} - \mathbf{k}_1\mathbf{r} - \omega_2(t' - \tau_2))} X + e^{i(\mathbf{k}_2\mathbf{r} - \mathbf{k}_1\mathbf{r} - \omega_2(t' - \tau_2))} X^\dagger \right). \quad (\text{A18})$$

d. Evaluation of the polarization

The total nonlinear polarization is defined as

$$P(t) = \text{Tr}\{(X + X^\dagger)\rho(t)\}. \quad (\text{A19})$$

Inserting Eq. (A16) into Eq. (A19) and using Eq. (A10), one obtains:

$$P(t) = e^{i\mathbf{k}_1\mathbf{r}} P_{\mathbf{k}_1}(t) + e^{-i(\mathbf{k}_2\mathbf{r} - 2\mathbf{k}_1\mathbf{r})} P_{-\mathbf{k}_2 + 2\mathbf{k}_1}(t) + e^{i\mathbf{k}_2\mathbf{r}} P_{\mathbf{k}_2}(t) + e^{-i\mathbf{k}_1\mathbf{r}} P_{-\mathbf{k}_1}(t) + e^{i(\mathbf{k}_2\mathbf{r} - 2\mathbf{k}_1\mathbf{r})} P_{\mathbf{k}_2 - 2\mathbf{k}_1}(t) + e^{-i\mathbf{k}_2\mathbf{r}} P_{-\mathbf{k}_2}(t). \quad (\text{A20})$$

Here

$$P_{\mathbf{k}_1}(t) = \text{Tr}\{X\bar{\rho}(t)\}, \quad (\text{A21})$$

$$P_{-\mathbf{k}_2+2\mathbf{k}_1}(t) = i\frac{\eta_2}{\hbar} \int_{-\infty}^t dt' E_2(t' - \tau_2) \times \\ \times \text{Tr} \left\{ X \bar{\mathcal{G}}(t, t') e^{i\omega_2(t' - \tau_2)} [X, \bar{\rho}(t')] \right\}, \quad (\text{A22})$$

$$P_{\mathbf{k}_2}(t) = i\frac{\eta_2}{\hbar} \int_{-\infty}^t dt' E_2(t' - \tau_2) \times \\ \times \text{Tr} \left\{ X \bar{\mathcal{G}}(t, t') e^{-i\omega_2(t' - \tau_2)} [X^\dagger, \bar{\rho}(t')] \right\}, \quad (\text{A23})$$

$$P_{-\mathbf{k}_1}(t) = \text{Tr} \left\{ X^\dagger \bar{\rho}(t) \right\}, \quad (\text{A24})$$

$$P_{\mathbf{k}_2-2\mathbf{k}_1}(t) = i\frac{\eta_2}{\hbar} \int_{-\infty}^t dt' E_2(t' - \tau_2) \times \\ \times \text{Tr} \left\{ X^\dagger \bar{\mathcal{G}}(t, t') e^{-i\omega_2(t' - \tau_2)} [X^\dagger, \bar{\rho}(t')] \right\}, \quad (\text{A25})$$

$$P_{-\mathbf{k}_2}(t) = i\frac{\eta_2}{\hbar} \int_{-\infty}^t dt' E_2(t' - \tau_2) \times \\ \times \text{Tr} \left\{ X^\dagger \bar{\mathcal{G}}(t, t') e^{i\omega_2(t' - \tau_2)} [X, \bar{\rho}(t')] \right\}. \quad (\text{A26})$$

The last three terms in Eq. (A20) are the complex conjugate of the first three terms. Here we are interested in the polarization $P_{-\mathbf{k}_2}(t)$, which gives rise to the PP signal. The term (A25), which yields two-pulse photon echo¹ and double coherence signal⁵⁶, can be considered very similarly.

e. Correlation functions

We define the correlation functions:

$$C(t, t') = \text{Tr} \left\{ X^\dagger \bar{\mathcal{G}}(t, t') [X, \bar{\rho}(t')] \right\}, \quad (\text{A27})$$

$$C^L(t, t') = \text{Tr} \left\{ X^\dagger \bar{\mathcal{G}}(t, t') X \bar{\rho}(t') \right\}, \quad (\text{A28})$$

$$C^R(t, t') = -\text{Tr} \left\{ X^\dagger \bar{\mathcal{G}}(t, t') \bar{\rho}(t') X \right\}. \quad (\text{A29})$$

Evidently,

$$C(t, t') = C^L(t, t') + C^R(t, t'). \quad (\text{A30})$$

The correlation functions introduced above are related with the dressed response functions introduced in Refs.^{57,58}.

We also introduce the object

$$C(t, \omega) = \int_{-\infty}^t dt' e^{-i\omega(t-t')} C(t, t'), \quad (\text{A31})$$

as well as similar objects for the L and R correlation functions. For $t > \tau$,

$$\int_{-\infty}^{\infty} d\omega e^{i\omega(t-\tau)} C(t, \omega) = C(t, \tau). \quad (\text{A32})$$

Hence we can recast Eq. (A26) in the form

$$P_{-\mathbf{k}_2}(t) = i\frac{\eta_2}{\hbar} \int_{-\infty}^t dt' E_2(t' - \tau_2) e^{i\omega_2(t' - \tau_2)} C(t, t') \\ + i\frac{\eta_2}{\hbar} \int_{-\infty}^t dt' \int_{-\infty}^{\infty} d\omega e^{i\omega(t-t')} E_2(t' - \tau_2) e^{i\omega_2(t' - \tau_2)} C(t, \omega). \quad (\text{A33})$$

2. Evaluation of C , C^L and C^R

Solving the master equation (17) for the density matrix $\rho_1(t)$ up to a first order in $\mathcal{H}_2(t)$ and following the procedure outlined in Sec. A 1, we obtain

$$P_1(t) = \text{Tr} \left\{ X^\dagger \rho_1(t) \right\} = \text{Tr} \left\{ X^\dagger \bar{\rho}(t) \right\} + \\ + i\frac{\eta_2}{\hbar} \int_{-\infty}^t dt' e^{i\omega t'} C(t, t') + \mathcal{O}(\eta_2^2) \quad (\text{A34})$$

($\bar{\rho}(t)$ is defined by Eq. (A17)). The application of the same procedure to the auxiliary master equation (A35) for the density matrix $\rho_2(t)$ yields

$$P_2(t) = \text{Tr} \left\{ X^\dagger \rho_2(t) \right\} = \text{Tr} \left\{ X^\dagger \bar{\rho}(t) \right\}. \quad (\text{A35})$$

We thus obtain

$$P_1(t) - P_2(t) = i\frac{\eta_2}{\hbar} C(t, \omega) + \mathcal{O}(\eta_2^2). \quad (\text{A36})$$

Note that $P_1(t)$ contains a contribution where the pump pulse is zero, the so called pump-off contribution¹. To get rid of it, we have to additionally consider the master equation (19) for the density matrix $\rho_3(t)$, which simply gives the linear response to pulse #2,

$$P_3(t) = \text{Tr} \left\{ X^\dagger \rho_3(t) \right\} = i\frac{\eta_2}{\hbar} \int_{-\infty}^t dt' e^{i\omega t'} C_0(t-t') + \mathcal{O}(\eta_2^2). \quad (\text{A37})$$

Here

$$C_0(t-t') = \text{Tr} \left\{ X^\dagger \bar{\mathcal{G}}_0(t-t') [X, \rho(-\infty)] \right\} \quad (\text{A38})$$

where $\bar{\mathcal{G}}_0(t-t') = \bar{\mathcal{G}}(t, t')$ for $\eta_1 = 0$. Hence we obtain

$$P_1(t) - P_2(t) - P_3(t) = i\frac{\eta_2}{\hbar} C_{PP}(t, \omega) + \mathcal{O}(\eta_2^2). \quad (\text{A39})$$

The correlation function

$$C_{PP}(t, \omega) = \int_{-\infty}^t dt' e^{i\omega t'} \{ C(t, t') - C_0(t-t') \} \quad (\text{A40})$$

determines the ideal PP signal.

a. Separate evaluation of the SE, GSB, and ESA contributions

Consider the master equation (23) for the density matrix ρ_1^L . Distinct from Eq. (17), the interaction Hamiltonian $\mathcal{H}_2(t)$ is applied in Eq. (23) on the left only (hence subscript L). Solving it up to a first order in $\mathcal{H}_2(t)$, we obtain

$$P_1^L(t) = \text{Tr} \{X^\dagger \rho_1^L(t)\} = \text{Tr} \{X^\dagger \bar{\rho}(t)\} + i \frac{\eta_2}{\hbar} \int_{-\infty}^t dt' e^{i\omega t'} C^L(t, t') + \mathcal{O}(\eta_2^2). \quad (\text{A41})$$

Then

$$P_1^L(t) - P_2(t) = i \frac{\eta_2}{\hbar} C_{SE}(t, \omega) + \mathcal{O}(\eta_2^2) \quad (\text{A42})$$

where

$$C_{SE}(t, \omega) = \int_{-\infty}^t dt' e^{i\omega t'} C^L(t, t') \quad (\text{A43})$$

specifies the ideal SE signal.

We can also solve the master equation

$$\frac{\partial}{\partial t} \rho_1^R(t) = -\frac{i}{\hbar} [H_0 + \mathcal{H}_1(t), \rho_1^R(t)] + \frac{i}{\hbar} \rho_1^R(t) \mathcal{H}_2(t) + \mathcal{R} \rho_1^R(t) \quad (\text{A44})$$

in which $\mathcal{H}_2(t)$ is applied on the right (hence subscript R). It yields

$$P_1^R(t) = \text{Tr} \{X^\dagger \rho_1^R(t)\} = \text{Tr} \{X^\dagger \bar{\rho}(t)\} + i \frac{\eta_2}{\hbar} \int_{-\infty}^t dt' e^{i\omega t'} C^R(t, t') + \mathcal{O}(\eta_2^2) \quad (\text{A45})$$

Hence the GSB+ESA contribution to the ideal PP signal reads

$$P_1^R(t) - P_2(t) - P_3(t) = i \frac{\eta_2}{\hbar} (C_{GSB}(t, \omega) + C_{ESA}(t, \omega)) + \mathcal{O}(\eta_2^2). \quad (\text{A46})$$

We can further evaluate the GSB and ESA contributions separately, by performing one extra calculation of the PP signal without ESA. This is achieved by putting $\mu_{ue} = 0$ in Eq. (A2).

3. Ideal and real signals

Let us fix the arrival times of the laser pulse #1 and #2 at

$$\tau_1 = 0, \quad \tau_2 = T. \quad (\text{A47})$$

The integrated PP signal is defined as¹

$$I_{PP}^{int}(T, \omega_2) = \text{Im} \int_{-\infty}^{\infty} dt E_2(t - T) e^{-i\omega_2 t} \tilde{P}_{-\mathbf{k}_2}(t),$$

where

$$\tilde{P}_{-\mathbf{k}_2}(t) = P_{-\mathbf{k}_2}(t) - P_{-\mathbf{k}_2}^{off}(t) \quad (\text{A49})$$

and $P_{-\mathbf{k}_2}^{off}(t)$ is the polarization evaluated without the pump pulse. Using Eq. (A33) we obtain

$$I_{PP}^{int}(T, \omega_2) = \text{Re} \int_{-\infty}^{\infty} dt d\omega' \Phi_{PP}^{int}(T - t, \omega_2 - \omega') C_{PP}(t, \omega'). \quad (\text{A50})$$

Here

$$\Phi_{PP}^{int}(\tau, \Omega) = E_2(-\tau) \int_{-\infty}^{-\tau} dt' E_2(t') e^{i(\gamma + i\Omega)(t' + \tau)} \quad (\text{A51})$$

is the integrated TFG function¹⁶.

The dispersed PP signal is defined as¹

$$I_{PP}^{dis}(T, \omega_2, \omega) = \text{Im} E_2(\omega - \omega_2) \tilde{P}_{-\mathbf{k}_2}(\omega) \quad (\text{A52})$$

where

$$E_2(\omega) = \int_{-\infty}^{\infty} dt \exp\{i\omega t\} E_2(t - T), \quad (\text{A53})$$

$$\tilde{P}_{PP}(\omega) = \int_{-\infty}^{\infty} dt \exp\{-i\omega t\} \tilde{P}_{-\mathbf{k}_2}(t). \quad (\text{A54})$$

Using Eq. (A33) we get

$$I_{PP}^{dis}(T, \omega_2, \omega) = \text{Re} \int_{-\infty}^{\infty} dt d\omega' \Phi^{dis}(T - t, \omega_2 - \omega', \omega) C_{PP}(t, \omega'), \quad (\text{A55})$$

where the dispersed TFG function reads¹⁶

$$\Phi_{PP}^{dis}(\tau, \Omega, \omega) = E_2(\omega - \omega_2) e^{i(\omega - \omega_2)\tau} \int_{-\infty}^{-\tau} d\tau' E_2(\tau') e^{(\gamma + i\Omega)(\tau' + \tau)}. \quad (\text{A56})$$

As is easy to see, $\int_{-\infty}^{\infty} d\omega I_{PP}^{dis}(T, \omega_2, \omega) = I_{PP}^{int}(T, \omega_2)$, as it should be¹.

ACKNOWLEDGMENTS

This work has been supported by the Deutsche Forschungsgemeinschaft (DFG) through a research grant and the DFG-Cluster of Excellence "Munich-Centre for Advanced Photonics" (www.munich-photonics.de). E. P.-G. acknowledges support by the International Max-Planck Research School of Advanced Photon Science (www.mpg.de/APS).

REFERENCES

- ¹S. Mukamel, *Principles of Nonlinear Optical Spectroscopy*. Oxford University Press, New York (1995).
- ²L. Valkunas, D. Abramavicius, and T. Mančal. *Molecular Excitation Dynamics and Relaxation* (WILEY-VCH, Weinheim, 2013).
- ³Y. J. Yan, L. E. Fried, and S. Mukamel, *J. Phys. Chem.* **93**, 8149 (1989).
- ⁴L. E. Fried and S. Mukamel, *Phys. Rev. A* **41**, 6485 (1990).
- ⁵M. F. Gelin and W. Domcke, *J. Chem. Phys.* **144**, 194104 (2016).
- ⁶M. F. Gelin, D. Egorova and W. Domcke, *J. Phys. Chem. B* **115**, 5648 (2011).
- ⁷M. F. Gelin, D. Egorova, and W. Domcke, *Phys. Chem. Chem. Phys.* **15**, 8119 (2013).
- ⁸J.H. Eberly and K. Wodkiewicz, *J. Opt. Soc. Am.* **67**, 1253 (1977).
- ⁹S. Mukamel, C. Ciordas-Ciurdariu and V. Khidekel, *IEEE J. Quant. Electr.* **32**, 1278 (1996).
- ¹⁰S. Mukamel, C. Ciordas-Ciurdariu and V. Khidekel, *Adv. Chem. Phys.* **101**, 345 (1997).
- ¹¹S. Mukamel, *J. Chem. Phys.* **107**, 4165 (1997).
- ¹²D. Piolli, D. Brida, S. Mukamel, G. Lanzani, and G. Gerullo, *Phys. Rev. A* **82**, 053809 (2010).
- ¹³M. F. Gelin, A. V. Pislakov, and W. Domcke, *Phys. Rev. A* **65**, 062507 (2002).
- ¹⁴D. Egorova, M.F. Gelin, and W. Domcke, *J. Chem. Phys.* **122**, 134504 (2005).
- ¹⁵M.F. Gelin, D. Egorova and W. Domcke, *Chem. Phys.* **301**, 129 (2004).
- ¹⁶M.F. Gelin, D. Egorova, and W. Domcke, *Chem. Phys.* **312**, 135-143 (2005).
- ¹⁷G. C. Walker, E. Akesson, A. E. Johnson, N. E. Levinger, and P. F. Barbara, *J. Phys. Chem.* **96**, 3728 (1992).
- ¹⁸Y. Zong and J. L. McHale, *J. Chem. Phys.* **106**, 4963 (1997).
- ¹⁹Y. Zong and J. L. McHale, *J. Chem. Phys.* **107**, 2920 (1997).
- ²⁰S. A. Kovalenko, N. Eilers-Koenig, T. A. Senyushkina, and N. P. Ernsting, *J. Phys. Chem. A*, **105**, 4834-4843, (2001).
- ²¹R. Montero, A. P. Conde, A. Longarte, and F. Castano, *Chem. Phys. Chem.* **11**, 3420 (2010).
- ²²T. Backup and M. Motzkus, *Annu. Rev. Phys. Chem.* **65**, 39 (2014).
- ²³S. Rafiq, J. C. Dean and G. D. Scholes, *J. Phys. Chem. A* **119**, 11837 (2015).
- ²⁴S. Rafiq, G. D. Scholes, *Chem. Phys. Lett.* **683**, 500 (2017).
- ²⁵P. Kim, M. S. Kelley, A. Chakraborty, N. L. Wong, R. P. Van Deyne, G. C. Schatz, F. N. Castellano, and L. X. Chen, *J. Phys. Chem. C*, **122**, 14195 (2018).
- ²⁶D. K. Das, K. Makhil, and D. Goswami, *Phys. Chem. Chem. Phys.* **20**, 13400 (2018).
- ²⁷V. May and O. Kühn, *Charge and Energy Transfer Dynamics in Molecular Systems*. Wiley-VCH, Berlin (2004).
- ²⁸D. Egorova, M. Thoss, W. Domcke, and H. Wang, *J. Chem. Phys.* **119**, 2761 (2003).
- ²⁹A.G. Redfield, *Adv. Magn. Reson.* **1**, 1 (1965).
- ³⁰G. Stock and W. Domcke, *Phys. Rev. A* **45**, 3032 (1992).
- ³¹S. Mukamel and J. D. Biggs, *J. Chem. Phys.* **134**, 161101 (2011).
- ³²K. E. Dorfman, B. P. Fingerhut, and S. Mukamel, *Phys. Chem. Chem. Phys.* **15**, 12348 (2013).
- ³³A. V. Pislakov, M. F. Gelin, and W. Domcke, *J. Phys. Chem. A* **107**, 2657-2666 (2003).
- ³⁴L. Seidner, G. Stock and W. Domcke, *J. Chem. Phys.* **103**, 3998 (1995).
- ³⁵Y. Tanimura and S. Mukamel, *J. Phys. Soc. Japan*, **63**, 66 (1994).
- ³⁶Y. Tanimura and Y. Maruyama, *J. Chem. Phys.* **107**, 1779 (1997).
- ³⁷S. Hahn and G. Stock, *Chem. Phys. Lett.* **296**, 137 (1998).
- ³⁸B. Wolfseder, L. Seidner, G. Stock, and W. Domcke, *Chem. Phys.* **217**, 275 (1997).
- ³⁹D. Egorova, A. Kühn, and W. Domcke, *Chem. Phys.* **268**, 105 (2001).
- ⁴⁰T. Renger, V. May, O. Kühn, *Phys. Rep.* **2001**, 343, 137.
- ⁴¹D. Egorova, M. F. Gelin, M. Thoss, H. Wang, and W. Domcke, *J. Chem. Phys.* **129**, 214303 (2008).
- ⁴²M.F. Gelin, D. Egorova, A.V. Pislakov, W. Domcke, *Chem. Phys. Lett.* **391**, 234 (2004).
- ⁴³W. Domcke and G. Stock, *Adv. Chem. Phys.* **100**, 1 (1997).
- ⁴⁴M. F. Gelin, D. Egorova, and W. Domcke, *Acc. Chem. Res.* **42**, 1290 (2009).
- ⁴⁵M. Liebel, C. Schnedermann, and P. Kukura, *PRL* **112**, 198302 (2014).
- ⁴⁶T. Polivka and V. Sundström, *Chem. Phys. Lett.* **477**, 1 (2009).
- ⁴⁷J. Krčmař, M. F. Gelin, and W. Domcke, *J. Chem. Phys.* **143**, 074308 (2015).
- ⁴⁸I.V. Rubtsov and K. Yoshihara, in *Femtochemistry*, edited by DeSchryver *et al.* Wiley, Berlin (2001), pg. 367.
- ⁴⁹A. Kühn and W. Domcke, *J. Chem. Phys.* **116**, 263 (2002).
- ⁵⁰W. W. Parson and A. Warshel, *Chem. Phys.* **296**, 201 (2004).
- ⁵¹Y. Tanimura, *J. Phys. Soc. Jpn.* **75**, 082001 (2006).
- ⁵²M. F. Gelin, Y. Tanimura and W. Domcke, *J. Chem. Phys.* **139**, 214302 (2013).
- ⁵³C. Kreisbeck and T. Kramer, *J. Phys. Chem. Lett.* **3**, 2828-2833 (2012).
- ⁵⁴B. F. E. Curchod and T. J. Martinez, *Chem. Rev.* **118**, 3305 (2018).
- ⁵⁵D. V. Makhov, C. Symonds, S. Fernandez-Alberti, and D. V. Shalashilin, *Chem. Phys.* **493**, 200 (2017).
- ⁵⁶J. Kim, S. Mukamel, G. Scholes, *Acc. Chem. Res.* **42**, 1375 (2009).
- ⁵⁷F. Shuang, C. Yang, and Y. J. Yan, *J. Chem. Phys.* **114**, 3868 (2001).
- ⁵⁸Z. Shen, V. Engel, R. Xu, J. Cheng, and Y. Yan, *J. Chem. Phys.* **117**, 6142 (2002).

Paper 2

†

† **Theoretical aspects of femtosecond double-pump single-molecule spectroscopy I. Weak-field regime.** E. Palacino-González, M. F. Gelin and W. Domcke, *Phys. Chem. Chem. Phys.*, **19**, 32296-32306 (2017). DOI: 10.1039/c7cp04809b



Theoretical aspects of femtosecond double-pump single-molecule spectroscopy. I. Weak-field regime†

Cite this: DOI: 10.1039/c7cp04809b

Elisa Palacino-González,  Maxim F. Gelin* and Wolfgang Domcke

We present a theoretical description of double-pump femtosecond single-molecule signals with fluorescence detection. We simulate these signals in the weak-field regime for a model mimicking a chromophore with a Franck–Condon-active vibrational mode. We establish several signatures of these signals which are characteristic for the weak-field regime. The signatures include the quenching of vibrational beatings by electronic dephasing and a pronounced tilt of the phase-time profiles in the two-dimensional (2D) maps. We study how environment-induced slow modulations of the electronic dephasing and relevant chromophore parameters (electronic energy, orientation, vibrational frequency and relative shift of the potential energy surfaces) affect the signals.

Received 17th July 2017,
Accepted 20th November 2017

DOI: 10.1039/c7cp04809b

rsc.li/pccp

I. Introduction

Single-molecule (SM) spectroscopy comprises a set of techniques which detect spectroscopic signals from individual molecules imbedded in polymer matrices or in solution.^{1–5} Most SM experiments are fluorescence excitation measurements. A tunable narrow-band laser is scanned over the absorption band of a single chromophore, and the absorption is detected as Stokes-shifted fluorescence.⁶ SM signals are free of inhomogeneous broadening inherent in ensemble experiments and are usually recorded in the frequency domain. Because of the nanosecond timescale of fluorescence, time-resolved detection of emitted photons cannot provide information on fast (picosecond) and ultrafast (femtosecond) processes in single chromophores.

SM spectroscopy has been extended into the femtosecond time domain by van Hulst and coworkers.^{7–12} Chromophores were excited with two phase-locked femtosecond laser pulses and the fluorescence was collected with a confocal microscope. In this coherent femtosecond technique, which was pioneered by Scherer and coworkers in ensemble spectroscopy,¹³ the fluorescence is detected as a function of the time delay between the two phase-locked pump pulses. For a pure electronic (two-level) transition in individual terrylenediimide (TDI) molecules in a poly(methyl methacrylate) (PMMA) matrix at ambient temperature, it was shown that electronic quantum coherence can be probed and manipulated.⁹ For individual dinaphthoquaterylenebis(dicarbonyl) (DNQDI) dyes, the detection of vibrational wave packets has been demonstrated.⁷

In the present work, we give a theoretical analysis of femtosecond double-pump SM spectroscopy. Inspired by the experimental results of van Hulst and coworkers,^{7–9} we consider a chromophore with two (ground and excited) electronic states and a single underdamped high-frequency Franck–Condon active vibrational mode. We explore the effects of electronic dephasing, heterogeneity in laser-SM coupling and slow fluctuations of relevant molecular parameters due to the environment.

The femtosecond double-pump SM experiments of ref. 7–9 were performed with relatively weak pump pulses. On the other hand, it is emphasized in the review¹¹ that weak-field and strong-field regimes “are two extremes on a continuum of increasing intensity. Our experiments morph quite naturally from weak-field into strong field depending on the orientation of the molecule in the sample, *i.e.* the overlap between the excitation dipole and the incident electric field. It therefore makes little sense to make a hard statement about the “regime” in which these experiments take place.” From the theoretical perspective, the two regimes can clearly be defined and SM signals simulated in the two regimes exhibit qualitatively different behaviors. In the present paper, we concentrate on the study of SM signals in the regime of weak radiation-matter coupling. The strong-coupling regime is investigated in the accompanying paper.¹⁴

II. Theoretical framework

A. Hamiltonian

Characteristic aspects of SM spectroscopy are the heterogeneity of the ensemble of molecular chromophores as well as temporal fluctuations of molecular parameters, both of which arise from the embedding of the chromophores in a polymer matrix at

Department of Chemistry, Technische Universität München, D-85747, Garching, Germany. E-mail: maxim.gelin@ch.tum.de

† Electronic supplementary information (ESI) available. See DOI: 10.1039/c7cp04809b

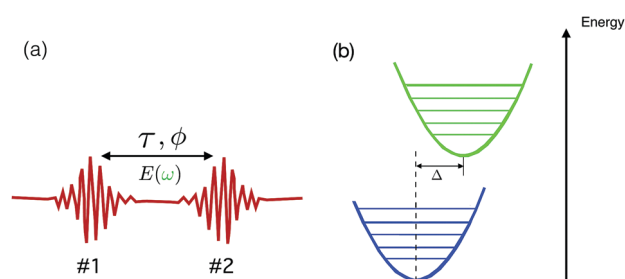


Fig. 1 (a) Sketch of a pair of phase-locked pump pulses. (b) Schematic view of the potential-energy functions of a chromophore with two electronic states.

ambient temperature. In the present context, the thermal fluctuations can be considered as slow, with the exception of the fluctuations of the vertical electronic excitation energy, which lead to pure electronic dephasing.^{1,2,15,16} The electronic dephasing will be included in the quantum equation of motion, while the slow fluctuations of other parameters will be treated as stochastic variables, see below.

In the weak-coupling regime, chromophores resonantly excited by a pair of pump pulses can be considered as electronic two-state systems, because optical transitions between the lowest excited electronic state and higher-lying excited electronic states do not contribute to the SM signal in the leading order in the system-field interaction. We thus consider chromophores with an electronic ground state $|1\rangle$ and a bright excited electronic state $|2\rangle$. The Hamiltonian specifying an individual chromophore is written as a 2×2 matrix in the electronic state space:

$$H = \begin{pmatrix} h_1 & 0 \\ 0 & \varepsilon + h_2 \end{pmatrix}. \quad (1)$$

Here ε is the adiabatic electronic excitation energy, while h_1 and h_2 are the vibrational Hamiltonians in the electronic ground state and the lowest excited electronic state of the chromophore. Note that ε as well as the parameters specifying h_1 and h_2 may differ not only among various chromophores, but also for the same chromophore at different detection times. This temporal heterogeneity will be accounted for below.

The oscillatory transients detected in experiments of ref. 7 and 9 reveal predominantly a single frequency which can be traced to the dominant Franck-Condon-active vibrational mode of the chromophore.¹⁷ We thus explicitly include a single harmonic vibrational mode of the chromophore into the system Hamiltonian of eqn (1). The remaining vibrational modes of the chromophore and the polymer matrix will be considered as a thermal environment and accounted for by an appropriate master equation. Hence

$$\begin{aligned} h_1 &= \frac{\hbar\Omega}{2}(P^2 + Q^2), \\ h_2 &= \frac{\hbar\Omega}{2}(P^2 + (Q - \Delta)^2), \end{aligned} \quad (2)$$

where Ω , P , and Q are the frequency, dimensionless momentum, and dimensionless coordinate of the harmonic mode, respectively,

while Δ is the dimensionless shift of the minimum of the potential energy function of the lowest excited electronic state with respect to the minimum of the ground-state potential-energy function (see Fig. 1). For simplicity, the vibrational frequency is assumed to be the same in both electronic states. If necessary, different frequencies can readily be considered.^{18–22} Generalization of the present description towards chromophores with several separable Franck-Condon-active vibrational modes is straightforward.

The interaction of the chromophore with a pair of phase-locked pulses is described in the dipole approximation and in the rotating wave approximation by the Hamiltonian

$$H_F(t) = -[E(t)X^\dagger + E^*(t)X] \quad (3)$$

where

$$\begin{aligned} E(t) &= E_1(t) + E_2(t), \\ E_1(t) &= E_0 f(t + \tau) e^{-i\omega_1 t}, \\ E_2(t) &= E_0 f(t) e^{i(\phi - \omega_2 t)}, \end{aligned} \quad (4)$$

and

$$X = \hat{e}\boldsymbol{\mu} \begin{pmatrix} 0 & 1 \\ 0 & 0 \end{pmatrix}, \quad X^\dagger = \hat{e}\boldsymbol{\mu} \begin{pmatrix} 0 & 0 \\ 1 & 0 \end{pmatrix}, \quad (5)$$

are the dipole transition operators, $\boldsymbol{\mu}$ is the electronic transition dipole vector, and \hat{e} is the unit vector of the polarization of the two pump pulses. Eqn (4) describes pump pulses with the amplitude E_0 , dimensionless envelope $f(t)$ (which is assumed to be the same for both pulses) and carrier frequencies ω_1 and ω_2 ; τ is the time delay between the pulses and ϕ is their relative phase. For further convenience, we set the arrival time of the first pulse at $t = -\tau$, while the second pulse arrives at $t = 0$. In general, ϕ may depend on both t and τ .^{23,24} In the present work, we assume that ϕ is t - and τ -independent, which seems to be consistent with the definition of phase shifts in the experiments of ref. 7–9. On the other hand, recent variants of femtosecond SM double-pump experiments of van Hulst and coworkers²⁵ and Kukura and coworkers²⁶ employ an interferometric signal detection scheme. These experiments correspond to $\phi = \omega_2\tau$ and can also be simulated with the present theory.

It is convenient to introduce the system-field coupling parameter

$$\eta = \eta_0(\hat{e}\hat{\boldsymbol{\mu}}) \quad (6)$$

where

$$\eta_0 = E_0\mu, \quad (7)$$

$\hat{\boldsymbol{\mu}}$ is a unit vector along the transition dipole moment and $\mu = |\boldsymbol{\mu}|$. η_0 determines the maximal system-field coupling. The actual coupling, $\eta \leq \eta_0$, depends on the orientation of the selected chromophore relative to the polarization of the laser field. Furthermore, all parameters specifying the Hamiltonians (1) and (3),

$$\varepsilon, \Omega, \Delta, \text{ and } \hat{e}\hat{\boldsymbol{\mu}}, \quad (8)$$

may be different for different chromophores and for different measurements, depending on the local environment of the chromophores. For example, the orientation $\hat{e}\hat{\mu}$ of the transition dipole (and therefore the system-field coupling η) may change with time and a SM measurement performed at delay time τ_2 may encounter a $\hat{e}\hat{\mu}$ which differs from $\hat{e}\hat{\mu}$ at delay time τ_1 . Therefore, the SM signal is governed by a “snapshot” Hamiltonian, which changes from measurement to measurement due to the coupling of the chromophore to its local environment. In other words, every SM signal reveals a particular realization of the parameters (8) sampled from certain distributions.

In a typical femtosecond SM double-pump experiment, the signal as a function of the time delay τ is detected with a certain time step $\Delta\tau$,

$$\tau = j\Delta\tau, \quad j = 0, 1, 2, \dots \quad (9)$$

In ref. 7–9, for example, $\Delta\tau = 3$ fs. Furthermore, the signal is measured several times for every time delay and is averaged.¹¹ This permits the detection of a sufficient number of photons and improves the signal-to-noise ratio. The time interval between all these measurements (those performed for a fixed τ and determined by the repetition rate of the SM experiment as well as those performed for different τ) is much longer than any relevant microscopic time interval specifying electron-vibrational dynamics and fluorescence detection of the single chromophore. Hence, there is no correlation between the values of the parameters (8) in any two consecutive measurements.

To simulate such a measurement protocol, we introduce a stochastic modulation of the chromophore parameters. For simplicity and universality, we adopt a coarse grained picture. Rather than explicitly simulating multiple measurements performed at every fixed time delay $j\Delta\tau$, we represent these multiple measurements by an effective single measurement and assume that at every time delay $j\Delta\tau$ the parameters (8) can take random values. Specifically, we assume the following simple modulation law:

$$A_\tau = \bar{A} + \delta_A(r_\tau - 1/2). \quad (10)$$

Here A_τ is a stochastic realization of any parameter from the list (8) at a specific time delay τ , \bar{A} represents its mean value, δ_A controls the amplitude of modulations, and r_τ is a random number uniformly distributed in the interval $[0,1]$. Thus, realizations of the parameters are modeled as uncorrelated stochastic variables.

Obviously, the modulation law of eqn (10) is not unique. Other modulation laws, *e.g.*, Gaussian, are more common and may be better justified physically. However, the distributions of the parameters extracted from the experiments of ref. 7–9 are difficult to associate with specific standard distributions. The choice of the stochastic modulation law is further discussed in Section IV.

B. Reduced density matrix, equation of motion, and SM signal

Each particular realization of the parameters (8) produces a snapshot system Hamiltonian H and a snapshot system-field interaction Hamiltonian $H(t)$ for a given time delay τ . The chromophore is also coupled to the environment, which

includes the vibrational modes of the chromophore that are not explicitly included in the system Hamiltonian H as well as the degrees of freedom of the polymer matrix. Integrating out the environmental degrees of freedom, the time evolution of the chromophore is described by the reduced density matrix

$$\rho(t) = \begin{pmatrix} \rho_{11}(t) & \rho_{12}(t) \\ \rho_{21}(t) & \rho_{22}(t) \end{pmatrix}. \quad (11)$$

The time evolution of $\rho(t)$ is governed by the snapshot master equation

$$\frac{\partial \rho(t)}{\partial t} = -\frac{i}{\hbar}[H + H_F(t), \rho(t)] + \Gamma\rho(t), \quad (12)$$

where the snapshot relaxation operator Γ accounts for the impact of the environment on the dynamics of the system. The observable associated with an operator S of the system is evaluated for $t \geq 0$ through the reduced density matrix as

$$S(t) = \text{Tr}\{\rho(t)S\} \quad (13)$$

where the trace is taken with respect to electronic and vibrational degrees of freedom of the system. $S(t)$ depends on the time delay τ of the pump pulses both explicitly (owing to $H(t)$) and parametrically (owing to random realizations of the chromophore parameters according to eqn (10)).

The double-pump SM signal is defined as the total (time- and frequency-integrated) fluorescence of a single chromophore detected as a function of the interpulse delay τ and relative phase ϕ . This signal is proportional to the time integral of the population of the excited electronic state of the chromophore ($S = |2\rangle\langle 2|$) and can be evaluated as

$$I_F(\tau, \phi) \sim \int_{t_0}^{\infty} dt \text{Tr}\{\rho_{22}(t)\}, \quad (14)$$

where t_0 is any time moment before the arrival of the first pump pulse such that $\text{Tr}\{\rho_{22}(t_0)\} = 0$.

As emphasized in the beginning of Section IIA, electronic dephasing is the fastest and the most important environmental effect at ambient temperature. It is caused by the modulation of the electronic excitation energy of the chromophore by intramolecular and intermolecular degrees of freedom or by phase drifts of the laser pulses employed. It can be accounted for by the dephasing operator

$$\Gamma\rho(t) = -\gamma \begin{pmatrix} 0 & \rho_{12}(t) \\ \rho_{21}(t) & 0 \end{pmatrix} \quad (15)$$

where γ is the snapshot electronic dephasing rate which obeys the modulation law (10). A microscopic treatment of electronic dephasing is also possible (see, *e.g.*, ref. 27), but the phenomenological description *via* eqn (15) is sufficient for the purposes of the present work. Usually, dephasing is considered to be an ensemble property and the concept of dephasing should be used at the SM level with caution. An elucidative discussion of this topic can be found in ref. 9 and 28. As discussed above, the signals of ref. 7–9 were measured many times for a fixed interpulse delay τ . The application of ergodic arguments indicates that

these signals (and therefore electronic dephasing) have a partial ensemble character.

There exist several inter- and intra-molecular processes affecting excited-state populations of individual chromophores which are not described by the operator (15). They include radiationless decay (intersystem crossing, internal conversion), orientational relaxation, as well as vibrational relaxation and dephasing. These processes, occurring on the picosecond-to-nanosecond time scale, can be disregarded on the timescale of a few hundred femtoseconds, which is determined by the time delay between the two pump pulses. However, the timescale of these processes is comparable with the timescale of the detection of SM fluorescence (spontaneous emission).

Radiationless decay of the excited electronic state can be taken into account by introducing the corresponding decay time τ_R and setting $\Gamma_R \rho(t) = -\tau_R^{-1} \rho_{22}(t)$. Since Γ_R causes exponential decay of the population of the excited electronic state, radiationless decay can be simply disregarded by defining the SM signal as

$$I_F(\tau, \phi) \sim \text{Tr}\{\rho_{22}(t_f)\} \quad (16)$$

where t_f is a time moment at which the second pump pulse is over. Eqn (14) and (16) are equivalent definitions of the same SM signal, which is independent of the fluorescence accumulation time. In the present work, we do not consider radiationless decay explicitly and identify the signal $I_F(\tau, \phi)$ with the r.h.s. of eqn (16). This renders the signal dimensionless and $0 \leq I_F(\tau, \phi) \leq 1$.

Fluorescence lifetimes can be comparable with characteristic rotational diffusion times. However, the impact of rotational diffusion on the SM signal is similar to that of radiationless decay and can be treated in the same manner, replacing τ_R by the rotational diffusion time τ_D . Hence, reorientation of the chromophore during a single measurement is not explicitly considered in the present work. A rigorous theory describing the impact of rotational diffusion as well as finiteness of the numerical aperture on the excitation and collection of fluorescence from individual chromophores can be found in ref. 29.

For a chromophore imbedded in a polymer matrix, the environment is a source of vibrational relaxation and vibrational dephasing. At the SM level, these processes can be accounted for by invoking quantum stochastic equations³⁰ or stochastic Schrödinger equations.³¹ For polyatomic chromophores, vibrational relaxation and vibrational dephasing typically occur on a picosecond timescale. For $t > t_f$, however, vibrational relaxation and vibrational dephasing do not affect the total electronic population $\text{Tr}\{\rho_{22}(t)\}$: these processes just redistribute energy among vibrational levels within the excited electronic state. Vibrational relaxation and vibrational dephasing are therefore irrelevant for the evaluation of femtosecond double-pump SM signals.

Summarizing, the master eqn (12) with the relaxation operator (15) is appropriate for the simulation of femtosecond double-pump SM signals defined *via* eqn (16). Master equations describing steady-state SM signals, on the other hand, are constructed according to different criteria. These master equations can be formulated for vibronic populations only (assuming fast

vibrational dephasing) and account for various dissipation processes and lifetimes.³²

C. Analytical results

According to eqn (3), interaction of the chromophore with the external field is governed by the dipole coupling parameter η of eqn (6). The SM signal can be expanded in a power series in η ²⁷

$$I_F(\tau, \phi) = \sum_{k=2,4,6,\dots} I_k(\tau, \phi). \quad (17)$$

Here $I_k(\tau, \phi) \sim \eta^{2k}$, where k corresponds to the number of interactions of the chromophore with the pump pulses. For sufficiently weak pulses, the SM signal is given by the lowest-order contribution $I_2(\tau, \phi)$. In this case, the chromophore interacts twice with the pump pulses and the signal scales linearly with the pulse intensity. This is the weak-coupling regime which is the subject of the present paper. For stronger pump pulses, higher-order terms in the expansion (17) are relevant, and the signal depends nonlinearly on the pulse intensity (see the accompanying paper¹⁴).

The weak-field signal can be evaluated as:³³

$$I_2(\tau, \phi) = \sum_{a,b=1}^2 \sigma_{ab}(\tau, \phi) \quad (18)$$

where

$$\sigma_{ab}(\tau, \phi) = 2\text{Re} \int_{-\infty}^{\infty} dt \int_0^{\infty} dt_1 E_a^*(t) E_b(t - t_1) R(t_1) \quad (19)$$

and $R(t_1)$ is the linear response function which describes steady-state linear absorption and relaxed fluorescence. For the model system of the present work, $R(t_1)$ can be evaluated analytically as explained in ref. 16. In our notation, the result reads:

$$R(t_1) = \eta^2 e^{-i(\epsilon/\hbar + \gamma)t_1 - g(t_1)}, \quad (20)$$

where

$$g(t_1) = \frac{\Delta^2}{2} \left[\coth\left(\frac{\hbar\Omega}{2k_B T}\right) (1 - \cos(\Omega t_1)) + i \sin(\Omega t_1) \right], \quad (21)$$

k_B is the Boltzmann constant and T is temperature.³⁴

If the pulses have Gaussian envelopes

$$f(t) = \exp\{-(t/\tau_p)^2\} \quad (22)$$

(τ_p being the pulse duration) the integration over t in eqn (19) can be done analytically with the result³³

$$I_2(\tau, \phi) \sim \text{Re} \int_0^{\infty} dt_1 [\Phi_0(t_1) + \Phi_1(t_1, \tau, \phi)] R(t_1). \quad (23)$$

Here

$$\Phi_0(t_1) = e^{-t_1^2/(2\tau_p^2)} (e^{i\omega_1 t_1} + e^{i\omega_2 t_1}) \quad (24)$$

is the contribution describing interaction of the chromophore with the same pump pulse (pulse #1 or #2), while

$$\Phi_1(t_1, \tau, \phi) = e^{-\omega^2 \tau_p^2/2} e^{i\omega_1 t_1} (e^{-(\tau-t_1)^2/(2\tau_p^2)} e^{-i(\phi-\omega\tau)} + e^{-(\tau+t_1)^2/(2\tau_p^2)} e^{i(\phi-\omega\tau)}) \quad (25)$$

is the contribution arising when the chromophore interacts once with pulse #1 and once with pulse #2. In the above expressions

$$\omega_{12} = (\omega_1 + \omega_2)/2, \quad \omega = (\omega_2 - \omega_1)/2. \quad (26)$$

The term (24) yields the τ -independent background, which is inherent in double-pump signals.^{7–9} The term (25) determines the τ -dependence of the signal. If the pulses are short on the vibrational dynamics time scale, have the same carrier frequencies and are temporally well separated, eqn (23) simplifies to

$$I_2(\tau, \phi) \sim \eta^2 [2 + \text{Re} e^{-i\phi - (i\varepsilon/\hbar - \omega_1 + \nu)\tau - g(\tau)}]. \quad (27)$$

The above analysis reveals that double-pump SM spectroscopy in the weak-field regime does not monitor vibrational wavepackets which are associated with electronic populations of the system density matrix. Double-pump spectroscopy rather monitors the effect of vibrational motion on the electronic coherence of the density matrix.

D. Computational details

The mean values of the model parameters (8) are designated by an overbar and are selected as follows. The vibrational frequency is set to $\bar{\Omega} = 0.13$ eV, which yields a vibrational period $\tau_\Omega = 2\pi/\bar{\Omega} = 32$ fs. These values are typical for the SM signals of ref. 7 and 8. For such a high-frequency vibration, $\coth[\hbar\bar{\Omega}/(2k_B T)] \approx 1$ at ambient temperature. Hence the chromophore is initially in its ground vibrational state in the electronic ground state. The dimensionless shift of the excited-state potential energy function is chosen as $\bar{A} = 2$. The pulses have Gaussian envelopes (22), identical carrier frequencies ($\omega_1 = \omega_2$) and are approximately in resonance with the 0–0 transition of the chromophore, which is typical for SM spectroscopy. The detuning of the carrier frequency,

$$\bar{\omega}_{\text{det}} = \omega_1 - \bar{\varepsilon}/\hbar, \quad (28)$$

as assumed to be of the order of the vibrational frequency $\bar{\Omega}$ and is varied in the simulations. As in the experiments of ref. 7 and 8, we consider short pump pulses ($\tau_p = 10$ fs, $\tau_p \ll \tau_\Omega$) which are capable to create/interrogate vibrational wavepackets.

While the perturbative expressions (18)–(21) could be used for the evaluation of the double-pump SM signal in the weak-coupling regime, we evaluated $I_F(\tau, \phi)$ by numerical solution of the master eqn (12). This is the method of choice in the strong-coupling regime considered in the accompanying paper.¹⁴ Both methods yield identical SM signals in the weak-coupling regime.

The procedure for the numerical solution of the master equation is briefly described as follows. For each particular realization (10) of the model parameters (8), we expand the density matrix in eqn (12) in the eigenfunctions of the vibrational ground-state Hamiltonian and thereby convert the master equation into matrix form. The so obtained system of linear first-order differential equations is solved numerically by a fourth-order Runge–Kutta integrator with a time step 0.25 fs.

The chromophore is assumed to be initially prepared in the vibrational ground state of the electronic ground state.

Since the signals in the weak-coupling regime scale quadratically with the system-field coupling parameter η , it is not of interest to vary η_0 of eqn (7). We thus set $\eta_0 = 0.0025$ eV throughout the paper.

III. SM signals: no stochastic modulation of parameters

In the present section, we analyze SM signals under the assumption that environment-induced modulations of the chromophore parameters (8) can be neglected. This establishes a reference picture for the study of statistical distributions of the parameters in Section IV. In the present section we set $\hat{\mu} = 1$, that is $\eta = \eta_0$.

We start by the investigation of the influence of the detuning of the pump-pulse frequency ω_{det} on the time evolution of the signal. Fig. 2 shows $I_F(\tau, 0)$ for several ω_{det} indicated in the legend. The pulse with $\omega_{\text{det}} = \bar{\Omega}A^2/2 = 2\bar{\Omega}$ excites the chromophore at the vertical excitation energy. The closer ω_{det} is to $2\bar{\Omega}$, the higher is $I_F(\tau, 0)$ and the larger is the amplitude of the vibrational beatings. For negative detunings, on the other hand, the amplitude of these beatings drastically decreases with $|\omega_{\text{det}}|$. Hence vibrational oscillations are barely visible in the two bottom curves in Fig. 2. All signals exhibit beatings with the period $\tau_\Omega = 32$ fs, except the signal for $\omega_{\text{det}} = 2\bar{\Omega}$, which exhibits a twice shorter period. This is a manifestation of the phase factor $\exp(i[\omega_1 - \varepsilon/\hbar]\tau)$ in the expression for the linear response function (27). If, for example, the detuning is $\omega_{\text{det}} = 3\bar{\Omega}$, then $I_F(\tau, 0)$ oscillates with the period $\tau_\Omega/3$ (not shown). For certain detunings, the SM signal therefore reveals not only the fundamental of the vibrational frequency, but also its overtones. Since it is common practice to excite SM chromophores near the 0–0 transition, we set $\bar{\omega}_{\text{det}} = 0$ in the remainder of the paper.

Fig. 3 illustrates the influence of electronic dephasing on double-pump signals by showing $I_F(\tau, 0)$ for four dephasing times. According to eqn (20), the SM signal reveals the linear response function plus a constant background. If electronic dephasing is absent, the signal exhibits vibrational oscillations

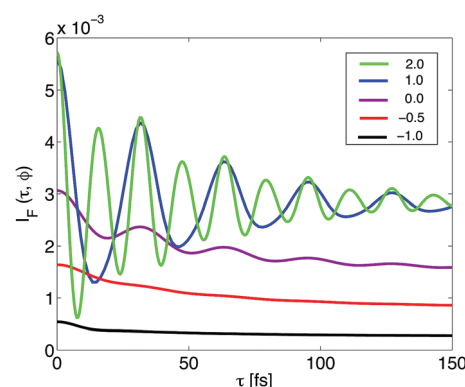


Fig. 2 SM signal $I_F(\tau, 0)$ vs. pulse delay time τ for different pump-pulse detunings $\bar{\omega}_{\text{det}}/\bar{\Omega}$ indicated in the legend. The electronic dephasing time is $\bar{\gamma}^{-1} = 50$ fs.

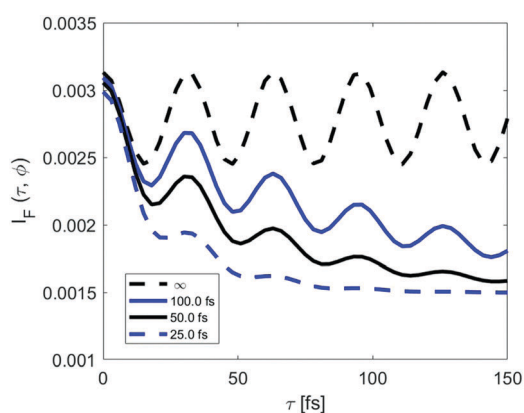


Fig. 3 SM signal $I_F(\tau, 0)$ vs. pulse delay time τ for different dephasing times indicated in the legend.

with a period $\tau_\Omega = 32$ fs and constant amplitude. Dephasing quenches the signal.

It should be noted that the signals in Fig. 3 always decrease at short pulse delay times τ . This behavior is generic for signals in the weak-coupling regime and can be understood as follows. Two coinciding pump pulses ($\tau = 0$) with amplitude E_0 are equivalent to a single pump pulse with amplitude $2E_0$. Hence $I_F(\tau \ll \tau_p, \phi) \sim 4E_0^2$. As τ increases, the two pulses become non-overlapping and act independently, promoting a smaller fraction of the electronic ground-state population to the excited electronic state. This yields the scaling $I_F(\tau \gg \tau_p, \phi) \sim 2E_0^2$. In addition, the $I_F(\tau, 0)$ evaluated with and without electronic dephasing are different at $\tau = 0$. Accidentally, the effect is not very pronounced for the signals in Fig. 3, but for other shifts of the potential-energy surfaces (*e.g.*, for $\bar{A} = 1$ or 4, see Fig. S1 of the ESI†) it is more pronounced. Furthermore, electronic dephasing even may enhance the signal (*e.g.*, for $\bar{A} = 4$, see Fig. S1(b) of the ESI†). This indicates that dephasing during the action of the pulses cannot be neglected. This is a manifestation of the intricate interrelation between the external driving and dephasing/relaxation, which has been studied in detail in ref. 35–38. The simplified formula (27) assumes instantaneous pump pulses and does not capture these effects.

Fig. 4 displays two-dimensional (2D) plots of $I_F(\tau, \phi)$ vs. τ and ϕ , so-called fluorescence maps,^{7,39} which are evaluated without (a) and with (b) electronic dephasing. Panel (a) shows the time-phase profile of the harmonic oscillator wavepacket, while the phase portrait in panel (b) is attenuated on a timescale of ≈ 100 fs due to electronic dephasing. Several general patterns in Fig. 4 can be understood from the following considerations. When two pump pulses overlap ($\tau = 0$) and have relative phase $\phi = \pi$, they cancel each other (destructive interference) and do not excite the chromophore. Overlapping pulses with $\phi = 0, 2\pi$, on the other hand, reinforce each other (constructive interference). Hence 2D maps in the vicinity of $\tau = 0$ exhibit a minimum at $\phi = \pi$ and maxima at $\phi = 0, 2\pi$. Eqn (27) reveals that $I_F(\tau, \phi)$ does not possess mirror symmetry relative to $\phi = \pi$. Correspondingly, the 2D plots in Fig. 4 do not exhibit this symmetry: the time-phase profiles are tilted to the right. This tilt is caused by the phase factor $\exp(-i\phi)$ in eqn (21) and can be considered as a signature of the weak-coupling regime.

IV. SM signals: effect of stochastic modulation of parameters

As has been discussed in Section IIA, a SM measurement for a given delay time τ selects a snapshot system Hamiltonian and a snapshot relaxation operator specifying the master eqn (12). The parameters of the Hamiltonian and relaxation operator vary from measurement to measurement as modeled by eqn (10) and the SM signal is evaluated according to eqn (16). In the present section, we study the effect of these parameter variations and discuss how information about the modulation law can be extracted from the experimental signals. Similar to the measurement protocol of ref. 7 and 9, we assume that the time delay between the pump pulses is scanned with a time step $\Delta\tau = 3$ fs.

Before embarking on simulations, let us discuss physically motivated numerical values of the modulation amplitudes δ_A , where $A = \Omega, \varepsilon, \Delta, \phi, \gamma$. The modulations are caused by the heterogeneity of the environment which the SM chromophore experiences at different measurements, that is, at different time

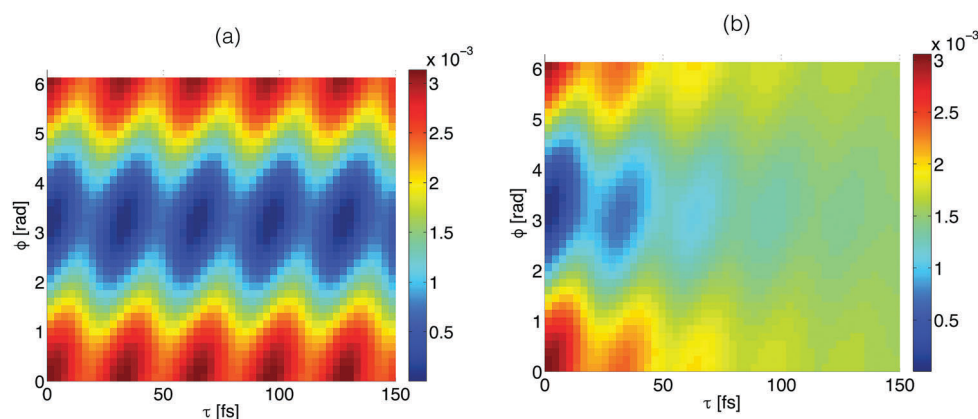


Fig. 4 2D maps $I_F(\tau, \phi)$ for $\bar{\gamma} = 0$ (a) and $\bar{\gamma}^{-1} = 50$ fs (b).

delays between the pump pulses. The amplitude of the electronic energy modulations δ_e is largely responsible for inhomogeneous broadening in ensemble experiments and is a rather well characterized quantity. It should typically be of the order of several hundreds of inverse centimeters ($100 \text{ cm}^{-1} = 0.0124 \text{ eV}$), as revealed *e.g.*, by the steady-state SM experiments at ambient temperatures.^{40,41} In the femtosecond double SM experiments performed with relatively long (75 fs) pulses (no vibrational wavepackets were excited) a rather small value of $\delta_e = 0.0075 \text{ eV}$ was extracted after processing the data for 53 SMs.⁸ In a later experiment performed with interferometric detection of the SM fluorescence, on the other hand, a value was found which is larger by an order of magnitude.²⁵

The modulations of $\hat{e}\hat{\mu}_{12}$ reflect reorientations of the chromophore between measurements. Since the chromophore orientational diffusion times are comparable with the fluorescence lifetimes (see the discussion in Section IIA), unrestricted rotational diffusion would correspond to high a amplitude of δ_ϕ and full chaoticization of $I_F(\tau, \phi)$. This does not happen in the SM experiments of ref. 7 and 9 and corroborates the general physical picture of the restricted chromophore reorientation (wobbling) in the polymer matrix. This restricted diffusion is usually described *via* the diffusion-in-the-cone model,^{42,43} and the value of δ_ϕ can be traced back to the value of the cone angle $\arccos(\delta_\phi)$ within which the chromophore reorientation is restricted. Modulations in the dephasing times extracted from the experiments of ref. 8 scatter by several tens of femtoseconds around a mean value of $\bar{\gamma}^{-1} \approx 50 \text{ fs}$, which also correlates with the frequency-domain SM data.⁴⁰ The parameters characterizing the potential energy surfaces of the chromophores (vibrational frequency Ω and displacement Δ) can also depend on the local environment, but it is difficult to give universal numbers here. In peptides, for example, the energy differences between amide I vibrations are of the order of $10\text{--}100 \text{ cm}^{-1}$, which is 0.6–6% of the vibrational frequency.⁴⁴

Summarizing, we can estimate a range of reasonable values of the modulation amplitudes. However, the simulation of $I_F(\tau, \phi)$ for several typical values of δ_A offers little information about how the modulations affect the signals. To get insight into this problem which goes beyond consideration of a specific chromophore, we will follow two complementary strategies. First, we select the values of δ_A ($A = \Omega, \varepsilon, \Delta, \phi, \gamma$) which produce modulations in $I_F(\tau, \phi)$ of roughly the same amplitudes. This permits us to establish the sensitivity of $I_F(\tau, \phi)$ to the modulation of each particular parameter (Section IVA). Second, for each δ_A ($A = \Omega, \varepsilon, \Delta, \phi, \gamma$) we establish the critical values for which $I_F(\tau, \phi)$ becomes chaotic such that vibrational beatings become undetectable (Section IVB).

A. Sensitivity of the signal to the parameter modulations

We begin our discussion with Fig. 5, which illustrates how $I_F(\tau, 0)$ (black line) and $I_F(\tau, \pi)$ (blue line) are affected by the modulation of the parameters. Fig. 5(a), in which the signals are evaluated for the mean values of the parameters (8), establishes the reference picture. Both $I_F(\tau, 0)$ and $I_F(\tau, \pi)$ exhibit damped oscillations with the period $\tau_\Omega = 32 \text{ fs}$ and approach

the same constant background for $\tau \gg \bar{\gamma}^{-1}$, because the time-dependent contribution to the signal decays to zero due to electronic dephasing. As has been explained in the previous section, $I_F(0, \pi) = 0$ and therefore $I_F(\tau, \pi)$ increases non-monotonically towards its background value. On the other hand, $I_F(0, 0) \neq 0$ and $I_F(\tau, 0)$ decreases non-monotonically towards the same constant background. $I_F(\tau, 0)$ and $I_F(\tau, \pi)$ oscillate in anti-phase: maxima of $I_F(\tau, 0)$ correspond to minima of $I_F(\tau, \pi)$ and *vice versa*. This is a direct consequence of the $\sim \exp(-i\phi)$ phase dependence of the SM signal in eqn (27). The anti-phase evolution of the signals is a signature of the weak-coupling regime, and several SM signals of ref. 7 and 8 clearly exhibit this behavior. A related observation is that $I_F(\tau, 0)$ and $I_F(\tau, \pi)$ are exact mirror images of each other, so that $(I_F(\tau, 0) + I_F(\tau, \pi))/2$ is τ -independent, being proportional to the constant background. Hence, a nearly constant value of $I_F(\tau, 0) + I_F(\tau, \pi)$ also can be considered as a witness of the weak-coupling regime.

Fig. 5(b)–(f) show the same signal, but evaluated with parameter modulations as specified in the figure caption. The signals in panels (b)–(f) look like noisy versions of the signal in panel (a), but the vibrational beatings with the period $\tau_\Omega = 32 \text{ fs}$ remain clearly visible. The numerical values of the amplitude of modulations δ_A ($A = \Omega, \varepsilon, \Delta, \phi, \gamma$) were selected to produce fluctuations of roughly the same amplitude in the panels (b) through (f). This choice of δ_A illustrates the sensitivity of SM signals to modulations of specific parameters. Indeed, $\delta_\Omega = 0.007 \text{ eV}$ represents 5.4% of the mean vibrational frequency; $\delta_\Delta = 0.04$ represents 2% of the mean displacement of the potential energy function; $\delta_\phi = 0.03$ represents 3% of the mean coupling parameter $\eta = \eta_0(\hat{e}\hat{\mu})$; $\delta_{\gamma^{-1}} = 20 \text{ fs}$ represents 40% of the mean electronic dephasing. Hence, the parameters can be arranged in the order of decreasing sensitivity of the SM signal as follows: $\Delta, \eta, \Omega, \gamma$.

These results can be rationalized as follows. Modulations of Δ modify Franck–Condon factors which scale $\sim \exp\{-\Delta^2/2\}$ and are responsible for Gaussian dependence of $I_F(\tau, \phi)$ on Δ (see eqn (21) and (27)). The parameter ($\hat{e}\hat{\mu}$) controls the system-field coupling η and even relatively small variations of it produce tangible effects on the signal, because $I_F(\tau, \phi) \sim \eta^2$. Interestingly, the signal in panel (e) of Fig. 5 (which exhibits orientational modulations) is the only one which increases at very short τ . Since $I_F(\tau, \phi) \sim \eta^2$, a relatively small increase of the system-field coupling η can beat the decrease of the signal owing to optical dephasing. The sensitivity of the double-pump signals to modulations of chromophore orientations has been emphasized in ref. 7–9 and 11. $I_F(\tau, \phi)$ is quite sensitive to modulations of the vibrational frequency, because Ω determines the period of vibrational beatings. Dephasing controls the rate of decay of the signal in the weak-coupling regime (see eqn (27)). The exponential dependence of $I_F(\tau, \phi)$ on γ is much weaker than Gaussian dependence of $I_F(\tau, \phi)$ on Δ , hence a relatively low sensitivity of the signal to fluctuations of γ . Modulations of the electronic energy ε cannot be considered in the above manner, because the absolute value of ε does not matter in the present context. However, the sensitivity of the signal to changes of ε

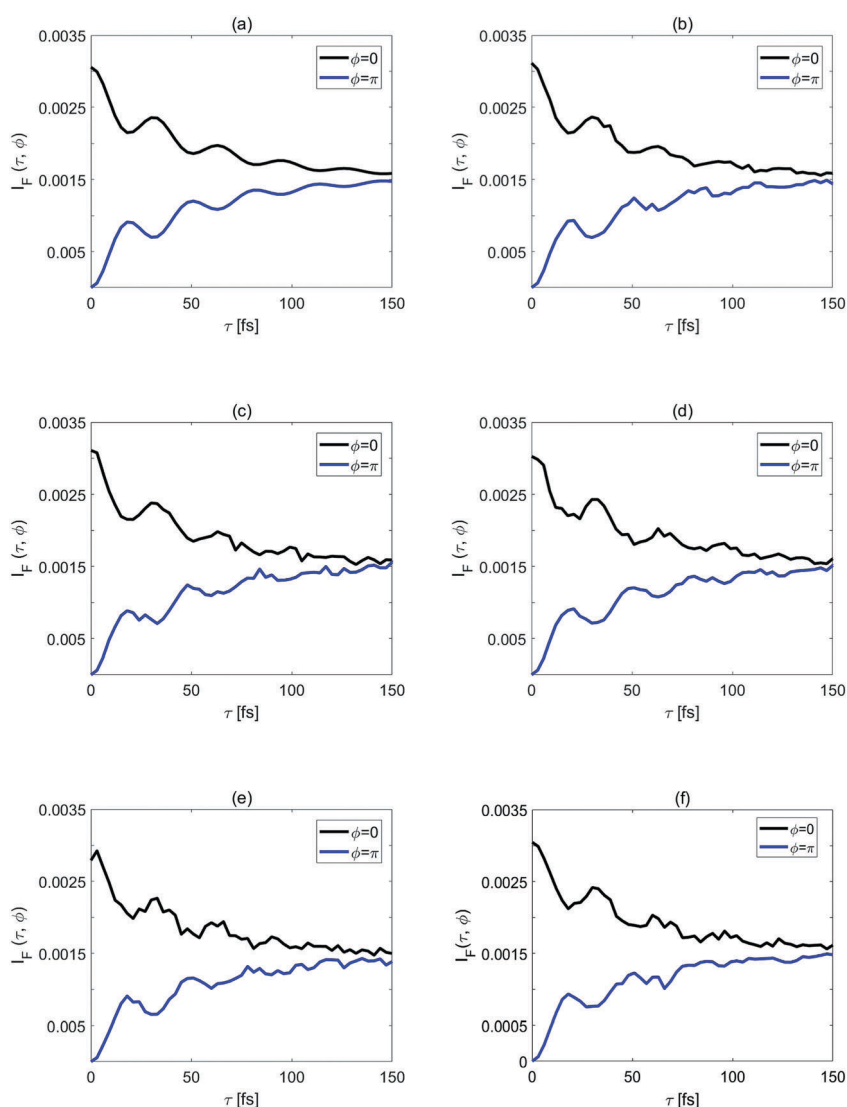


Fig. 5 Panel (a) depicts the SM signal $I_F(\tau, 0)$ (black line) and $I_F(\tau, \pi)$ (blue line) evaluated for the following mean values of the parameters: $\bar{\Omega} = 0.13$ eV, $\bar{\omega}_{\text{det}} = 0$, $\bar{A} = 2$, $\bar{\delta}\hat{\mu} = 1$, and $\bar{\gamma}^{-1} = 50$ fs. Panels (b–f) show the effect of modulation of the vibrational frequency, $\delta_{\Omega} = 0.007$ eV (b); electronic energy, $\delta_{\varepsilon} = 0.01$ eV (c); displacement of the potential energy function, $\delta_A = 0.04$ (d); molecular orientation, $\hat{\mathbf{e}}\hat{\mu} = \cos(\pi/4 - \varphi)/\cos(\pi/4)$, $\delta_{\varphi} = 0.1$ (e); electronic dephasing, $\delta_{\gamma^{-1}} = 20$ fs (f). The signals are evaluated with a discretization step of 3 fs in τ .

decreases for short pulses, because the interaction of the chromophore with Dirac-delta pulses is independent of the electronic energy and the pulse carrier frequency.

Fig. 6 displays the effect of the simultaneous modulations of all parameters on $I_F(\tau, 0)$ and $I_F(\tau, \pi)$. Rather surprisingly, the level of noise in Fig. 6 is comparable with that in Fig. 5(b)–(f). The reason is that the changes in $I_F(\tau, \pi)$ are induced by the low-amplitude modulations of the five parameters. Modulations due to each of these parameters may either increase or decrease the signal. Taken together, they largely cancel each other.

Fig. 7 illustrates how the modulation of the parameter ε affects the 2D maps $I_F(\tau, \phi)$. For comparison, Fig. 4 displays the same signals but without modulations. Since the amplitude of the modulation of ε is chosen to be relatively small, the 2D maps in Fig. 7 look like blurred versions of those in Fig. 4.

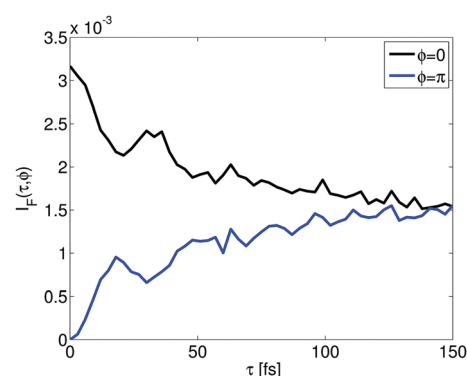


Fig. 6 $I_F(\tau, 0)$ (black line) and $I_F(\tau, \pi)$ (blue line) evaluated with the simultaneous modulations of the parameters $A = \Omega, \varepsilon, \Delta, \varphi, \gamma$. The numerical values of δ_A are given in the caption for Fig. 5.

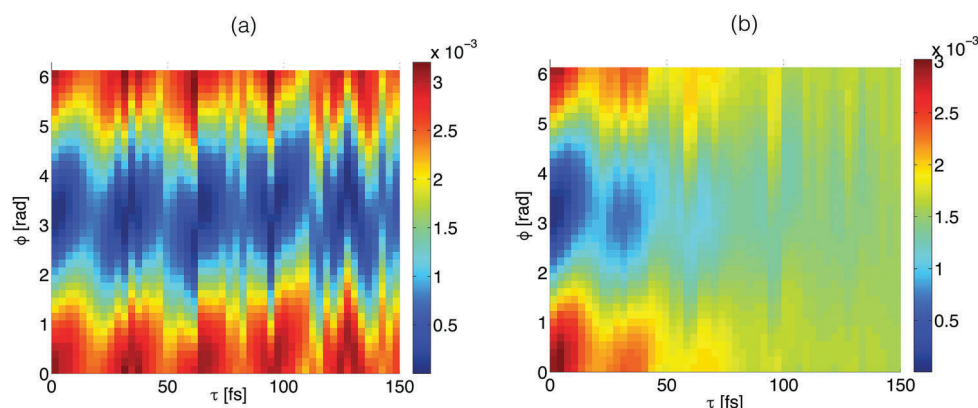


Fig. 7 2D maps $I_F(\tau, \phi)$ for $\bar{\gamma} = 0$ (a) and $\bar{\gamma}^{-1} = 50$ fs (b). The electronic energy ε is sampled according to eqn (10) with $\delta_\varepsilon = 0.01$ eV.

B. Critical values of the modulation amplitudes

Obviously, the level of noise in the SM signal increases with the amplitude of the modulations. It is therefore instructive to establish critical values of δ_A for which $I_F(\tau, \phi)$ loses discernible vibrational beatings. This is illustrated by Fig. 8 and 9 which, respectively, exemplify the effect of the electronic energy modulations and orientational modulations. In Fig. 8, the magnitude of δ_{ε_2} is twice (a) and three times (b) higher than that in Fig. 5(c). In Fig. 9, the magnitude of δ_ϕ is twice (a) and three times (b) higher than that in Fig. 5(e).

The effect of increasing amplitude of modulation on the signals in Fig. 8 and 9 is qualitatively very similar. Vibrational beatings are still discernible in panel (a) but barely visible in panel (b) of Fig. 8 and 9. The changes of $I_F(\tau, \phi)$ with the amplitudes of other relevant parameters look qualitatively very similar and are presented in the ESI[†] (Fig. 2–4). The critical values of the modulation amplitudes, that is the values of δ_A for which vibrational beatings in $I_F(\tau, \phi)$ become buried in noise, are collected in Table 1. The existence of these critical values reveals certain limitations on the information content of SM experiments.

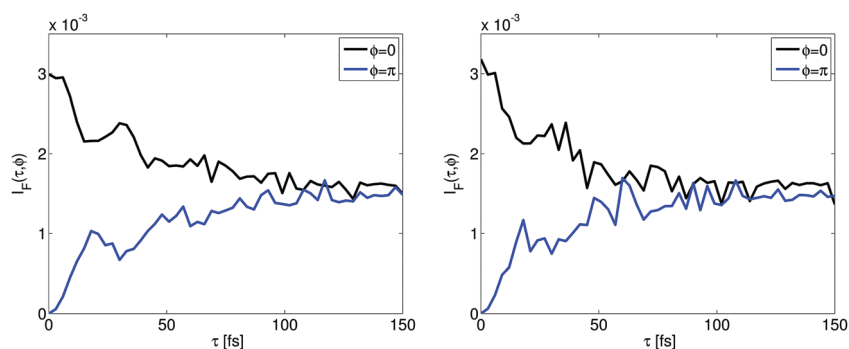


Fig. 8 $I_F(\tau, 0)$ (black line) and $I_F(\tau, \pi)$ (blue line) for different amplitudes of the electronic energy modulation: $\delta_{\varepsilon_2} = 0.02$ eV (left panel) and 0.03 eV (right panel). The remaining parameters assume the mean values as for Fig. 5(a).

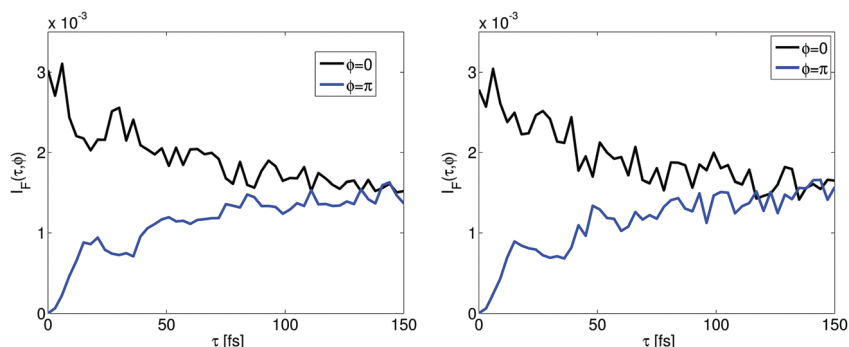


Fig. 9 $I_F(\tau, 0)$ (black line) and $I_F(\tau, \pi)$ (blue line) for different amplitudes of the molecular orientation, $\hat{\mathbf{e}}_{\mu_{12}} = \cos(\pi/4 - \phi)/\cos(\pi/4)$, $\delta_\phi = 0.2$ (left panel) and 0.3 (right panel). The remaining parameters assume the mean values as for Fig. 5(a).

Table 1 Critical values of the amplitude modulations

δ_{Ω} (eV)	δ_{ε} (eV)	δ_A	δ_{ϕ} (°)	$\delta_{\gamma^{-1}}$ (fs)
0.028	0.03	0.2	17	50

We have assumed that the parameters (8) vary according to the modulation law (10). SM signals simulated with a Gaussian modulation of the parameters look qualitatively similar to those in Fig. 5 and 6 and are presented in the ESI† (Fig. 5 and 6). An interesting question is whether one can uncover the underlying modulation law by analyzing SM signals. We believe that the answer is positive due to the following considerations. Usually, signals of several individual chromophores are measured.⁷ A natural way to process these data is to fit the signal of each individual chromophore to an appropriate trial function (for example, eqn (27)) and thus obtain distributions of the parameters (8). This approach has been chosen in ref. 7–9. However, as emphasized in the present work, each time delay τ may require specific parameters and fitting signals $I_F(\tau, \phi)$ for all τ by the same set of parameters may not be justified. Hence, an alternative analysis may be appropriate. Let us assume that several transients $I_F(\tau, \phi, n)$ ($n = 1, 2, \dots, N$) have been obtained. If N is large enough, the ensemble signal can be evaluated as $\bar{I}_F(\tau, \phi) = N^{-1} \sum_n I_F(\tau, \phi, n)$. This has been demonstrated in ref. 7, where the ensemble double-pump signal was recovered by the averaging of 52 SM signals. We suggest that also the variance $N^{-1} \sum_n I_F(\tau, \phi, n)^2 - \bar{I}_F(\tau, \phi)^2$ (which is not accessible in ensemble spectroscopy) as well as higher-order moments of the SM signal should be considered. These observables can be evaluated even if individual SM transients are rather noisy. This analysis may provide insight into stochastic properties (e.g. Gaussian vs. uniform or classical vs. quantum) of the environment-induced modulations. An interesting possibility related to the above suggestion has recently been demonstrated in ref. 45.

V. Conclusions

We have developed a theoretical description of femtosecond double-pump SM signals for a simple model of the chromophore and its environment. It is based on driven master equations for the density matrix of the chromophore and is applicable in both weak-coupling and strong-coupling regimes. In this paper, we concentrated on a detailed study of the weak-coupling regime. In this case, the signal is determined by the linear response function which can be evaluated analytically for the displaced harmonic oscillator model. For numerical illustrations, we considered a chromophore with a single high-frequency Franck-Condon-active vibrational mode. We studied how slow modulations of relevant molecular parameters due to an environment at ambient temperature affect the SM signals. We propose that information on these statistical modulations can be obtained by the analysis of a sufficiently large set of SM signals.

The simulated double-pump SM signals exhibit vibration-induced beatings of the electronic coherence of the density matrix of the chromophore that are quenched by electronic dephasing. The signals evaluated with a phase difference of 0 and π are mirror images of each other and their mean value is delay time independent. They oscillate in anti-phase: maxima of the former signal correspond to minima of the latter signal and *vice versa*. These features are signatures of the weak-coupling regime and several SM signals of ref. 7 and 8 clearly exhibit this behavior. 2D maps of SM signals show a pronounced tilt of the phase-time profiles. This tilt also is characteristic of the weak-coupling regime. The signals in the strong-coupling regime are studied in the accompanying paper.¹⁴

Conflicts of interest

There are no conflicts to declare.

Acknowledgements

This work has been supported by the Deutsche Forschungsgemeinschaft (DFG) through a research grant and the DFG-Cluster of Excellence “Munich-Centre for Advanced Photonics” (www.munich-photonics.de). E. P.-G. acknowledges support by the International Max-Planck Research School of Advanced Photon Science (www.mpq.mpg.de/APS).

References

- P. Tamarat, A. Maali, B. Lounis and M. Orrit, *J. Phys. Chem. A*, 2000, **104**, 1.
- Y. Jung, E. Barkai and R. Silbey, *J. Chem. Phys.*, 2002, **117**, 10980.
- M. Orrit, T. Ha and V. Sandoghdar, *Chem. Soc. Rev.*, 2014, **43**, 973.
- W. E. Moerner, *Rev. Mod. Phys.*, 2015, **87**, 1183.
- W. E. Moerner, Y. Shechtman and Q. Wang, *Faraday Discuss.*, 2015, **184**, 9–36.
- M. Orrit and J. Bernard, *Phys. Rev. Lett.*, 1990, **65**, 2716.
- D. Brinks, F. D. Stefani, F. Kulzer, R. Hildner, T. H. Haminiou, Y. Avlasevich and N. F. van Hulst, *Nature*, 2010, **465**, 905.
- R. Hildner, D. Brinks, F. D. Stefani and N. F. van Hulst, *Phys. Chem. Chem. Phys.*, 2011, **13**, 1888–1894.
- R. Hildner, D. Brinks and N. F. van Hulst, *Nat. Phys.*, 2011, **7**, 172.
- D. Brinks, R. Hildner, F. D. Stefani and N. F. van Hulst, *Faraday Discuss.*, 2011, **153**, 51.
- D. Brinks, R. Hildner, E. M. H. P. van Dijk, F. D. Stefani, J. B. Nieder, J. Hernando and N. F. van Hulst, *Chem. Soc. Rev.*, 2014, **43**, 2476–2491.
- L. Piatkowski, N. Accanto and N. F. van Hulst, *ACS Photonics*, 2016, **3**, 1401.
- N. F. Scherer, R. J. Carlson, A. Matro, M. Du, A. J. Ruggiero, V. Romero-Rochin, J. A. Cina, G. R. Fleming and S. A. Rice, *J. Chem. Phys.*, 1991, **95**, 1487.

- 14 E. Palacino-González, M. F. Gelin and W. Domcke, *Theoretical aspects of femtosecond double-pump single-molecule spectroscopy. II. Strong-field regime*, DOI: 10.1039/C7CP04810F.
- 15 R. Kubo, *Adv. Chem. Phys.*, 1969, **15**, 101.
- 16 S. Mukamel, *Principles of Nonlinear Optical Spectroscopy*, Oxford University Press, New York, 1995.
- 17 Y. Avlasevich, S. Müller, P. Erk and K. Müllen, *Chem. – Eur. J.*, 2007, **13**, 6555.
- 18 L. S. Cederbaum and W. Domcke, *J. Chem. Phys.*, 1976, **64**, 603.
- 19 S. Mukamel, S. Abe, Y. J. Yan and R. Islampour, *J. Phys. Chem.*, 1985, **89**, 201.
- 20 V. Chernyak and S. Mukamel, *J. Chem. Phys.*, 2001, **114**, 10430.
- 21 R. Borrelli and A. Peluso, *J. Chem. Theory Comput.*, 2014, **11**, 415.
- 22 M. F. Gelin, W. Domcke and B. J. Rao, *J. Chem. Phys.*, 2016, **144**, 184307.
- 23 A. W. Albrecht, J. D. Hybl, S. M. Gallagher Faeder and D. M. Jonas, *J. Chem. Phys.*, 1999, **111**, 10934.
- 24 Z. Zhang, K. L. Wells, E. W. J. Hyland and H.-S. Tan, *Chem. Phys. Lett.*, 2012, **550**, 156.
- 25 L. Piatkowski, E. Gellings and N. F. van Hulst, *Nat. Commun.*, 2015, **7**, 1.
- 26 A. Weigel, A. Sebesta and P. Kukura, *J. Phys. Chem. Lett.*, 2015, **6**, 4032.
- 27 M. F. Gelin, Y. Tanimura and W. Domcke, *J. Chem. Phys.*, 2013, **139**, 214302.
- 28 S. Yampolsky, D. A. Fishman, S. Dey, E. Hulkko, M. Banik, E. O. Potma and V. A. Apkarian, *Nat. Photonics*, 2014, **8**, 650.
- 29 M. F. Gelin and D. S. Kosov, *J. Chem. Phys.*, 2006, **125**, 054708.
- 30 C. W. Gardiner, *Handbook of Stochastic Methods*, Springer-Verlag Berlin Heidelberg, New York, 1997.
- 31 D. Suess, A. Eisfeld and W. T. Strunz, *Phys. Rev. Lett.*, 2014, **113**, 150403.
- 32 P. Malý, J. M. Gruber, R. van Grondelle and T. Mančal, *Sci. Rep.*, 2016, **6**, 26230.
- 33 L. Chen, M. F. Gelin, W. Domcke and Y. Zhao, *J. Chem. Phys.*, 2015, **142**, 164106.
- 34 Generalization of this formula towards chromophores with several Franck–Condon-active modes is straightforward.
- 35 G. Ashkenazi, R. Kosloff and M. Ratner, *J. Am. Chem. Soc.*, 1999, **21**, 3386.
- 36 E. Geva, *J. Chem. Phys.*, 2002, **116**, 1629.
- 37 D. Egorova, M. F. Gelin, M. Thoss, W. Domcke and H. Wang, *J. Chem. Phys.*, 2008, **129**, 214303.
- 38 M. F. Gelin, D. Egorova and W. Domcke, *J. Chem. Phys.*, 2009, **131**, 124505.
- 39 2D maps reported in ref. 7 and 10 reveal the four-wave-mixing contribution $I_4(\tau, \phi)$ to the SM signal $I_F(\tau, \phi)$.
- 40 M. Haase, C. G. Hübner, F. Nolde, K. Müllen and T. Basché, *Phys. Chem. Chem. Phys.*, 2011, **13**, 1776.
- 41 M. Mitsui, H. Fukui, R. Takahashi, Y. Takakura and T. Mizukami, *J. Phys. Chem. A*, 2017, **121**, 1577.
- 42 G. Lipari and A. Szabo, *J. Am. Chem. Soc.*, 1982, **104**, 4546.
- 43 V. A. Jarymowycz and M. J. Stone, *Chem. Rev.*, 2006, **106**, 1624.
- 44 S. Woutersen and P. Hamm, *J. Phys.: Condens. Matter*, 2002, **14**, R1035.
- 45 T. D. M. Bell and A. H. A. Clayton, *Sci. Rep.*, 2015, **5**, 8158.

Paper 3

‡

‡ **Theoretical aspects of femtosecond double-pump single-molecule spectroscopy II. Strong-field regime.** E. Palacino-González, M. F. Gelin and W. Domcke, *Phys. Chem. Chem. Phys.*, **19**, 32307-32319 (2017). DOI: 10.1039/c7cp0481of



Cite this: DOI: 10.1039/c7cp04810f

Theoretical aspects of femtosecond double-pump single-molecule spectroscopy. II. Strong-field regime

Elisa Palacino-González,  Maxim F. Gelin* and Wolfgang Domcke

We investigate femtosecond double-pump single-molecule signals in the strong-field regime, which is characterized by nonlinear scaling of the signal with the intensity of the pump pulses. The signals can be decomposed into population and coherence contributions. In contrast to the weak-field regime (in which only the coherence contribution is important) both contributions are relevant in the strong-field regime and reveal the vibrational dynamics of the chromophore. Other than in the weak-field regime, the detection of vibrational beatings is not limited by the electronic dephasing time of the chromophore. Moreover, the signals in the strong-field regime are more robust with respect to the environment-induced modulation of the chromophore parameters. It is shown that excited-state absorption in chromophores with three electronic states is reflected in the phase dependence of single-molecule signals. The simulations reveal that the information content of femtosecond double-pump single-molecule signals is enhanced in the strong-coupling regime.

Received 17th July 2017,
Accepted 20th November 2017

DOI: 10.1039/c7cp04810f

rsc.li/pccp

I. Introduction

The advent of picosecond and femtosecond lasers has revolutionized the field of molecular electronic spectroscopy, allowing researchers the monitoring of vibrational wave packets and the making/breaking of chemical bonds in ensembles of various molecular species in real time.¹ Very recently, it has been demonstrated that responses of individual molecules in condensed-phase environments can be probed with femtosecond time resolution. Femtosecond time resolution has been brought to the field of single-molecule (SM) spectroscopy by van Hulst and coworkers.^{2–7} This group has developed double-pump femtosecond SM spectroscopy, which combines the fluorescence detection of SMs pioneered by Orrit and Bernard⁸ with pulse-shaping and the double-pump excitation scheme pioneered in femtosecond ensemble spectroscopy by Scherer and co-workers.⁹ In this technique, the fluorescence of individual chromophores is scanned *vs.* the time delay between two phase-locked pump pulses. This scheme reconciles the fluorescence detection of molecular responses (which usually is associated with a nanosecond time scale) with femtosecond time resolution, allowing the interrogation of the dynamics of individual chromophores influenced by their local environment at ambient temperature.

In the accompanying paper,¹⁰ we have developed a theoretical description of double-pump femtosecond SM spectroscopy and applied it to simulate signals of individual chromophores in the weak-field regime, where the SM signal scales linearly with the intensity of the pump pulses. The weak-field regime applies if the electric field of the two pump pulses is comparatively weak or if the projection of the transition-dipole moment vector of the chromophore on the polarization vector of the pump pulses is small. The weak-field/strong-field regimes are therefore not only governed by the strength of the laser pulses, but also by the orientation of the selected chromophore. In the present work, we systematically study SM signals in the strong-field regime, which is characterized by the nonlinear scaling of the signal with the intensity of the pump pulses.

In SM spectroscopy, exceptionally photostable chromophores with large transition dipole moments are usually employed. An earlier variant of the SM pump-probe experiments by van Hulst and coworkers relied on strong laser pulses and saturation effects.¹¹ The same experimental method has also been successfully applied to individual multichromophore systems, such as the light harvesting complex LH2 of purple bacteria.¹² In these experiments, the phases of the laser pulses were not controlled and the time resolution was limited to several hundreds of femtoseconds. More recent femtosecond double-pump SM experiments with phase-locked pulses, which monitored the electronic coherences of the chromophore's density matrix, were performed with weak-to-moderate pump pulses, although the possibility of the detection of SM signals in the strong-field regime was also clearly demonstrated.²

Department of Chemistry, Technische Universität München, D-85747, Garching, Germany. E-mail: maxim.gelin@ch.tum.de

Usually, chromophores in SM experiments are statistically oriented in a polymer matrix, and the chromophore-field coupling varies between weak and strong. This indicates that femtosecond double-pump SM spectroscopy is inherently in the strong-field regime when the orientation of the transition dipole moment is nearly parallel to the polarization of the pump pulses. Hence, a perturbative theory in the molecule-field interaction^{13–15} may be not a universally useful approach and a non-perturbative description of SM signals is required. Herein, we analyze strong-field effects in double-pump SM spectroscopy.

II. Hamiltonian, equation of motion and SM signal

A framework for the theoretical description and the simulation of double-pump SM signals has been developed in the preceding paper.¹⁰ There, we considered chromophores with just two electronic states, the electronic ground state S_0 and a single bright excited electronic state S_1 . This level of description is sufficient in the weak-field regime. Photostable chromophores used in SM experiments can sometimes be considered as electronic two-state systems even in the strong-field regime, because optical coupling of S_1 to higher lying excited electronic states S_n ($n \geq 1$) can be minimized by a judicious choice of the chromophore (for example, by choosing a chromophore which does not exhibit excited-state absorption in the spectral range of interest). However, transitions to/from higher-lying electronic states cannot in general be ignored in the strong-field regime. In principle, the radiative coupling of S_1 to S_n is an undesirable process in SM spectroscopy, because any photochemistry occurring in S_n states may destroy the chromophore.¹⁶ There exist several exceptions though. Excited-state absorption is used in the pump-probe optical microscopy of non-fluorescent chromophores to learn about their local environment.^{17,18} Pump-probe force microscopy of nanostructures, which also involves excited-state absorption, has reached picosecond time resolution and may soon be optimized towards the detection of individual chromophores.¹⁹ In general, S_n states are expected to undergo rapid deactivation owing to

intra-chromophore processes or interactions with the environment. Carefully chosen chromophores may nevertheless survive several measurement cycles and their S_n states may contribute to double-pump SM signals. In the present work, we therefore include a higher-lying second excited electronic state in the model of the chromophore.

We consider a chromophore with the electronic ground state $|1\rangle$, a bright excited electronic state $|2\rangle$, and a higher-lying excited electronic state $|3\rangle$. The Hamiltonian specifying an individual chromophore is written as a 3×3 matrix in the electronic state space,

$$H = \begin{pmatrix} h_1 & 0 & 0 \\ 0 & \varepsilon_2 + h_2 & 0 \\ 0 & 0 & \varepsilon_3 + h_3 \end{pmatrix}, \quad (1)$$

where the ε_k are adiabatic electronic excitation energies from the electronic ground state and h_k are the vibrational Hamiltonians ($k = 1, 2, 3$) of a specific chromophore detected in the SM experiment. For simplicity, we consider chromophores with a single Franck-Condon-active harmonic vibrational mode²⁰ with frequency Ω , dimensionless momentum P , and dimensionless coordinate Q ,

$$\begin{aligned} h_1 &= \frac{\hbar\Omega}{2}(P^2 + Q^2), \\ h_2 &= \frac{\hbar\Omega}{2}(P^2 + (Q - \Delta_2)^2), \\ h_3 &= \frac{\hbar\Omega}{2}(P^2 + (Q - \Delta_3)^2). \end{aligned} \quad (2)$$

Here Δ_2 and Δ_3 are dimensionless shifts of the potential energy functions in the excited states $|2\rangle$ and $|3\rangle$ with respect to the minimum of the ground-state potential-energy function (see Fig. 1). The remaining modes of the chromophore as well as the vibrational degrees of freedom of the polymer matrix will be considered as an environment. The influence of the environment on the chromophore dynamics will be described by relaxation operators in the master equation (see below).

In the dipole approximation and in the rotating wave approximation, the interaction of the chromophore with a pair of phase-locked pulses is specified by the Hamiltonian

$$H_F(t) = -[E(t)X^\dagger + E^*(t)X], \quad (3)$$

where

$$\begin{aligned} E(t) &= E_1(t) + E_2(t), \\ E_1(t) &= E_0 f(t + \tau) e^{-i\omega_1 t}, \\ E_2(t) &= E_0 f(t) e^{i(\phi - \omega_2 t)} \end{aligned} \quad (4)$$

and

$$X = \begin{pmatrix} 0 & \hat{\boldsymbol{\mu}}_{12} & 0 \\ 0 & 0 & \hat{\boldsymbol{\mu}}_{23} \\ 0 & 0 & 0 \end{pmatrix}, \quad X^\dagger = \begin{pmatrix} 0 & 0 & 0 \\ \hat{\boldsymbol{\mu}}_{12} & 0 & 0 \\ 0 & \hat{\boldsymbol{\mu}}_{23} & 0 \end{pmatrix}. \quad (5)$$

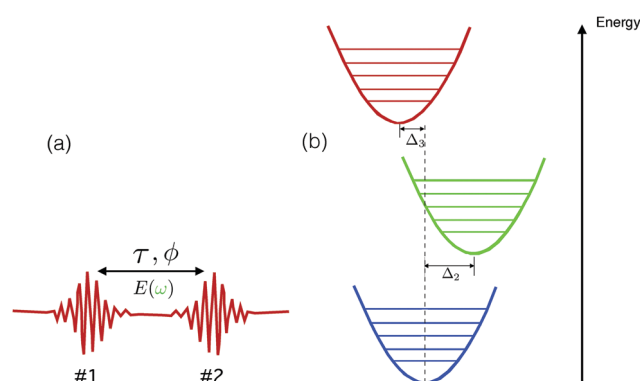


Fig. 1 (a) Sketch of a pair of phase-locked pump pulses. (b) Schematic view of the potential-energy functions of a chromophore with three electronic states.

are transition dipole moment operators, μ_{12} and μ_{23} are their matrix elements, and \hat{e} is the unit vector of the polarization of the two pump pulses. In eqn (4), E_0 and $f(t)$ are the amplitude and the dimensionless envelope of the pulses, ω_1 and ω_2 are their carrier frequencies, τ is the time delay between the pulses, and ϕ is their relative phase. For convenience, the arrival of the first pulse is set to $t = -\tau$ so that the second pulse arrives at $t = 0$.

It is convenient to introduce the chromophore-field coupling parameters

$$\eta_{12} = \eta_{12}^{(0)}(\hat{e}\hat{\mu}_{12}), \quad \eta_{23} = \eta_{23}^{(0)}(\hat{e}\hat{\mu}_{23}) \quad (6)$$

where

$$\eta_{12}^{(0)} = E_0\mu_{12}, \quad \eta_{23}^{(0)} = E_0\mu_{23}, \quad (7)$$

$\hat{\mu}_{12}$ and $\hat{\mu}_{23}$ are the unit vectors along the transition dipole moments, $\mu_{12} = |\mu_{12}|$ and $\mu_{23} = |\mu_{23}|$. Eqn (6) shows that the system-field coupling in the SM experiment is determined by two actors: constant factors ($\eta_{12}^{(0)}$ and $\eta_{23}^{(0)}$, which are fixed for experiments with a given chromophore) and random factors ($\hat{e}\hat{\mu}_{12}$ and $\hat{e}\hat{\mu}_{23}$, which may change from one SM measurement to another due to reorientation of the chromophore). Chromophores suitable for double-pump SM spectroscopy usually exhibit large transition dipole moments.²¹ Therefore, η_{12} and η_{23} can be in the strong-coupling regime even for a rather moderate field amplitude E_0 if $\hat{e}\hat{\mu}_{12} \approx 1$ and $\hat{e}\hat{\mu}_{23} \approx 1$.

The ensemble of chromophores is highly heterogeneous and the parameters specifying the Hamiltonians (1) and (3),

$$\varepsilon_2, \varepsilon_3, \Omega, \Delta_2, \Delta_3, \hat{e}\hat{\mu}_{12}, \text{ and } \hat{e}\hat{\mu}_{23}, \quad (8)$$

depend on the local environment of the chromophore. Below we describe how this effect is accounted for in the present work (the details can be found in the accompanying paper¹⁰). In a typical femtosecond SM experiment, the signal as a function of the time delay τ is detected with a certain time step Δ_τ ,

$$\tau = j\Delta_\tau, \quad j = 0, 1, 2, \dots \quad (9)$$

Since Δ_τ is much longer than any relevant microscopic time scale of the electron-vibrational dynamics of the single chromophore, there is no correlation between the values of the parameters (8) in any two consecutive measurements. Hence we can assume that at every time delay (9) the parameters can take random values according to the modulation law

$$A_\tau = \bar{A} + \delta_A(r_\tau - 1/2). \quad (10)$$

Here A_τ is a stochastic realization of any parameter from the list (8), \bar{A} represents its mean value, δ_A controls the amplitude of the modulation, and r_τ is a random number uniformly distributed in the interval $[0, 1]$.

Each particular realization of the parameters (8) produces a snapshot (τ -dependent) system Hamiltonian H and a snapshot

system-field interaction Hamiltonian $H(t)$. The time evolution of such a chromophore is described by the density matrix

$$\rho(t) = \begin{pmatrix} \rho_{11}(t) & \rho_{12}(t) & \rho_{13}(t) \\ \rho_{21}(t) & \rho_{22}(t) & \rho_{23}(t) \\ \rho_{31}(t) & \rho_{32}(t) & \rho_{33}(t) \end{pmatrix}.$$

obeying the master equation

$$\frac{\partial \rho(t)}{\partial t} = -\frac{i}{\hbar}[H + H_F(t), \rho(t)] + \Gamma \rho(t). \quad (11)$$

The snapshot (τ -dependent) relaxation operator Γ accounts for the pure electronic dephasing and is given by (cf. ref. 10)

$$\Gamma \rho(t) = -\gamma_2 \begin{pmatrix} 0 & \rho_{12}(t) & 0 \\ \rho_{21}(t) & 0 & \rho_{23}(t) \\ 0 & \rho_{32}(t) & 0 \end{pmatrix} - \gamma_3 \begin{pmatrix} 0 & 0 & \rho_{13}(t) \\ 0 & 0 & 0 \\ \rho_{31}(t) & 0 & 0 \end{pmatrix}, \quad (12)$$

where γ_2 and γ_3 are the dephasing rates of the single (1, 2 and 2, 3) and double (1, 3) electronic coherences, respectively.

The signal is the total fluorescence of a single chromophore detected as a function of the interpulse delay τ and the relative phase ϕ . We identify this signal with the total population of the excited electronic state of the chromophore after the action of the second pump pulse,

$$I_F(\tau, \phi) = \text{Tr}\{\rho_{22}(t_\tau)\}. \quad (13)$$

Here the trace is taken with respect to vibrational degrees of freedom of the chromophore and t_τ is a time moment after the action of the second pump pulse. Eqn (1)–(12) fully specify the dynamics of the SM chromophore and eqn (13) specifies the double-pump SM signal which, in addition to its explicit dependence on τ , depends parametrically on τ owing to random realizations of the chromophore parameters according to eqn (10). The assumptions underlying this description have been discussed in detail in the preceding paper.¹⁰

III. Analytical results

A number of general trends and features in the behavior of SM signals can be understood without numerical simulations. The intensity of the double-pump SM signal can be expanded as^{10,22}

$$I_F(\tau, \phi) = \sum_{k=2,4,6,\dots} I_k(\tau, \phi), \quad (14)$$

where k corresponds to the number of interactions of the chromophore with the laser pulses. Therefore $I_k(\tau, \phi) \sim E_0^k$. For sufficiently weak pulses, the signal is represented by $I_2(\tau, \phi)$, scales linearly with the pulse intensity, and can be evaluated analytically.¹⁰ For stronger chromophore-field coupling, higher-order terms in the expansion (14) are relevant. The k -wave-mixing contribution to the double-pump signal consists of two terms,

$$I_k(\tau, \phi) = I_k + \tilde{I}_k(\tau, \phi).$$

Here I_k describes a τ - and ϕ -independent background, which results from the interaction of the chromophore with just one of the pump pulses. The τ - and ϕ -dependent contribution $\tilde{I}_k(\tau, \phi)$ stems from the interaction of the chromophore with both pulses. In principle, all $I_k(\tau, \phi)$ can be evaluated analytically through $(k - 1)$ -order response functions,^{23,24} but the expressions rapidly become cumbersome.

If the pump pulses are temporally well separated (that is, if the time interval between the pulses, τ , is much longer than the pulse duration τ_p), the double-pump signal assumes the form

$$I_F(\tau, \phi) = A(\tau) + (B(\tau)e^{i\phi} + B^*(\tau)e^{-i\phi})e^{-\gamma_2\tau} + (C(\tau)e^{2i\phi} + C^*(\tau)e^{-2i\phi})e^{-\gamma_3\tau}. \quad (15)$$

Here $A(\tau)$ is the contribution which results from the evolution of the chromophore in the electronic population during the pulse delay τ . $B(\tau)$ is the (single) coherence contribution, which involves the electronic states 1, 2 and 3. The term $C(\tau)$ is the double coherence contribution, which involves the electronic states 1, 3.

The explicit expressions for $A(\tau)$, $B(\tau)$ and $C(\tau)$ can be found in the Appendix. The contributions $B(\tau)$ and $C(\tau)$ vanish if the pump pulses are not phase-locked or if the time delay between the pulses exceeds the optical dephasing time, $\tau \gg \gamma_2^{-1}, \gamma_3^{-1}$. In this case, $I_F(\tau, \phi)$ yields the strong-pulse pump-probe signal described in ref. 25 and 26. The SM experiments of ref. 11, in which the pulses are not phase-locked, are exclusively described by the $A(\tau)$ -contribution.

If the optical coupling between the states $|2\rangle$ and $|3\rangle$ can be neglected ($\mu_{23} = 0$, $\eta_{23} = 0$), the model of the chromophore reduces to an electronic two-state system. In this case, eqn (15) simplifies to

$$I_F(\tau, \phi) = A(\tau) + (B(\tau)e^{i\phi} + B^*(\tau)e^{-i\phi})e^{-\gamma_2\tau} \quad (16)$$

where $A(\tau)$ and $B(\tau)$ are the population and coherence contributions.

Eqn (16) reveals that the phase dependence of the SM signal of an electronic two-state system excited by temporally well separated pump pulses of arbitrary strength reads

$$I_F(\tau, \phi) = \chi + \theta_1 \cos(\phi + \tilde{\phi}_1). \quad (17)$$

Here χ , θ_1 , $\tilde{\phi}_1$ are τ -dependent parameters. In the weak-field regime, eqn (17) applies also for overlapping pulses.¹⁰

Eqn (15) shows that the signal of an electronic three-state system excited by temporally well separated pulses of arbitrary strength exhibits the phase dependence

$$I_F(\tau, \phi) = \chi + \theta_1 \cos(\phi + \tilde{\phi}_1) + \theta_{12} \cos(2\phi + \tilde{\phi}_2), \quad (18)$$

where θ_{12} , $\tilde{\phi}_2$ are τ -dependent parameters. The $\cos(2\phi + \tilde{\phi}_2)$ contribution stems from the double electronic coherence involving the electronic states 1 and 3. This term can be considered as a witness of the optical coupling to higher-lying electronic states.

IV. Choice of parameters and computational details

The mean values of the model parameters (8) are chosen as follows. The vibrational frequency is set to $\bar{\Omega} = 0.13$ eV which corresponds to a vibrational period $\tau_\Omega = 2\pi/\bar{\Omega} = 32$ fs (these values are typical for the signals of ref. 2–4). The dimensionless shifts of the potential energy functions are chosen as $\bar{A}_2 = 2$ and $\bar{A}_3 = -1$ (see Fig. 1). To illustrate the impact of higher-lying electronic states, we assume that the energy gap between the states 1 and 2 matches the gap between the states 2 and 3, that is $\bar{\epsilon}_3 = 2\bar{\epsilon}_2$. Since it is common practice to excite SM chromophores in resonance with the 0–0 transition, we set

$$\omega_1 = \omega_2 = \bar{\epsilon}_2/\hbar. \quad (19)$$

Hence the numerical values of $\bar{\epsilon}_k$ and ω_a are irrelevant for the evaluation of $I_F(\tau, \phi)$. The pulses are assumed to have Gaussian envelopes

$$f(t) = \exp\{-(t/\tau_p)^2\} \quad (20)$$

and short durations ($\tau_p = 10$ fs, $\tau_p \ll \tau_\Omega$).

We evaluate $I_F(\tau, \phi)$ by the exact numerical solution of the master eqn (11). For each particular realization (10) of the model parameters (8), we represent the master equation in matrix form by an expansion of the density matrix in the eigenfunctions of the vibrational ground-state Hamiltonian and solve it numerically by a fourth-order Runge-Kutta integrator with a time step of 0.25 fs. The chromophore is assumed to be initially prepared in the vibrational ground state of the electronic ground state.

V. Electronic two-state chromophores

If the optical coupling between state 2 and state 3 can be neglected ($\eta_{23} = 0$), the chromophore can be considered as an electronic two-state system. In Section VA, we analyze signals of such chromophores under the assumption that all model parameters (8) assume their mean values and set $\hat{\epsilon}\hat{\mu}_{12} = 1$, which renders $\eta_{12} = \eta_{12}^{(0)}$. This establishes a reference picture for the study of modulations of these parameters in Section VB.

A. No stochastic modulation of parameters

Fig. 2 shows typical examples of the evolution of the population of the excited electronic state $\text{Tr}\{\rho_{22}(t)\}$ in the weak-coupling regime ($\eta_{12} = 0.02$ eV) and in the strong-coupling regime ($\eta_{12} = 0.4$ eV). In this example, the pump pulse #1 comes at $t = 0$, while pump pulse #2 arrives at $t = 80$ fs.

In the weak-coupling regime (black line), where $\text{Tr}\{\rho_{22}(t)\} \sim \eta_{12}^2$, pump #1 creates a certain excited-state population around $t = 0$. Then $\text{Tr}\{\rho_{22}(t)\}$ remains constant until pulse #2 transfers more population from the ground electronic state $|1\rangle$ to the excited state $|2\rangle$. It is this population which yields the weak-coupling SM signal $I_F(\tau, \phi) = I_2(\tau, \phi)$.

In the strong-coupling regime (blue line), the situation is different. The linear scaling of $\text{Tr}\{\rho_{22}(t)\}$ with η_{12}^2 ceases to

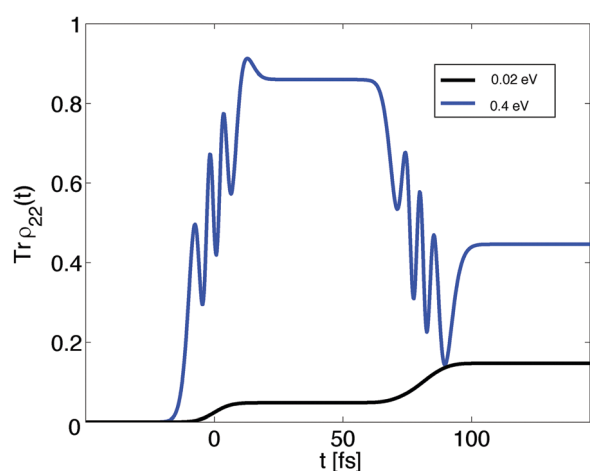


Fig. 2 Time evolution of the excited-state population $\text{Tr}\{\rho_{22}(t)\}$ for $\tau = 80$ fs, $\phi = 0$, $\bar{\gamma}_2 = 0$ and two system-field couplings η_{12} indicated in the legend.

be valid, because the field-induced population exchange is governed by Rabi oscillations.^{27,28} These oscillations are clearly seen during the interaction of the chromophore with pulse #1 and #2. For this example, the frequency of Rabi oscillations is estimated as $\bar{\Omega}_R \approx 2\eta_{12}/\hbar$, which for $\eta_{12} = 0.4$ eV yields the period $2\pi/\bar{\Omega}_R = 5.17$ fs. This is close to the period 5.25 fs of the Rabi beatings visible in the figure. Pulse #2 may not only increase but may also decrease the population, as shown in the figure. This is a direct consequence of the oscillatory ($\sim \sin^2(\bar{\Omega}_R\tau_p/2)$) dependence of the excited-state population on the coupling parameter η_{12} . In the strong-coupling regime, π -pulses ($\bar{\Omega}_R\tau_p \approx \pi$) can be used to invert the electronic population and the field strength can be employed to manipulate vibrational wave packets.^{29–31} The time resolution in the strong-coupling regime is not limited by the pulse durations, in contrast to the weak-coupling regime.³² This illustrates that the use of strong pulses offers more possibilities to manipulate and control double-pump SM responses.

The populations in Fig. 2 do not exhibit oscillations of vibrational origin. However, the wave-packet motion is imprinted into the value of $\text{Tr}\{\rho_{22}(t_\infty)\}$ for each particular interpulse delay and the SM signal exhibits signatures of wave-packet dynamics. This is illustrated by Fig. 3, which shows how the time evolution of $I_F(\tau, 0)$ changes with the coupling parameter η_{12} for a moderate electronic dephasing rate. The signals depicted by full lines are proportional to η_{12}^2 and correspond to the weak-coupling regime. For $\tau < \bar{\gamma}_2^{-1}$, they exhibit low-amplitude vibrational beatings with a period $\tau_\Omega = 32$ fs which are quenched by dephasing for $\tau > \bar{\gamma}_2^{-1}$.¹⁰ When η_{12} further increases, the linear scaling of the signal with η_{12}^2 starts to break down. The signals depicted by dashed lines correspond to the strong-coupling regime and show vibrational oscillations, both for $\tau < \bar{\gamma}_2^{-1}$ and $\tau > \bar{\gamma}_2^{-1}$.

The considerations of Section III help us to rationalize the behavior of the signals in Fig. 3. If the pulses are temporally well separated, the signal can be split into the population contribution $A(\tau)$ and the coherence contribution $B(\tau)$. In the weak-coupling regime, $A(\tau)$ is τ -independent, and the time

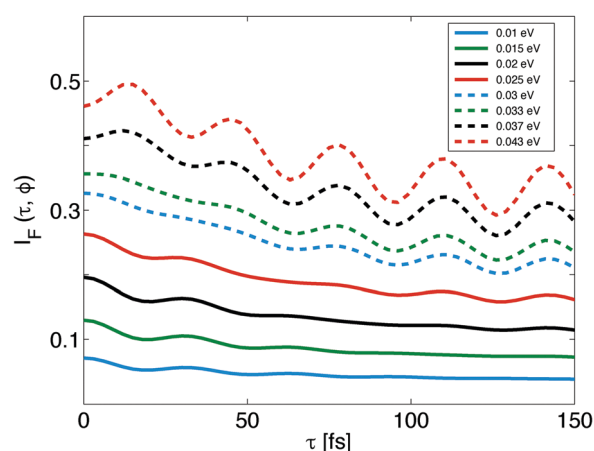


Fig. 3 SM signal $I_F(\tau, 0)$ vs. τ for different coupling parameters η_{12} indicated in the legend; the electronic dephasing time is $\bar{\gamma}_2^{-1} = 50$ fs.

evolution of the signal is determined exclusively by $B(\tau)$, which is quenched due to the electronic dephasing $\bar{\gamma}_2$.¹⁰ Hence the full-line-signals in Fig. 3 exhibit weak vibrational beatings which are quenched for $\tau > \bar{\gamma}_2^{-1}$. In the strong-coupling regime, on the other hand, both $A(\tau)$ and $B(\tau)$ are τ -dependent. For $\tau > \bar{\gamma}_2^{-1}$, $B(\tau)$ is quenched by dephasing while $A(\tau)$, which is unaffected by dephasing, dominates the signal and exhibits vibrational beatings (dashed lines in Fig. 3). The weak-coupling signals (full lines) and the strong-coupling signals (dashed lines) oscillate in anti-phase for $\tau < \bar{\gamma}_2^{-1}$. The former have their minima at $\tau = 14$ and 46 fs, and a maximum at $\tau = 30$ fs. The latter have their maxima at $\tau = 14$ and 46 fs, and a minimum at $\tau = 30$ fs. Hence the signals exhibit a flip of π in the phase of the beating upon change from the weak-coupling regime to the strong-coupling regime. It is the interplay between the population contribution $A(\tau)$ and the coherence contribution $B(\tau)$ which produces the π -flip of the phase.^{33,34}

The signal in Fig. 3 for $\eta_{12} = 0.03$ eV is at the border line between the weak-coupling regime and the strong-coupling regime. Hence $\eta_{12}^{(c)} = 0.03$ eV can be termed as the critical system-field coupling. This value of $\eta_{12}^{(c)}$ is not universal and depends on the characteristics of the material system and laser fields. It is remarkable, however, that the critical value of the system-field coupling parameter (that is, the coupling indicating a turnover from the weak-coupling regime to the strong-coupling regime) for pump-probe signals is the same for a similar model system and laser field parameters.²⁶ This is an indication of the universality of the crossover between the weak-coupling and strong-coupling regimes in femtosecond molecular spectroscopy.

Fig. 4 presents an alternative view of how the signals change with the coupling parameter. Panel (a) depicts $I_F(\tau, 0)$ as a function of τ for different η_{12} . In the weak-field regime, the signal scales linearly with the field intensity, $I_F(\tau, 0) \sim \eta_{12}^2$. When η_{12} attains the critical value $\eta_{12}^{(c)} = 0.03$ eV discussed above, the signals still increase with η_{12} , but increase slower than $\sim \eta_{12}^2$. For $\eta_{12} \geq \eta_{12}^{(c)}$, the signal reaches a maximum and starts to decrease, which manifests the onset of the oscillatory

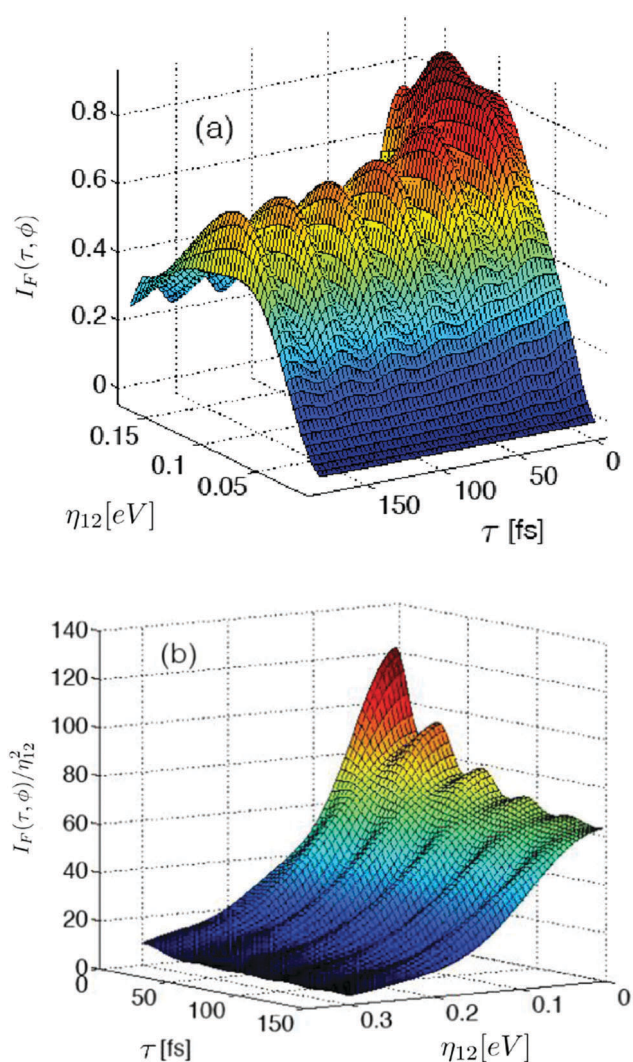


Fig. 4 The SM signal as a function of the time-delay τ and the coupling parameter η_{12} for the moderate electronic dephasing time $\bar{\gamma}_2^{-1} = 50$ fs. (a) $I_F(\tau, 0)$. (b) $I_F(\tau, 0)/\eta_{12}^2$. Note that the axes of (b) are rotated with respect to those of (a).

dependence of $I_F(\tau, 0)$ on η_{12} . Panel (b) depicts the same signal, but scaled by η_{12}^2 , $I_F(\tau, 0)/\eta_{12}^2$. This signal is η_{12} -independent in

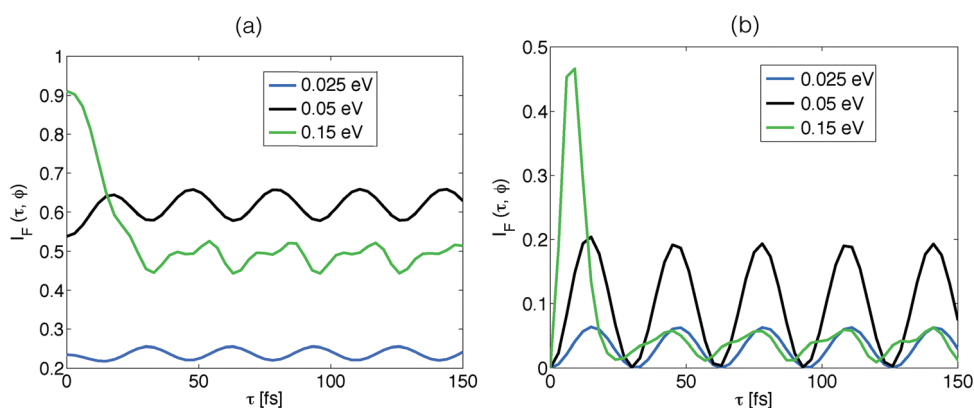


Fig. 5 SM signal $I_F(\tau, \phi)$ for $\phi = 0$ (a) and $\phi = \pi$ (b) vs. τ for several η_{12} indicated in the legend; $\bar{\gamma}_2 = 0$.

the weak-field regime (small η_{12} in panel (b)) and exhibits vibrational beatings which are damped owing to electronic dephasing.¹⁰ Once the coupling attains $\eta_{12}^{(c)} = 0.03$ eV, the vibrational beatings exhibit the π -flip discussed above. For $\eta_{12} \geq \eta_{12}^{(c)}$, the signal in panel (b) decreases with η_{12} , showing a clear deviation from the weak-coupling behavior. In the limit $\eta_{12}^2 \rightarrow \infty$, $I_F(\tau, \phi)/\eta_{12}^2 \rightarrow 0$.

Fig. 5 illustrates signals in the weak-field and strong-field regimes for different relative phases ϕ of the pump pulses. Let us consider $I_F(\tau, 0)$ (panel (a)) first. As explained in ref. 10, weak-field signals always decrease at short τ (blue line). The strong-field signals can either decrease (green line) or increase (black line). This is a direct reflection of Rabi cycling.^{27,28} Indeed, the two pump pulses at $\tau = 0$ are equivalent to a single pump pulse with double amplitude $2E_0$. If this pulse is stronger than the corresponding molecular π -pulse,³⁰ then it is less efficient in promoting the population to the excited electronic state. Hence a pair of strong pump pulses of amplitude E_0 separated by a time $\tau \neq 0$ can be more efficient in the excitation than the same pulses at $\tau = 0$.

As discussed above, $I_F(\tau, 0)$ exhibits a phase flip by π when changing from the weak-field regime to the strong-field regime. The signals depicted by blue and black lines in Fig. 5(a) clearly show this behavior. If the coupling exceeds $\eta_{12}^{(c)}$ considerably, the shape of the strong-field signal can also change (*cf.* black and green lines in Fig. 5(a)). The reason is that the number of Rabi cycles during the action of the pulse increases with η_{12} . These Rabi cyclings produce highly non-equilibrium distributions involving multiple vibrational levels in the ground and excited electronic states which modify the shapes of the vibrational beatings.^{25,32}

The $I_F(\tau, \pi)$ signals in Fig. 5(b) do not exhibit the π -flip. All these signals start from zero, because the overlapping pulses with $\phi = \pi$ cancel each other and do not excite the system. In the limit of Dirac delta-pulses, the difference between the weak-field signals and strong-field signals reduces to a scaling factor (see, *e.g.*, the discussion in ref. 35). The analysis of ref. 10 reveals that $I_F(\tau, \pi) = 0$ for $\bar{\gamma}_2 = 0$ and $\tau = \tau_0 n$ ($n = 0, 1, 2, \dots$). A slight deviation of the signals of Fig. 5(b) from this behavior is caused by the finite pulse duration.

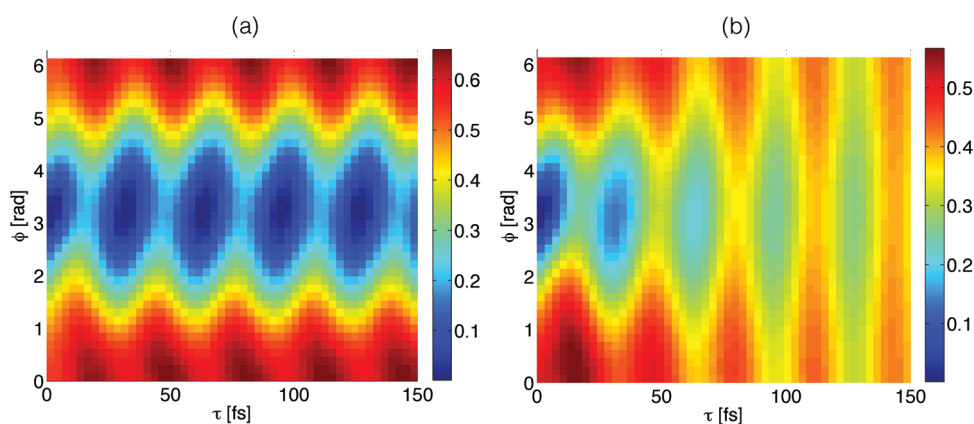


Fig. 6 2D maps $I_F(\tau, \phi)$ for $\eta_{12} = 0.05$ eV. (a) $\bar{\gamma}_2 = 0$. (b) $\bar{\gamma}_2^{-1} = 50$ fs.

Fig. 6 depicts two-dimensional (2D) plots of $I_F(\tau, \phi)$ vs. τ and ϕ , so-called fluorescence maps,^{2,5} calculated without (a) and with (b) electronic dephasing. Several general patterns in Fig. 6 can be understood from the following considerations. When the two pump pulses overlap ($\tau = 0$), the phase $\phi = \pi$ creates no excitation, because the pulses cancel each other (destructive interference). In contrast, for $\phi = 0, 2\pi$ the pulses reinforce each other (constructive interference). These results are independent of the pulse strength and electronic dephasing. Hence the 2D maps for $\tau < \tau_p$ exhibit a minimum at $\phi = \pi$ and maxima at $\phi = 0, 2\pi$, both in the weak-field regime and in the strong-field regime.

Apart from trivial intensity effects, there are fundamental qualitative differences between the weak-field and strong-field 2D maps for $\tau \geq \tau_p$. For weak pulses, the 2D maps show periodic phase-time profiles of the harmonic oscillator wavepacket which are tilted to the right and wiped out for $\tau \geq \bar{\gamma}_2^{-1}$ due to electronic dephasing.¹⁰ For strong pulses, on the other hand, the phase-time profiles exhibit a weaker tilt to the right (Fig. 6(a)). Furthermore, electronic dephasing does not quench the signal for $\tau \geq \bar{\gamma}_2^{-1}$ (Fig. 6(b)): $I_F(\tau, \phi)$ shows ϕ -independent stripes at $\tau = 62, 94$ and 126 fs, which reveal vibrational beatings with the period of $\tau_\Omega = 32$ fs. The reason is that the population (ϕ -independent) contribution $A(\tau)$ and the coherence (ϕ -dependent) contribution $B(\tau)$ are both τ -dependent and reveal vibrational beatings for strong pulses.

B. Effect of stochastic modulation of parameters

As has been discussed in Section II, each setting of the time delay (9) corresponds to a new experiment on the same chromophore, in which it experiences a different local environment and therefore has different molecular parameters. Hence the parameters (8) of the chromophore Hamiltonian and the dephasing operator change for each value of the time delay as modeled by eqn (10). Similar to the measurement protocol of ref. 2 and 3, we assume that $\Delta_\tau = 3$ fs.

Fig. 7(a) shows the representative signals $I_F(\tau, 0)$ and $I_F(\tau, \pi)$ evaluated for mean values of the parameters (8) specified in the figure caption. Fig. 7(b) through (e) show the same signals simulated with modulation of the chromophore electronic

energy (b), orientation (c), electronic dephasing (d), and displacement of the potential energy function (e). Panel (f) displays the effect of the simultaneous modulation of all these parameters.

Let us start the discussion with panel (a). $I_F(\tau, 0)$ initially increases with τ . This is a strong-field effect (recall the discussion of Fig. 5). On the other hand, $I_F(0, \pi) \equiv 0$ and $I_F(\tau, \pi)$ also initially increase with τ . $I_F(\tau, 0)$ and $I_F(\tau, \pi)$ converge for $\tau \geq \bar{\gamma}_2^{-1}$ and reveal vibrational beatings which, notably, are not quenched by dephasing. This is explained in terms of the contributions $A(\tau)$ and $B(\tau)$: the population contribution $A(\tau)$ is phase-independent and not affected by dephasing while the coherence contribution $B(\tau)$ is ϕ -dependent and decays as $\exp(-\bar{\gamma}_2\tau)$. Both $B(\tau)$ and $A(\tau)$ reveal vibrational beatings for strong pump pulses.

Now we discuss the effect of the modulation of the parameters. In the previous paper,¹⁰ we have identified the critical values of the parameters for which the SM signals in the weak-coupling limit become so noisy that the vibrational beatings cease to be undetectable. The modulation amplitudes δ_A of the parameters selected for Fig. 7(b)–(f) are higher than the critical amplitudes given in Table 1 of ref. 10. For such high values of δ_A the weak-field signals are buried in noise and do not exhibit any regular features, which renders the extraction of useful information highly problematic. On the other hand, the strong-field signals in Fig. 7(b)–(f), although noisy, do reveal the vibrational beatings. Below we give a rationale for this finding.

Consider first the modulations of the electronic excitation energy. The robustness of the strong-field SM signals to the modulations of ε_2 (Fig. 7(b)) can be explained in terms of the contributions $A(\tau)$ and $B(\tau)$: the coherence contribution $B(\tau)$ depends strongly on the electronic energy fluctuations. This is the only τ -dependent contribution to $I_F(\tau, \phi)$ in the weak-coupling regime,¹⁰ hence the high sensitivity of the weak-field signals. In the strong-coupling regime, on the other hand, the population term $A(\tau)$, which is much less sensitive to the modulations of ε_2 , is also τ -dependent and contributes to $I_F(\tau, \phi)$ on an equal footing with $B(\tau)$.

The modulations of $\hat{\varepsilon}_{\mu_{12}}$ reflect restricted chromophore reorientation (wobbling) in the polymer matrix, which is normally described *via* the diffusion-in-the-cone model.³⁶ In the

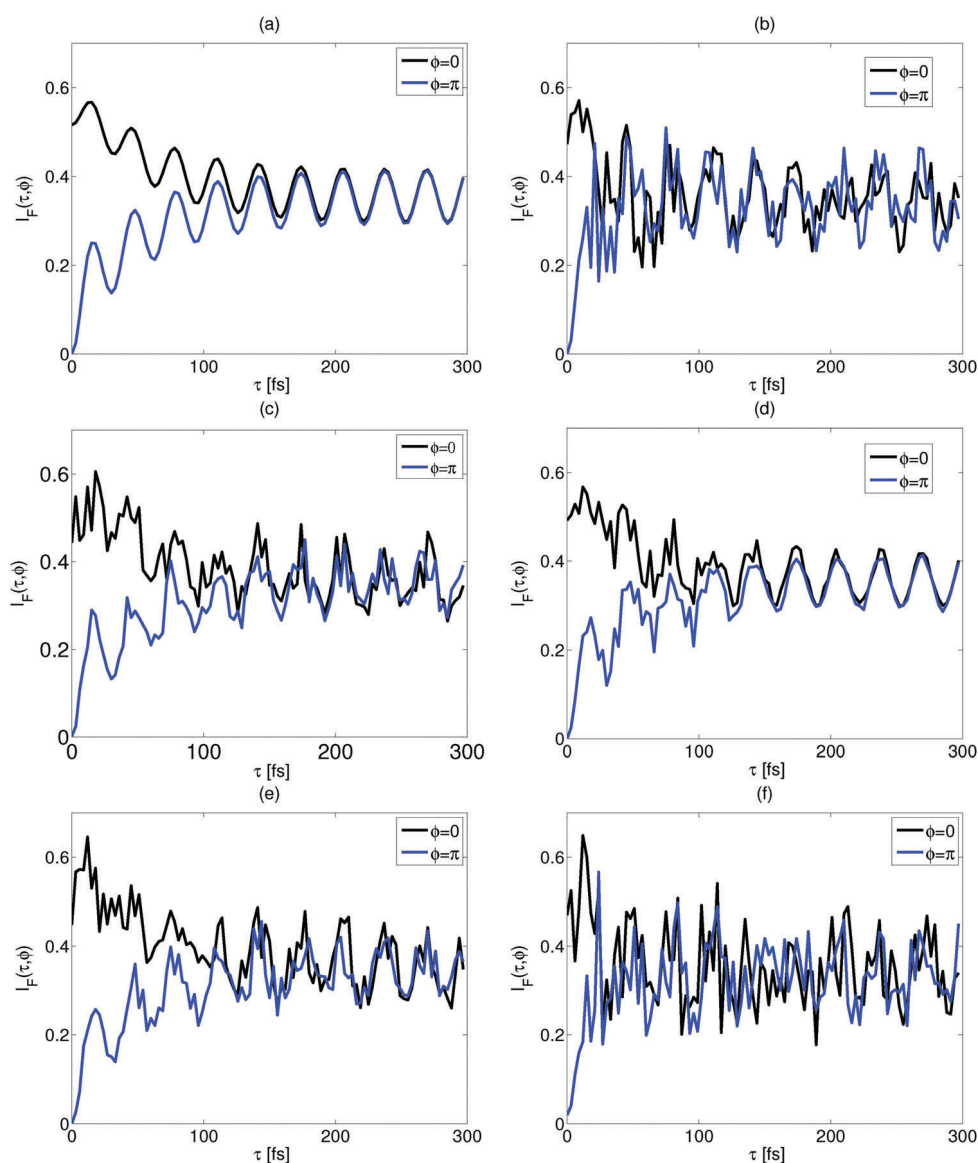


Fig. 7 Panel (a) depicts the SM signals $I_F(\tau, 0)$ (black line) and $I_F(\tau, \pi)$ (blue line) evaluated for the following mean values of the parameters: $\eta_{12}^{(0)} = 0.05$ eV, $\bar{\Omega} = 0.13$ eV, $\bar{\Delta}_2 = 2$, $\hat{\mathbf{e}}\hat{\boldsymbol{\mu}}_{12} = 1$, and $\bar{\gamma}^{-1} = 50$ fs. Panels (b) through (f) show the effect of modulation of the electronic energy, $\delta_{s_2} = 0.08$ eV (b); molecular orientation, $\hat{\mathbf{e}}\hat{\boldsymbol{\mu}}_{12} = \cos(\pi/4 - \varphi)/\cos(\pi/4)$, $\delta_\varphi = 0.6$ (c); electronic dephasing, $\delta_{\gamma^{-1}} = 70$ fs (d) displacement of the potential energy function, $\delta_{\Delta_2} = 0.32$, (e). Panel (f) displays the effect of the simultaneous modulations of all the above parameters. The signals are evaluated with a discretization step of 3 fs in τ .

weak-coupling regime, $I_F(\tau, \phi) \sim \eta_{12}^2$ and the δ_φ -variations produce quadratic modulations of the signal amplitude. In the strong-coupling regime, on the other hand, the dependence of $I_F(\tau, \phi)$ on η_{12}^2 is much weaker (recall Fig. 4 and its discussion). That explains the higher robustness of the strong-field signals against δ_φ -modulations (Fig. 7(c)).

The effect of the modulation of the electronic dephasing (Fig. 7(d)) is visible only on the timescale characteristic for the electronic dephasing. For $\tau \geq \bar{\gamma}_2^{-1}$, the effect disappears. Again, this phenomenon is a direct consequence of the decomposition of the signal into the coherence contribution $B(\tau) \sim \exp(-\gamma_2\tau)$ and the dephasing-independent population contribution $A(\tau)$. While the signal is solely determined by $B(\tau)$ in the weak-coupling regime, both $B(\tau)$ and $A(\tau)$ contribute in the strong-coupling regime.

The effect of the modulation of the displacement of the potential energy function, Δ_2 , is illustrated in Fig. 7(e). In the weak-coupling regime, $I_F(\tau, \phi)$ has a Gaussian dependence on Δ_2 (see eqn (20) and (26) of ref. 10). This indicates that Δ_2 controls the Franck–Condon factors of the relevant optical transitions. Hence, the high sensitivity of $I_F(\tau, \phi)$. In the strong-coupling regime, the system-field interaction is governed by Rabi cyclings and significantly depends on the pulse amplitude and duration. As a result, transitions with weak Franck–Condon factors can be significantly enhanced.³⁷ This diminishes the influence of modulations of Δ_2 on the signal in the strong-coupling limit.

Fig. 7(f) shows the effect of the simultaneous modulation of all these parameters. Despite the signals the $I_F(\tau, 0)$ (black line) and $I_F(\tau, \pi)$ (blue line) are quite noisy, they still reveal signatures

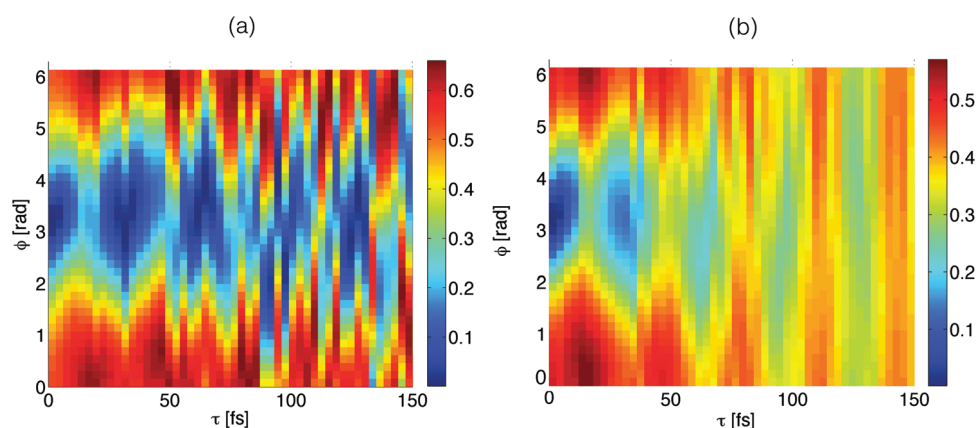


Fig. 8 2D maps $I_F(\tau, \phi)$ for $\eta_{12}^{(0)} = 0.05$ eV. The electronic energy gap is sampled according to eqn (10) with $\delta_{\varepsilon_2} = 0.07$ eV. (a) $\bar{\gamma}_2 = 0$. (b) $\bar{\gamma}_2^{-1} = 50$ fs.

of vibrational beatings, especially at longer time scales when the dephasing-sensitive contributions have disappeared.

We did not include the effect of the modulation of the vibrational frequency in Fig. 7. It turns out that the sensitivity of $I_F(\tau, \phi)$ to the modulations of Ω is roughly independent of the system-field coupling. The reason is that the time evolution of the electronic population $A(\tau)$ and the electronic coherence $B(\tau)$ is determined by vibrational motion which, in turn is governed by the vibrational frequency. When the amplitude of the modulation of the vibrational frequency, δ_{Ω} , is much smaller than the vibrational period τ_{Ω} , a few vibrational beatings can be detected in $I_F(\tau, \phi)$, notably at short τ . Otherwise, coherent vibrational motion ceases to be observable. These arguments are general and therefore applicable to both weak- and strong-coupling regimes. Yet, keeping in mind the exclusive role of the vibrational frequency, we can conclude that SM signals in the strong-coupling regime are more robust to modulations of the system parameters than SM signals in the weak-coupling regime.

Fig. 8 exemplifies the effect of the environment-induced modulation of chromophore parameters on 2D maps $I_F(\tau, \phi)$. This figure should be compared with Fig. 6, which displays the same signals without parameter modulations. For short τ , the maps in Fig. 8 can be considered as blurred versions of those in Fig. 6. For longer τ , the differences between Fig. 6 and 8 are more substantial and can be rationalized as follows. The population contribution $A(\tau)$ is ϕ -independent and variations of ε_2 produce stripes for $\tau > \bar{\gamma}_2^{-1}$, when the coherence contribution $B(\tau)$ disappears. The stripes in Fig. 7(b) reveal maxima around $\tau = 62, 94$ and 126 fs, reflecting vibrational wave packet motion. These vibrational features are totally absent in the weak-coupling 2D maps.¹⁰ Hence the 2D maps allow a clear distinction between the weak-coupling and strong-coupling regimes, even if the modulation of the system parameters is relatively strong.

VI. Electronic three-state chromophores

As has been explained in ref. 10, the weak-field SM signal $I_F(\tau, \phi)$ given by $I_2(\tau, \phi)$ in the expansion (14) is not affected by radiative

coupling to higher-lying electronic states. If the system-field coupling increases, the terms $I_k(\tau, \phi)$ with $k \geq 2$ in the expansion (14) become non-negligible and higher-lying electronic states may contribute to the signal, giving rise to excited-state absorption and/or stimulated emission. These effects are described by eqn (15), which partitions the signal of an electronic three-state chromophore into three contributions: the population $A(\tau)$, the single-coherence $B(\tau)$, and the double-coherence $C(\tau)$ (the latter is absent in two-state chromophores). To simplify the presentation in the present section, we assume the same strength of optical coupling between the electronic states 1,2 and 2,3: $\eta_{12} = \eta_{23}$. For brevity, we do not consider the modulation of the molecular parameters.

As a function of τ for fixed ϕ , the signal $I_F(\tau, \phi)$ of an electronic three-state chromophore does not show qualitatively different behavior in comparison with the signal of the corresponding two-state chromophore. A difference can arise when the vibrational frequencies in the three electronic states are different, but this situation is not considered here for brevity (these effects have been studied in ref. 25 and 26 for strong-pump strong-probe signals). On the other hand, the dependence of $I_F(\tau, \phi)$ on ϕ for fixed τ may look qualitatively different for two- and three-state chromophores. This effect has been discussed in Section III and is illustrated in Fig. 9. The phase dependence deviates from the $\cos(\phi + \tilde{\phi}_1)$ form of eqn (17) due to the presence of the double-coherence term $\cos(2\phi + \tilde{\phi}_2)$ in eqn (18). The deviation of the signal from eqn (17) can be considered as a witness of the radiative coupling with higher-lying electronic states.

2D maps $I_F(\tau, \phi)$ for a three-state chromophore without (a) and with (b) electronic dephasing are depicted in Fig. 10. These maps should be compared with those for the two-state chromophore presented in Fig. 6. Let us consider first the dephasing-free situation. The maps in Fig. 6(a) and 10(a) reflect the periodicity of the vibrational wave-packet motion in the electronic states involved. However, the third electronic state causes pronounced qualitative differences between the two maps. The signals in Fig. 10(a) do not exhibit phase-time profiles of a harmonic oscillator wave packet which are clearly seen in Fig. 6(a) and are typical for the electronic two-state chromophore. The signals

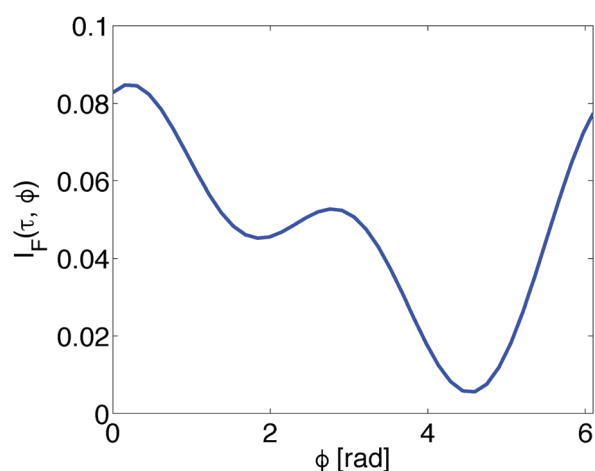


Fig. 9 Dependence of the SM signal $I_F(\tau, \phi)$ of the electronic three-state chromophore on the phase ϕ for a fixed time delay $\tau = 150$ fs, $\eta_{12} = 0.05$ eV, and $\bar{\gamma}_2 = \bar{\gamma}_3 = 0$.

in Fig. 10(a) rather show progressions of the three-maxima-two-minima patterns of changing shape and increasing asymmetry relative to the line $\phi = \pi$. This reflects nontrivial wavepacket interferometry in all three electronic states driven by two strong pump pulses. This asymmetry is a signature of the contributions from higher-lying excited electronic states. Interestingly, the signal in panel (a) of Fig. 10 displays a tilt of the τ, ϕ pattern to the right. This tilt is reinforced by the double-coherence contribution $C(\tau)$ which has a $\sim \exp(\pm i2\phi)$ phase dependence. The effect of electronic dephasing on the 2D maps of two-state system (Fig. 6(b)) and three-state system (Fig. 10(b)) is qualitatively similar. The signal in Fig. 10(b) shows equidistant stripes around $\tau = 62, 94$ and 126 fs which reveal vibrational wave-packet motion. They arise from the population contribution $A(\tau)$ and become visible when the single-coherence term $B(\tau)$ and the double-coherence term $C(\tau)$ are quenched by electronic dephasing. One thus can conclude that radiatively coupled higher-lying excited electronic states can substantially affect the phase-dependence of SM signals. Electronic dephasing attenuates this dependence, rendering the SM signals of two- and three-state chromophores similar.

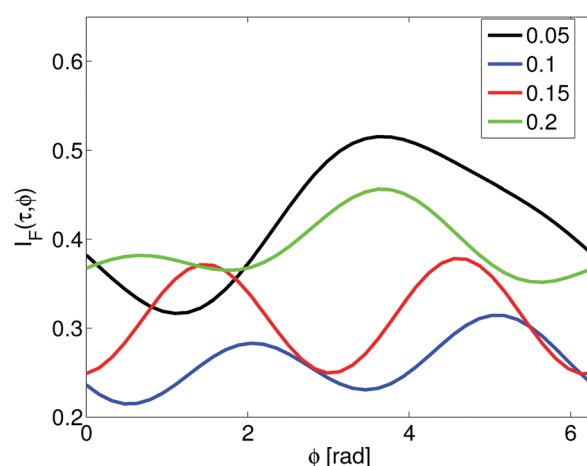


Fig. 11 SM signal $I_F(\tau, \phi)$ at a fixed $\tau = 50$ fs for different system-field couplings η_{12} indicated in the legend. $\bar{\gamma}_2^{-1} = \bar{\gamma}_3^{-1} = 50$ fs.

In Section VA, we have demonstrated that the system-field coupling can be used to manipulate and control the SM signals of two-state chromophores. This is possible for three-state chromophores too, even in the case of significant electronic dephasing. Fig. 11 shows the SM signals $I_F(\tau, \phi)$ for a fixed $\tau = 50$ fs and different system-field couplings η_{12} indicated in the legend. In contrast to the weak-coupling regime, the variation of η_{12} in the strong-coupling regime does not significantly change the overall signal intensity, but substantially alters the shape of the signal. As η_{12} increases, $I_F(\tau, \phi)$ in Fig. 11 evolves from a single-maximum single-minimum structure (black line) to double-maxima double-minima structures of different shapes (blue, red, and green lines), which are similar to that in Fig. 9. Hence the system-field coupling can be used to control and manipulate the SM signals of three-state chromophores. This may be important for applications, since the coupling of multi-state chromophores with femtosecond laser pulses can be adjusted to minimize the net population transfer to higher-lying excited electronic states in order to prevent unwanted photodissociation or photoisomerization.

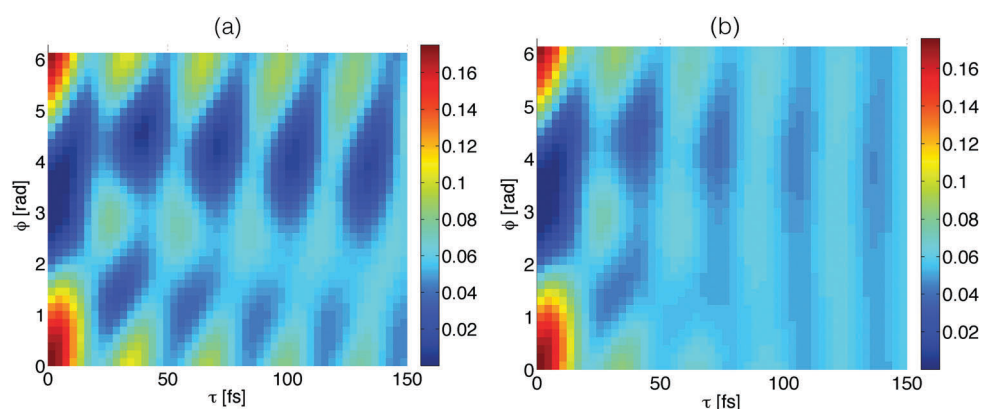


Fig. 10 2D maps of the electronic three-state chromophore for $\eta_{12} = 0.05$ eV. (a): $\bar{\gamma}_2 = \bar{\gamma}_3 = 0$. (b): $\bar{\gamma}_2^{-1} = \bar{\gamma}_3^{-1} = 50$ fs.

VII. Conclusions

In the present work, we have performed a systematic study of femtosecond double-pump signals of individual two-electronic-state and three-electronic-state chromophores in the strong-coupling regime. The SM signal consists of population and coherence contributions. In the weak-coupling regime, only the coherence contribution depends on the time delay τ between the pump pulses, while the population contribution is static. In the strong-coupling regime, on the other hand, both of these contributions are τ -dependent and contain information on the vibrational dynamics of the chromophore.

For a specific chromophore, there exists a critical value of the system-field coupling parameter which represents the turnover from the weak-coupling regime to the strong-coupling regime. The double-pump signals in the two regimes exhibit qualitatively different behaviors and patterns. The signatures of the weak-coupling regime are analyzed in the accompanying paper.¹⁰ The signatures of the strong-coupling regime are as follows. The signals exhibit vibrational beatings that are not quenched by electronic dephasing. These beatings reflect vibrational wave-packet dynamics in the electronic populations of the density matrix of the chromophore. Distinct from weak-field signals, strong-field signals for the relative phases 0 and π of the pump pulses are not mirror images of each other. When the time delay between the pump pulses exceeds the electronic dephasing time, the signals with relative phases 0 and π coincide and show vibrational beatings. The 2D maps of strong-field signals do not exhibit a substantial tilt of their phase-time profiles and are not quenched by electronic dephasing. The SM signals in the strong-coupling regime are more robust with respect to modulations of the system parameters than the SM signals in the weak-coupling regime.

Higher-lying excited electronic states do not contribute to femtosecond double-pump SM signals in the weak-coupling regime. In the strong-coupling regime however, their contributions may become significant. Our simulations of three-electronic-state chromophores reveal that there exist clear signatures of these contributions in the phase dependence of SM signals.

Our analysis suggests that the adjustment of the system-field coupling (by changing the laser pulse intensity) can be considered as an efficient tool for the judicious manipulation of femtosecond double-pump SM signals and for the enhancement of the information content of SM spectroscopy.

Conflicts of interest

There are no conflicts to declare.

Appendix A: derivation of eqn (15) and (16)

A rigorous derivation of eqn (15) and (16) can be given in the framework of the strong-pulse doorway-window method developed in ref. 25 and 38. Here we give a more intuitive derivation.

Let us consider an electronic two-state system first. The interaction of the system with external pulses is governed by the transition

dipole moment operator of eqn (3). Obviously, a single interaction of the system with an external pulse transforms the electronic populations $\rho_{11}(t)$ and $\rho_{22}(t)$ into electronic coherences $\rho_{12}(t)$ and $\rho_{21}(t)$ and the other way around: the electronic coherences $\rho_{12}(t)$ and $\rho_{21}(t)$ are converted into the electronic populations $\rho_{11}(t)$ and $\rho_{22}(t)$.

Before the pump pulses arrive, the system is in the electronic ground-state population. Since the SM signal $I_F(\tau, \phi)$ is proportional to the electronic population in the excited state, it is generated by an even number of interactions with the two pump pulses. There are two options: an even number of interactions with pulse #1 and an even number of interactions with pulse #2 (the contribution $A(\tau)$) and an odd number of interactions with pulse #1 and an odd number of interactions with pulse #2 (the contribution $B(\tau)$). Now assume that the two pulses are temporally well separated, so that pulse #1 arrives first and pulse #2 arrives later, with a delay τ exceeding the pulse duration. For the contribution $A(\tau)$, the system after the interaction with pulse #1 will be in the electronic population. For the contribution $B(\tau)$, the system will be in the electronic coherence. In the rotating wave approximation, each up-transition is associated with a phase factor $\exp(\pm i\phi)$ in the dipole moment operator of eqn (3), while each down-transition is associated with $\exp(\mp i\phi)$. Hence the coherence contribution $B(\tau)$ is proportional to a phase factor $\exp(\pm i\phi)$, while the population contribution $A(\tau)$ is ϕ -independent. The population contribution is not affected by electronic dephasing, but the coherence contribution decays exponentially with the electronic dephasing rate γ_2 . We thereby obtain eqn (16).

The $A(\tau)$ and $B(\tau)$ are independent of electronic dephasing and can therefore be evaluated *via* the Schrödinger equation

$$\frac{\partial |\psi(t)\rangle}{\partial t} = -\frac{i}{\hbar}(H + H_F(t))|\psi(t)\rangle, \quad (\text{A1})$$

where H and $H(t)$ are given by eqn (1) and (3). This may be of advantage for applications, since a numerical solution of the Schrödinger eqn (A1) is much cheaper computationally than the solution of the master eqn (11). The SM signal is expressed in terms of the wave function as follows:

$$I_F(\tau, \phi) = \text{Tr}\{|\langle \psi(t \rightarrow \infty) | 2 \rangle|^2\} \quad (\text{A2})$$

(trace implies summation over all vibrational states). The $A(\tau)$ and $B(\tau)$ can be retrieved from eqn (A2), which is evaluated through the solution of the Schrödinger eqn (A1) for $\phi = 0, \pi/2$ and π :

$$I_F(\tau, 0) = A(\tau) + B(\tau) + B^*(\tau),$$

$$I_F(\tau, \pi) = A(\tau) - (B(\tau) + B^*(\tau)),$$

$$I_F(\tau, \pi/2) = A(\tau) + i(B(\tau) - B^*(\tau)).$$

Hence,

$$A(\tau) = \frac{I_F(\tau, 0) + I_F(\tau, \pi)}{2},$$

$$\text{Re } B(\tau) = \frac{I_F(\tau, 0) - I_F(\tau, \pi)}{4},$$

$$\text{Im } B(\tau) = \frac{I_F(\tau, 0) + I_F(\tau, \pi)}{4} - \frac{I_F(\tau, \pi/2)}{2}.$$

The derivation of eqn (15) for an electronic three-state system is very similar. The difference is as follows: By two interactions with pulse #1, the system can be transformed from the electronic ground state $|1\rangle$ to the electronic coherence between the states $|1\rangle$ & $|3\rangle$. Hence the phase factor $\exp(2i\phi)$ and the double-coherence contribution $C(\tau)$. Solving the Schrödinger eqn (A1) for $\phi = 0, \pi/4, \pi/2, -\pi/2$, and π , we obtain after elementary algebra:

$$A(\tau) = \frac{I_F(\tau, 0) + I_F(\tau, \pi) + I_F(\tau, \pi/2) + I_F(\tau, -\pi/2)}{4},$$

$$\text{Re } B(\tau) = \frac{I_F(\tau, 0) - I_F(\tau, \pi)}{4},$$

$$\text{Im } B(\tau) = \frac{I_F(\tau, -\pi/2) - I_F(\tau, \pi/2)}{4},$$

$$\text{Re } C(t) = \frac{I_F(t, 0) + I_F(t, \pi) - I_F(t, \pi/2) - I_F(t, -\pi/2)}{8},$$

$$\text{Im } C(\tau) = \frac{1}{2}(A(\tau) - I_F(\tau, \pi/4)) + \frac{1}{\sqrt{2}}(\text{Re } B(\tau) - \text{Im } B(\tau)).$$

The validity of eqn (15) and (16) is based on the following two conditions. The pump pulses must be (i) temporally well separated ($\tau \gg \tau_p$, pulse overlap effects are neglected) and (ii) relatively short ($\tau_p < \gamma_2^{-1}, \gamma_3^{-1}$), so that the optical dephasing during the pulses can be neglected. If both conditions are satisfied, the SM signals calculated *via* eqn (15) and (16) match perfectly those obtained *via* the numerically exact solution of the master eqn (11). If (ii) is slightly violated ($\tau_p \sim \gamma_2^{-1}, \gamma_3^{-1}$) the SM signals calculated by the two methods differ quantitatively, but not qualitatively.

Acknowledgements

This work has been supported by the Deutsche Forschungsgemeinschaft (DFG) through a research grant and the DFG-Cluster of Excellence "Munich-Centre for Advanced Photonics" (www.munich-photonics.de). E. P.-G. acknowledges support by the International Max-Planck Research School of Advanced Photon Science (www.mpg.de/APS).

References

- 1 A. H. Zewail, *J. Phys. Chem. A*, 2000, **104**, 5660–5694.
- 2 D. Brinks, F. D. Stefani, F. Kulzer, R. Hildner, T. H. Haminiou, Y. Avlasevich and N. F. van Hulst, *Nature*, 2010, **465**, 905.
- 3 R. Hildner, D. Brinks and N. F. van Hulst, *Nat. Phys.*, 2011, **7**, 172.
- 4 R. Hildner, D. Brinks, F. D. Stefani and N. F. van Hulst, *Phys. Chem. Chem. Phys.*, 2011, **13**, 1888–1894.
- 5 D. Brinks, R. Hildner, F. D. Stefani and N. F. van Hulst, *Faraday Discuss.*, 2011, **153**, 51.
- 6 D. Brinks, R. Hildner, E. M. H. P. van Dijk, F. D. Stefani, J. B. Nieder, J. Hernando and N. F. van Hulst, *Chem. Soc. Rev.*, 2014, **43**, 2476–2491.
- 7 L. Piatkowski, N. Accanto and N. F. van Hulst, *ACS Photonics*, 2016, **3**, 140.
- 8 M. Orrit and J. Bernard, *Phys. Rev. Lett.*, 1990, **65**, 2716.
- 9 N. F. Scherer, R. J. Carlson, A. Matro, M. Du, A. J. Ruggiero, V. Romero-Rochin, J. A. Cina, G. R. Fleming and S. A. Rice, *J. Chem. Phys.*, 1991, **95**, 1487.
- 10 E. Palacino-González, M. F. Gelin and W. Domcke, *Phys. Chem. Chem. Phys.*, 2017, DOI: 10.1039/c7cp04809b.
- 11 E. M. H. P. van Dijk, J. Hernando, M. F. Garcia-Parajo and N. F. van Hulst, *J. Chem. Phys.*, 2005, **123**, 064703.
- 12 P. Malý, J. M. Gruber, R. J. Cogdell, T. Mančal and R. van Grondelle, *Proc. Natl. Acad. Sci. U. S. A.*, 2016, **113**, 2934.
- 13 S. Mukamel and M. Richter, *Phys. Rev. A: At., Mol., Opt. Phys.*, 2011, **83**, 013815.
- 14 H. Dong and G. R. Fleming, *J. Phys. Chem. B*, 2013, **117**, 11318.
- 15 P. Malý, J. M. Gruber, R. van Grondelle and T. Mančal, *Sci. Rep.*, 2016, **6**, 26230.
- 16 Higher-excited states in molecular aggregates involve several S_1 -excited chromophores and therefore are much more robust than the S_n states of individual chromophores. Recent SM experiments on LH2 performed at the saturation limit of the pump and probe pulses [12] seem to corroborate this observation. The theory of the present work can straightforwardly be extended towards the description of these systems.
- 17 W. Min, C. W. Freudiger, S. Lu and X. S. Xie, *Annu. Rev. Phys. Chem.*, 2011, **62**, 507.
- 18 M. C. Fischer, J. W. Wilson, F. E. Robles and W. S. Warren, *Rev. Sci. Instrum.*, 2016, **87**, 031101.
- 19 J. Jahng, J. Brocious, D. A. Fishman, S. Yampolsky, D. Nowak, F. Huang, V. A. Apkarian, H. K. Wickramasinghe and E. O. Potma, *Appl. Phys. Lett.*, 2015, **106**, 083113.
- 20 Generalization towards chromophores with several Franck-Condon-active modes is straightforward.
- 21 Y. Avlasevich, S. Müller, P. Erk and K. Müllen, *Chem. – Eur. J.*, 2007, **13**, 6555.
- 22 M. F. Gelin, Y. Tanimura and W. Domcke, *J. Chem. Phys.*, 2013, **139**, 214302.
- 23 Y. Tanimura and S. Mukamel, *Phys. Rev. E: Stat. Phys., Plasmas, Fluids, Relat. Interdiscip. Top.*, 1993, **47**, 118.
- 24 Y. Tanimura and K. Okumura, *J. Chem. Phys.*, 1997, **106**, 2078.
- 25 M. F. Gelin, D. Egorova and W. Domcke, *Phys. Chem. Chem. Phys.*, 2013, **15**, 8119.
- 26 M. F. Gelin, B. J. Rao, M. Nest and W. Domcke, *J. Chem. Phys.*, 2013, **139**, 224107.
- 27 L. C. Allen and J. H. Eberly, *Optical Resonance and Two-level Atoms*, Dover, 1988.
- 28 N. V. Vitanov, T. Halfmann, B. W. Shore and K. Bergmann, *Annu. Rev. Phys. Chem.*, 2001, **52**, 763.
- 29 J. Cao, C. J. Bardeen and K. R. Wilson, *J. Chem. Phys.*, 2000, **113**, 1898.
- 30 L. E. E. de Araujo and I. A. Walmsley, *J. Phys. Chem. A*, 1999, **103**, 10409.
- 31 J. Vala and R. Kosloff, *Opt. Express*, 2001, **8**, 238.

- 32 M. F. Gelin, D. Egorova and W. Domcke, *J. Phys. Chem. Lett.*, 2011, **2**, 114.
- 33 Frequency-dispersed weak-field pump-probe signals in the Stokes and anti-Stokes regions also exhibit phase flips, though caused by different physical reasons.
- 34 J. A. Cina, P. A. Kovac, C. C. Jumper, J. C. Dean and G. D. Scholes, *J. Chem. Phys.*, 2016, **144**, 175102.
- 35 S. Hahn and G. Stock, *Chem. Phys. Lett.*, 1998, **296**, 137.
- 36 G. Lipari and A. Szabo, *J. Am. Chem. Soc.*, 1982, **104**, 4546.
- 37 M. F. Gelin, A. K. Belyaev and W. Domcke, *Phys. Rev. A: At., Mol., Opt. Phys.*, 2013, **87**, 063416.
- 38 M. F. Gelin, D. Egorova and W. Domcke, *J. Phys. Chem. B*, 2011, **115**, 5648.